**The Thesis Committee for Ruba Afifi**
**Certifies that this is the approved version of the following Thesis:**

# $CO_2$ STORAGE RESOURCE ASSESSMENT IN SOUTHEAST OF JEFFERSON COUNTY, OFFSHORE TEXAS, USA

**APPROVED BY**
**SUPERVISING COMMITTEE:**

Timothy A. Meckel, Supervisor

Carlos A. Uroza, Co-Supervisor

Alex P. Bump

# $CO_2$ STORAGE RESOURCE ASSESSMENT IN SOUTHEAST OF JEFFERSON COUNTY, OFFSHORE TEXAS, USA


**by**

**Ruba Mahmood Afifi**


**Thesis**

Presented to the Faculty of the Graduate School of

The University of Texas at Austin

in Partial Fulfillment

of the Requirements

for the Degree of

**Master of Science in Geological Sciences**

**The University of Texas at Austin**

**August 2026**

## Dedication

I dedicate this work to my late father, Mahmood Saeed Afifi, as well as to the people of Gaza, through whom I've understood the true meaning of resilience while writing this thesis.

## Acknowledgements

Firstly, thanks to my co-supervisors at the Bureau of Economic Geology (BEG) Gulf Coast Carbon Center (GCCC), Tip Meckel and Carlos Uroza, for their guidance throughout this research. I am grateful to all GCCC staff who have contributed to my research with their insightful feedback and assistance. Special thanks to Dallas Dunlap, who provided his velocity model for seismic depth conversion of seismic elements in this study. Finally, thanks to my sponsors and mentors at Saudi Aramco for believing in me and enabling me to pursue higher education and professional development.

## Statement on the Use of AI

This thesis was entirely formulated, written and edited by humans. However, generative AI (e.g., Microsoft Copilot) was utilized for the following:

- Python code editing and troubleshooting
- Literature summarization and synthesis (not for writing)
- Petrel troubleshooting
- Grammatical and spelling corrections at the final editing stage (using Grammarly)

# Abstract

## $CO_2$ STORAGE RESOURCE ASSESSMENT IN SOUTHEAST OF JEFFERSON COUNTY, OFFSHORE TEXAS, USA



Ruba Afifi, MSc in Geological Sciences

The University of Texas at Austin, 2026

Supervisors: Timothy A. Meckel & Carlos A. Uroza



Carbon Capture and Geologic Sequestration (CCGS) has been demonstrated as an effective strategy for limiting the increasing impacts of anthropogenic greenhouse gas (GHG) emissions from industrial activities. The northern Gulf of Mexico (GOM) offers significant potential for large-scale subsurface storage, as indicated by the region's history of hydrocarbon exploration and production. Previous regional studies have analyzed subsurface data from the Lower and Middle Miocene Series and estimated a total static storage capacity of 129 $GtCO_2$ in the northern GOM, with the highest capacity density of 20 Mt/mi$^2$ (~7.5 Mt/km$^2$) located offshore southeast Texas (Wallace et al., 2014; Treviño and Meckel, 2017). These estimates were then reduced to ~4.7 Mt/mi$^2$ (1.8 Mt/km$^2$) when dynamic constraints (i.e., pressure and time) were incorporated into the capacity estimation methodology. The present study focuses on a region in southeast Texas, where an approximately 11,500-square-mile (30,000 km$^2$) delta lobe system prograded across the margin during the Early Miocene Epoch. The primary objectives are to identify geologic

storage prospects in this area and to constrain storage resource estimates. The Society of Petroleum Engineers' $CO_2$ Storage Resources Management System (SRMS) defines storage resource as "the quantity (mass or volume) of $CO_2$ that can be stored in a geologic formation in commercial quantities" (SRMS, 2022).

This study uses detailed geologic interpretation and site-specific characterization to identify storage prospects and refine resource estimates in the inner continental shelf of southeast Jefferson County, Texas. Three-dimensional seismic data and well logs are used to characterize the Lower Miocene stratigraphy, which is notable for its porosity, thickness, and extensive lateral and vertical continuity, creating favorable conditions for geologic carbon storage (Treviño and Meckel, 2017).

Key bio-stratigraphic surfaces associated with regional marine flooding events bound the interval of interest above and below with thick, extensive shales. The Lower Miocene 2 (LM2) interval contains thick interbedded sands and shales deposited by the progradation of deltaic systems toward the basin. The primary uncertainties in geologic characterization for storage assessment are related to the variability of sandy reservoir lateral extent and fault compartmentalization. In addition to structural mapping and well log interpretation, this study applies seismic attribute analysis to map sand extent between wells, enabling the construction of a three-dimensional static geologic model to identify storage prospects and assess their individual storage resources using two methods: (1) the static volumetric method (Goodman et al., 2011) and (2) the dynamic pressure-based analytical method, EASiTool (Hosseini et al., 2018).

The three-dimensional geological model pointed to a prospective area characterized by thick (approximately 280 ft) and laterally continuous sandstone with an average porosity of 21%, dipping and thickening toward the south and southeast. In the up-dip direction toward a salt diapir, the extent of the sandstones remains uncertain, particularly regarding the compartmentalization of injected $CO_2$. The prospect is bounded by two growth faults parallel to the dipping beds, which are evaluated as pressure boundary conditions in EASiTool simulations.

Volumetric capacity estimates are approximately 34 Mt for 1% storage efficiency (P90), 485 Mt for 14% (P50), and 1998 Mt for 50% (P10). EASiTool estimates for maximum storage capacities range from 96 to 789 Mt, with a P50 estimate of 320 Mt for open boundaries. In contrast, closed boundary scenarios yield capacities ranging from 3.7 to 9.3 Mt, with a P50 of 6 Mt. These results indicate that, for this reservoir, open-boundary EASiTool estimates correspond to storage efficiencies of 3-7% and closed-system estimates yield storage resrources corresponding to <0.5% storage efficiencies for a 20-year injection period.

This research has proven the storage potential of the Lower Miocene interval in Texas State Waters by constraining $CO_2$ storage resource estimates for the geologic site at the screening level and by applying a normalized capacity metric per area and per thickness for validation against other studies in the vicinity. Future steps for this storage site should incorporate multi-phase flow reservoir models to validate storage resource estimates from this study and to delineate the $CO_2$ plume for further project development.

## Table of Contents

# List of Tables

## List of Figures

# Chapter 1: Introduction

This chapter provides background information relevant to this research. The first section explains the motive for Carbon Capture and Geologic Storage (CCS). The next section describes the geologic setting of the Northern Gulf of Mexico (GOM) with an emphasis on the structural and stratigraphic framework of the Lower Miocene Series. The following section synthesizes previous work on geologic characterization and/or CCS assessments in and near the study location. The final section introduces the scope and objectives of this research.

## 1.1 Carbon Capture and Geologic Storage

The global climate change observed today is a direct consequence of increased greenhouse gas (GHG) emissions driven by human activities since the Industrial Revolution. The International Energy Agency's 2025 Global Energy Review reports that global $CO_2$ concentrations in the atmosphere have increased by 53% since pre-industrial levels, primarily due to fossil fuel combustion (IEA, 2025). The 2023 Intergovernmental Panel on Climate Change (IPCC) reports that since 1850, annual $CO_2$ emissions have been $45 \pm 5.5$ $GtCO_2$ per year, bringing the cumulative $CO_2$ emissions to $2400 \pm 240$ $GtCO_2$ in 2019. Around 84% of annual $CO_2$ emissions come from fossil fuels and industry (IPCC, 2023). In order to effectively mitigate the atmospheric effects of GHGs, 5-10 gigatons of $CO_2$ must be removed annually to stay below a 2°C net average temperature increase by the year 2100 (Dhakal et al., 2022).

Large-scale carbon capture and geologic storage is needed to remove gigaton-scale volumes of anthropogenic $CO_2$ from the atmosphere over the coming decades (IPCC, 2023). Geologic carbon sequestration in depleted hydrocarbon reservoirs or saline aquifers is the most effective strategy for storing such large volumes, but screening for potential storage sites requires a clear understanding of subsurface geologic conditions, volumetric storage resources, and the potential subsurface response to $CO_2$ injection.

The northern Gulf of Mexico (GOM) sedimentary basin is a highly prospective region for potential CCS deployment for several reasons. First, there is an abundance of high-quality subsurface data from historical hydrocarbon exploration and production, which lowers the costs associated with subsurface data acquisition and processing. Secondly, the Gulf Coast is one of the largest regional emitters in the country, with more than 390 point-source facilities that emitted a total of 20.1 $MMtCO_2e$ as of 2023 (EPA GHGRP, 2023). The proximity to large-volume point-source emitters, such as oil refineries and power plants, lowers $CO_2$ pipeline transportation costs. Finally, the Gulf Coast's regional geology is proven suitable for buoyant fluid trapping, as evident by the many hydrocarbon-producing fields in the region (Figure 1.1; Treviño and Rhatigan, 2017; Treviño and Meckel, 2017).

As of the time of writing this thesis, there are no active saline aquifer storage projects in the Gulf Coast yet. However, there are multiple ongoing $CO_2$ Enhanced Oil Recovery (EOR) projects (e.g., West Ranch and Hastings projects) and active leases in the area, including offshore in the vicinity of the study area (Figure 1.1). Currently, global $CO_2$ storage capabilities are still in the megaton (million metric tons) scale, nowhere near the gigaton (billion metric tons) scale required to stay below the 2°C mark by 2100. This research explores storage resource assessment for saline prospects in clastic sandstone formations for CCS in Southeast Texas and estimates their potential storage resource.

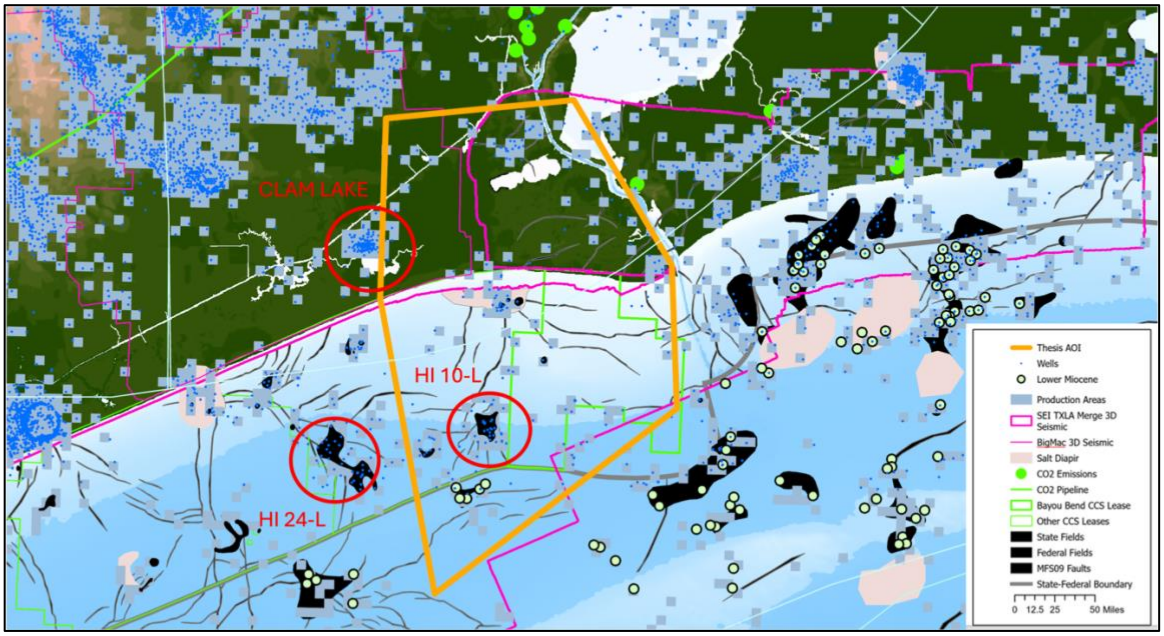


Figure 1.1: Regional basemap showing the relevant data around the study area (orange polygon). Red circles mark the locations of hydrocarbon fields discussed in this research. The boundaries of the study area were arbitrarily drawn to include the area with the highest capacity density (based on regional studies) and cover the faulted region east of the depleted fields (some of which were previously assessed for $CO_2$ storage).

## 1.2 Geologic Setting: Northern Gulf of Mexico

The Gulf of Mexico is one of the most extensively researched sedimentary basins in the world. The structural and depositional frameworks are well-recorded from its initial rifting in the Early Mesozoic to the last depositional episode in the Late Cenozoic (Ewing and Galloway, 2019; Snedden and Galloway, 2019). For this thesis, the geological context discussion will be limited to the present-day topography and bathymetry (Figure 1.2) and geological history of the relevant stratigraphic interval within the $CO_2$ storage window, which can generally be described as below supercritical depths (~3000 ft depth in the area of study), and above geopressured stratigraphy (~9000 ft depth in the area of study).

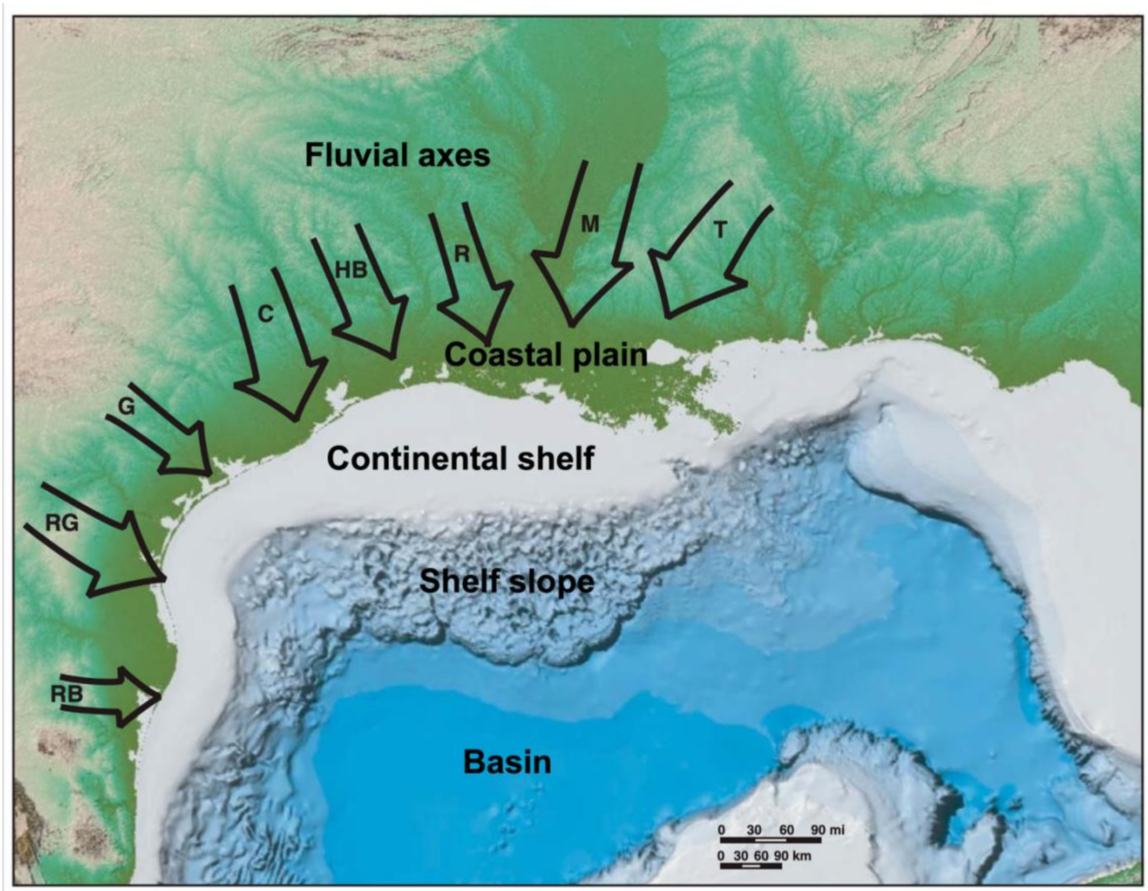


Figure 1.2: Topographic basemap (present day) showing Cenozoic fluvial axes in the Gulf of Mexico. RB=Rio Bravo; RG=Rio Grande; G=Guadalupe; C=Colorado; HB=Houston-Brazos; R=Red; M=Mississippi; T=Tennessee (modified from Galloway et al., 2011)

### 1.2.1 Paleogeographic history

The GOM basin was formed by seafloor spreading through the Middle Jurassic to Early Cretaceous time. The northern margin is characterized by a broad coastal plain and shelf, rimmed with a series of temporally well-defined shelf edges and continental slope successions (Figure 1.2, Galloway et al., 2011). Clastic sediment supply from the Laramide uplands in the northwest was low throughout the Cretaceous due to the interference of a foreland seaway, isolating the basin from sediments (Galloway, 2008). Starting from the Late Paleocene time, high volumes of clastic sediments began to enter the basin from the continental North American uplands through multiple fluvial-deltaic axes (Figure 1.2; Figure 1.3), initiating the progradation of the continental margin and depositional offlap that continued throughout the Cenozoic (Galloway et al., 2011; Snedden and Galloway, 2019).

During Oligocene time (~8 Ma), the northern shelf margin went through an extensive period of sediment supply—causing the progradation of fluvial-deltaic systems across the continental shelf and ended with a regional marine flooding event that deposited the Anahuac shale, marking the Oligocene-Miocene boundary (Snedden and Galloway, 2019).

The Miocene Epoch marks a period of increased sediment supply and extensive progradation of the continental margin, triggering growth faults and salt tectonics (Galloway et al., 2011). The Early, Middle, and Late Miocene record the progressive shift of the depositional locus from the northwest to the central and northeastern margins of the Gulf (Galloway et al., 2011). The Mississippi axis continued its long history of clastic sediment supply at the depocenter in present-day central Louisiana coast (Figure 1.3; Figure 1.4). To its west, the newly formed Red River fluvial axis was slowly traversing to the east and supplying the Calcasieu delta with sediments at the easternmost Texas coastal plain. These two deltaic systems are the principal depositional elements for the Early Miocene interval of interest (Ewing and Galloway, 2019; Snedden and Galloway, 2019).

At the northern GOM margin, the Early Miocene Epoch recorded continued deltaic and shoreline progradation while increasing sediment supply across the Anahuac transgressive shelf, leaving extensive shoreface and delta-fed slope facies consisting of interbedded sandstones and shales (Ewing and Galloway, 2019; Snedden and Galloway, 2019). By the end of the Early Miocene, a period of retrogradation and regional marine transgression deposited the regionally extensive Amphistegina B (Amph. B) Shale, marking the end of the Early Miocene depositional episode.

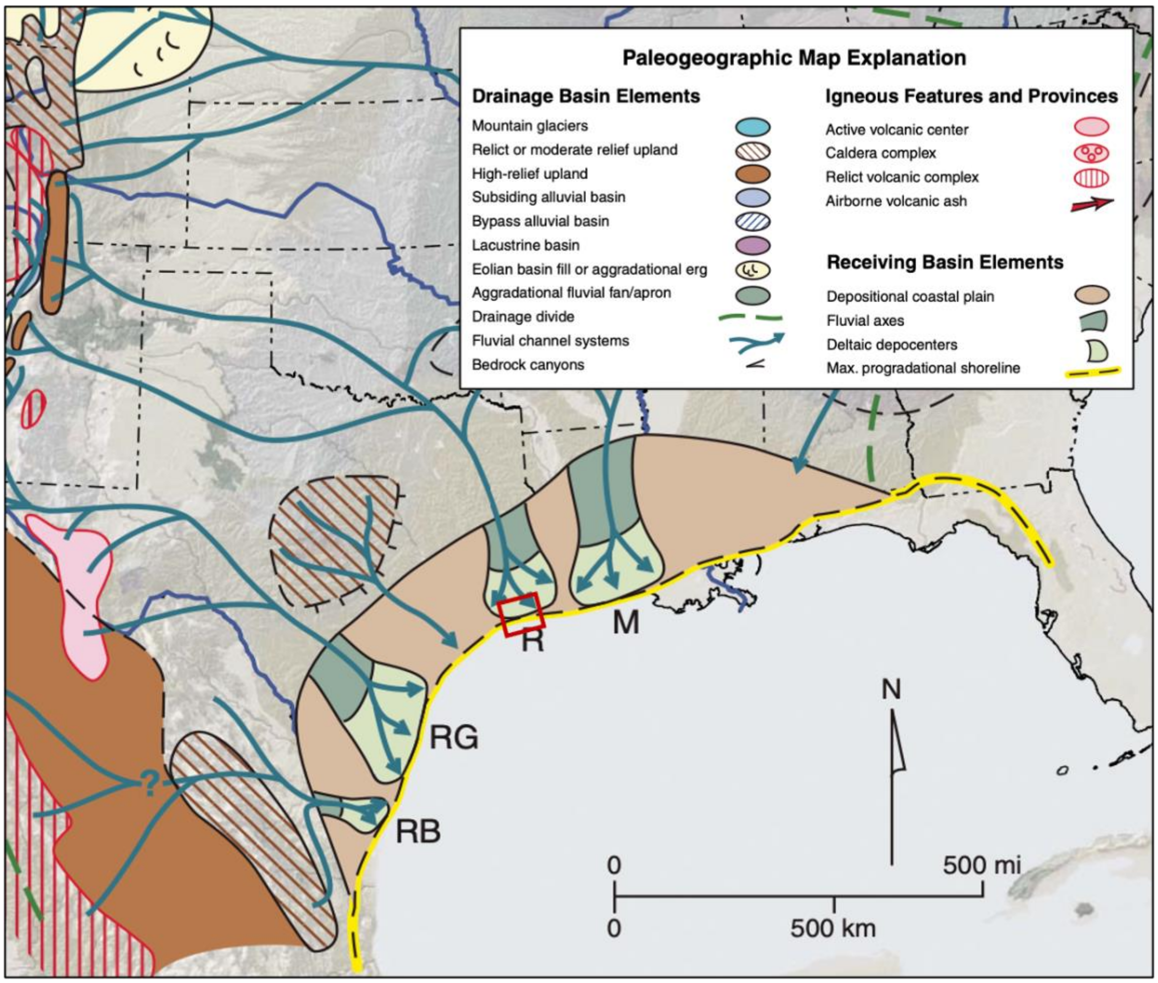


Figure 1.3: Paleogeographic map of the Northern Gulf of Mexico during the Early Miocene. RB=Rio Bravo; RG=Rio Grande; R=Red; M=Mississippi. The study area is shown in a red box (modified from Galloway et al. 2011).

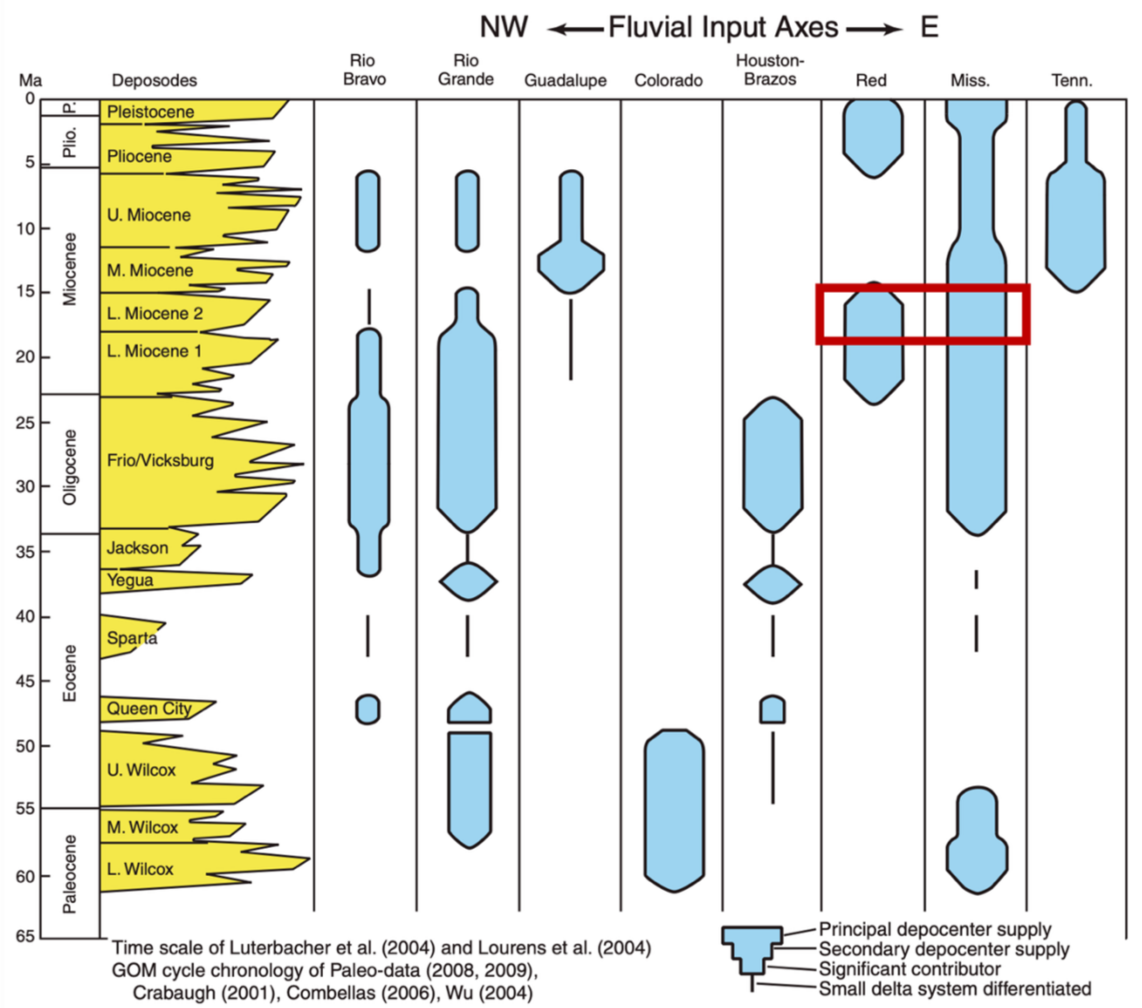


Figure 1.4: Temporal history of the fluvial input axes at the northern Gulf of Mexico basin margin. Axes are arranged according to geographic position. The width of the blue bar expresses the relative importance and contribution from each axis. Note the dominant fluvial axes during the Lower Miocene 2 depositional episode in the area of study indicated by red rectangle (modified from Galloway et al., 2011).

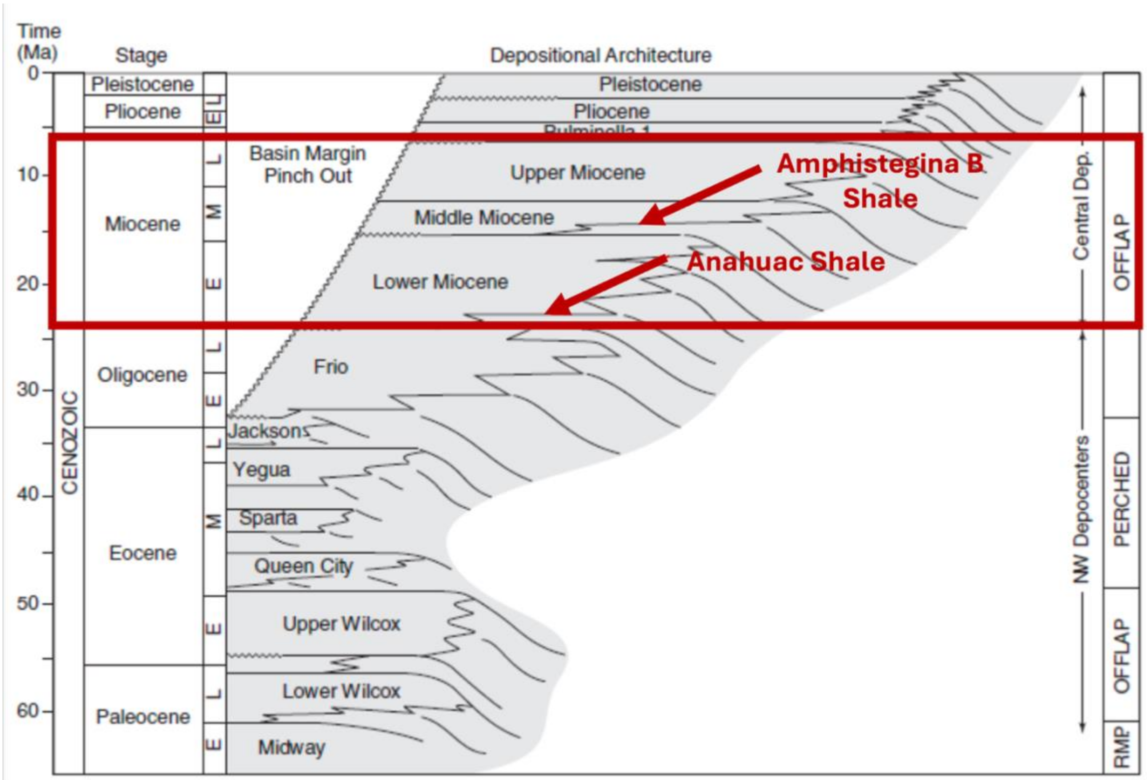


Figure 1.5: Cenozoic stratigraphic section in the Northern Gulf of Mexico, with Miocene stratigraphy outlined in red box. Red arrows point to regressions (marine flooding events) that bound the Lower Miocene interval of interest (modified from Galloway, 2008).

### 1.2.2 Stratigraphic framework

The Early Miocene Series in the northern GOM continental shelf is a target candidate for CCS for its extremely favorable reservoir qualities (thickness, extent, porosity, permeability, and trapping) that were shaped by prograding delta systems with high clastic sediment influx into the basin (Treviño and Meckel, 2017). Figure 1.6 is an analog model for the stratigraphy and scale of coastal deltaic system and their systems tracts (Paola et al., 2001).

The Early Miocene stratigraphic record consists of genetic supersequences that formed over two depositional episodes, which Galloway et al. (2000) named Lower Miocene 1 and 2 (LM1 and LM2, respectively) (Figure 1.7). These two depositional episodes of progradation are separated by a transgressive event recorded in the Marginulina Shale, associated with the *Marginulina* A and *Robulus* L benthic forams (Snedden and Galloway, 2019). The Lower Miocene progradational strata are capped with a more extensive transgressive shale, the Amph. B Shale, named for the *Amphistegina* B benthic foram marker (Galloway, 1989; Galloway et al., 2011). These major transgressive events are marked in the sedimentary record as Marine Flooding Surfaces (MFS) (Figure 1.7).

In this thesis, the LM2 depositional episode is identified as the Storage Interval of Interest (SIOI), bounded by the regional marine flooding surfaces MFS9 and MFS10 in the offshore log record (see Figure 1.7, Olariu et al., 2019). The parasequences of the SIOI consist predominantly of prograding coastal-deltaic and shallow marine sandstones and shales, overlain by thick transgressive Amph. B shale (Galloway, 1989; Galloway et al., 2011; Treviño and Meckel, 2017; Ewing and Galloway, 2019). Van Wagoner et al. (1990) illustrates how the stacking patterns can be observed in the log record (Figure 1.8). Well log correlation is covered in Chapter 2 of this research.

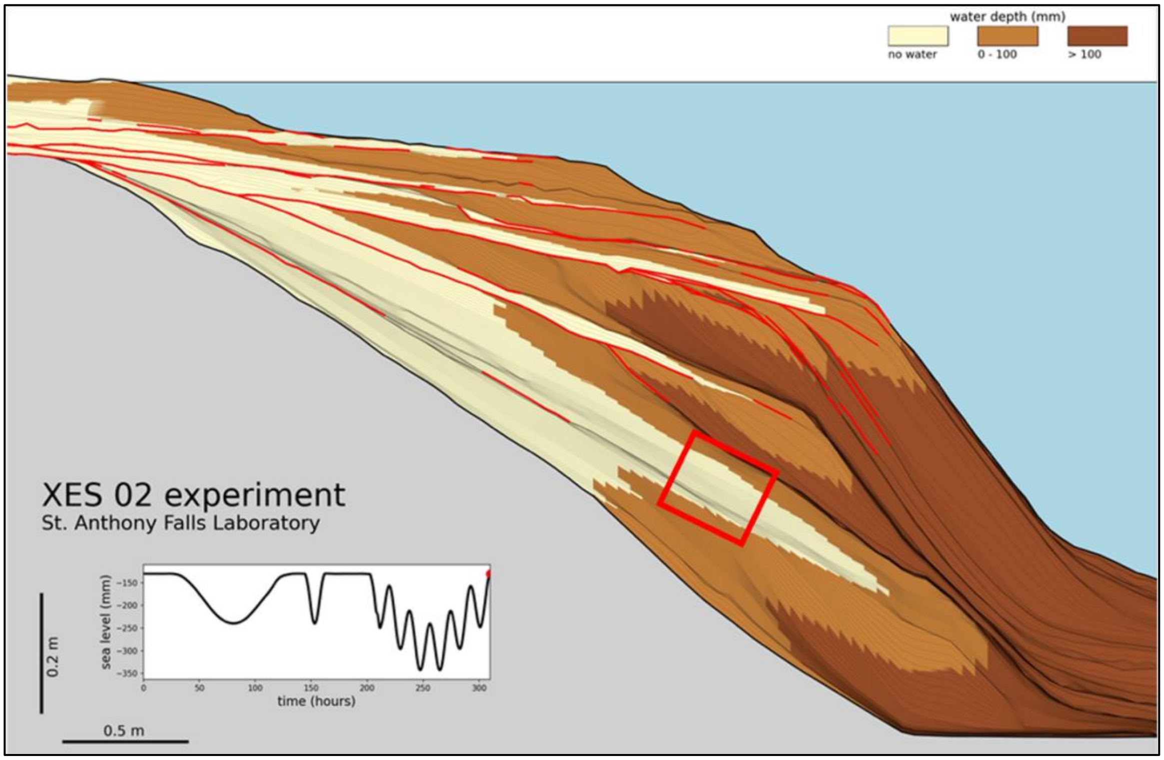


Figure 1.6: Geological delta model from laboratory sand-tank experiments in St. Anthony Falls Laboratory, demonstrating the depositional architecture of a coastal delta system and systems tracts, with a red box outlining what would be the position of the LM2 interval in the study area (modified from Paola et al., 2001).

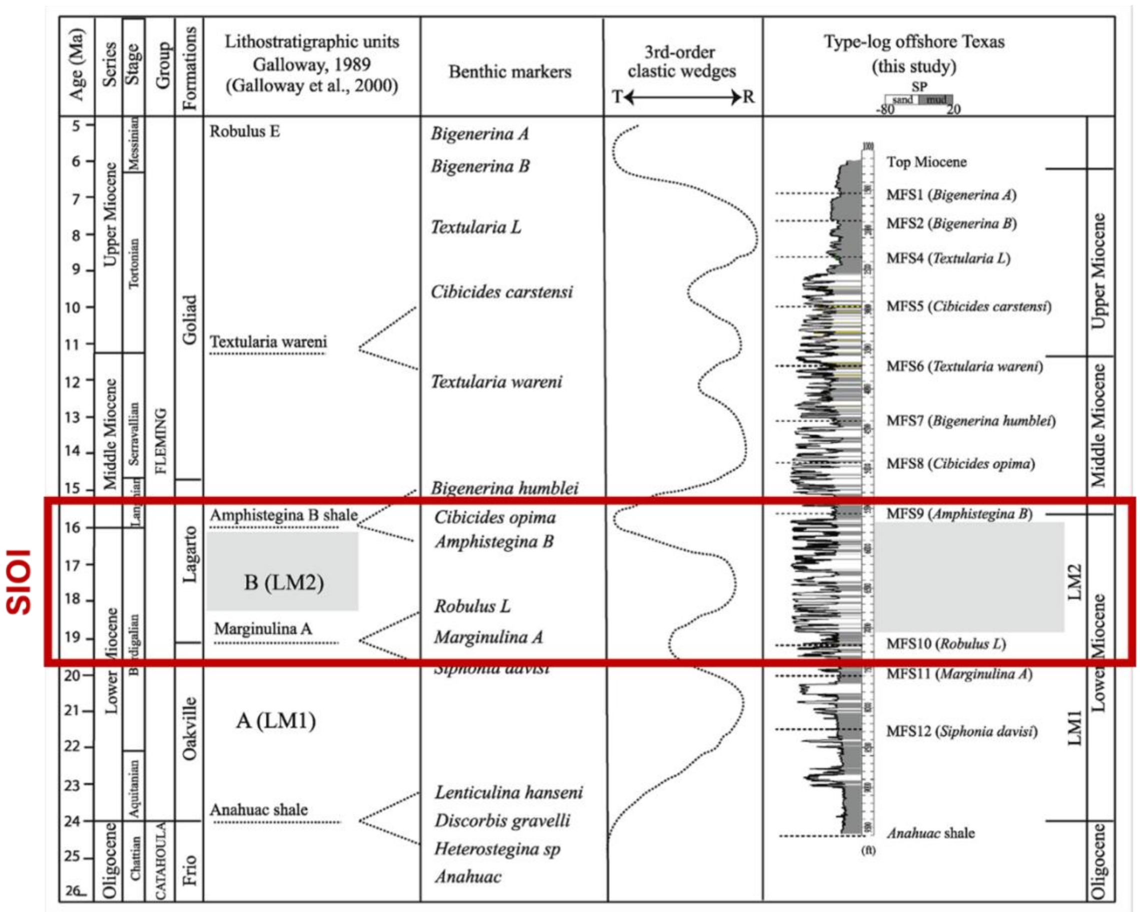


Figure 1.7: Stratigraphic section and type log offshore Texas (modified from Olariu et al., 2019). The red box outlines the Lower Miocene 2 (LM2) storage interval of interest and relevant stratigraphic markers.

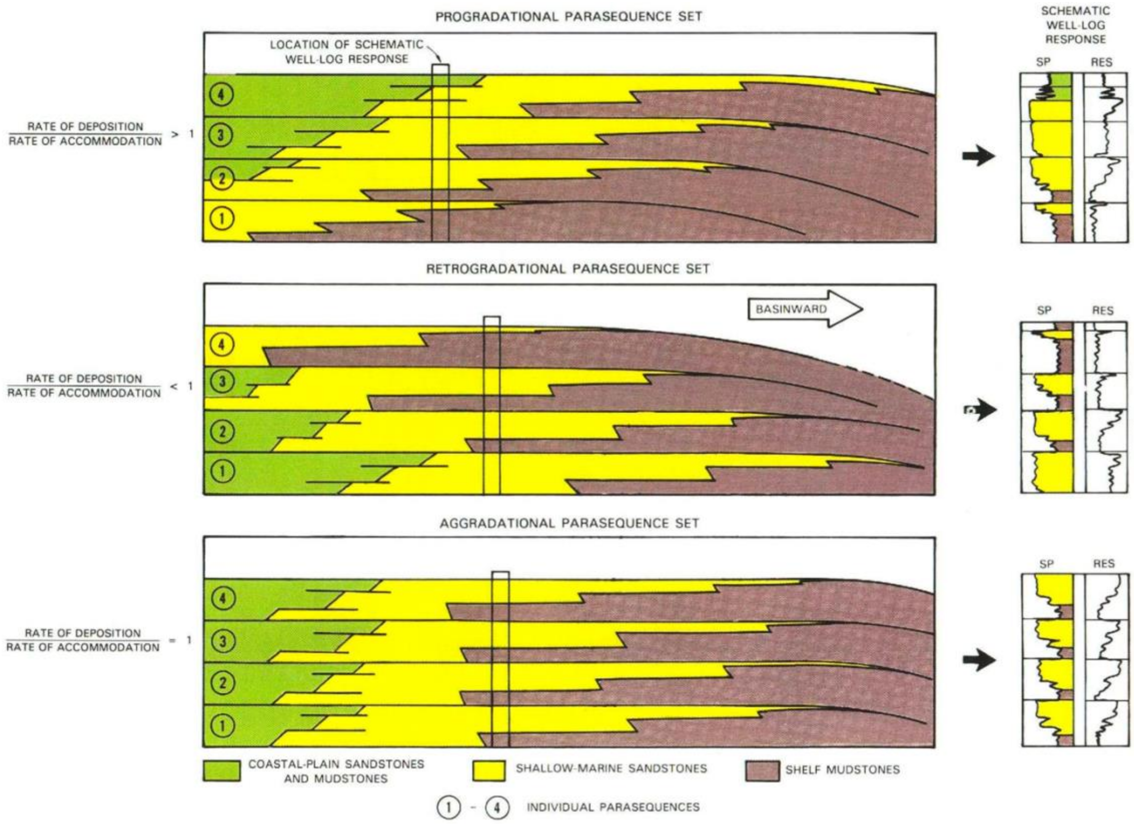


Figure 1.8: Schematic of stacking patterns of different types of parasequence sets (progradational, retrogradational, and transgressive) of a passive margin and their corresponding well log response (Van Wagoner et al., 1990).

### 1.2.3 Structural framework

During the Early Miocene, the northern Gulf margin was dominated by a suite of structurally distinct domains shaped by interaction of rapid clastic progradation, salt tectonics, and differential subsidence (Figure 1.9). These domains, bounded by the shelf edge and extending basinward toward the deep basin hinge, were integral in controlling Early Miocene sediment distribution, structural relief, and accommodation patterns across the northern Gulf margin (Snedden and Galloway, 2019).

The shelf and coastal plain record extensive growth-fault systems and margin-parallel extensional deformation driven by salt diapirism, deltaic loading and sedimentary progradation into the deep basin, producing the Oligocene–Miocene detachment structural domain that dominates onshore and near-shelf regions of Texas and Louisiana (Snedden and Galloway, 2019). Basinward, thick sequences of delta-derived siliciclastics accumulated over the underlying mobile Louann Salt and unstable Frio strata (Ewing and Galloway, 2019), resulting in broad areas of growth faults, active salt diapirism, and mini-basin development where listric faults and rollover anticlines partition accommodation space (Figure 1.9). This study includes an analysis on the structural changes within the LM2 and discusses its implications on the interplay between sediment supply and active deformation by salt growth and faulting during the LM2 depositional episode.

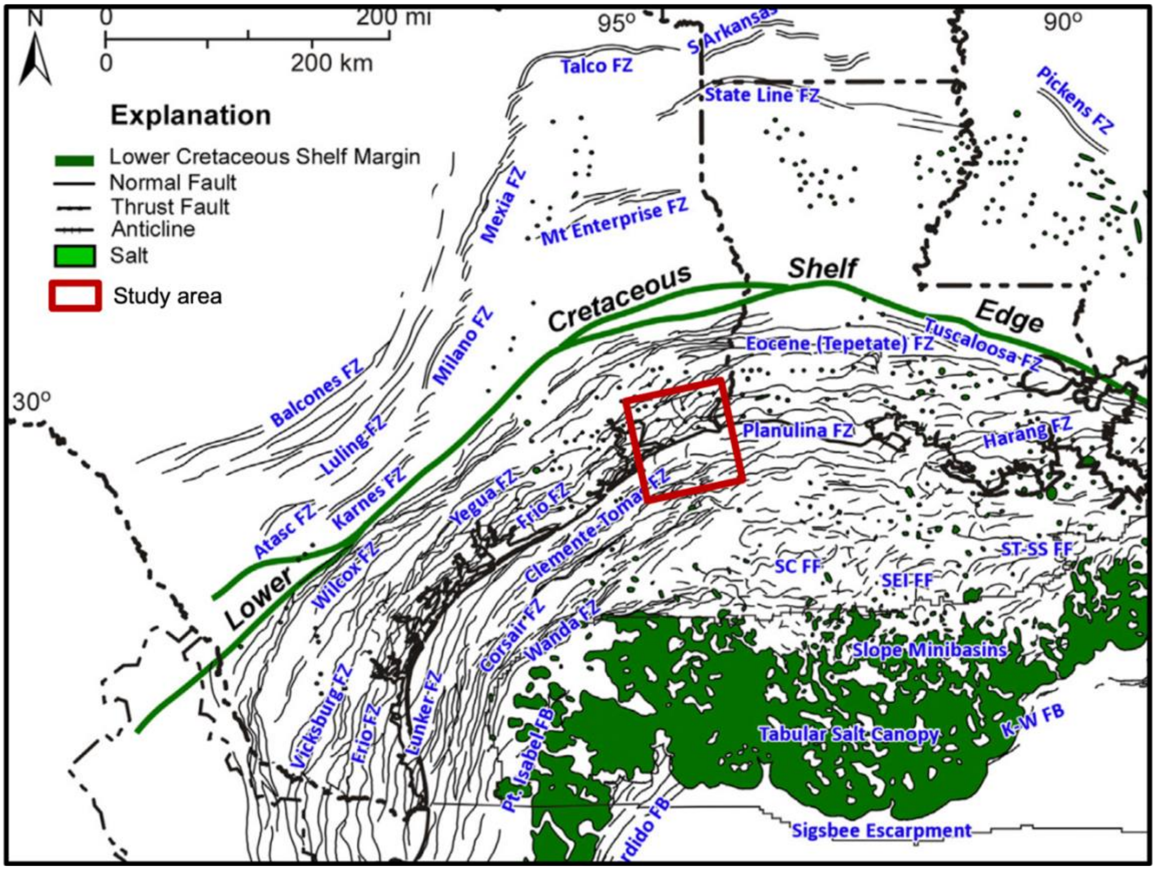


Figure 1.9: Gravity-Tectonic structural elements of the Northern Gulf of Mexico basin (modified from Ewing and Galloway, 2019).

## 1.3 Previous Work

### 1.3.2 Regional $CO_2$ storage resource assessment studies

Many regional studies have assessed site suitability for permanent $CO_2$ storage in Early Miocene stratigraphy offshore Texas and Louisiana (Carr et al., 2011; Wallace et al., 2014; Carr et al., 2016; Carr et al., 2017; Treviño and Meckel, 2017; Beckham, 2018; Ramirez Garcia, 2019; Ruiz, 2019; DeAngelo et al., 2019; Bump et al., 2021; Bump and Hovorka, 2023). Their depth position within the $CO_2$ storage window (below supercritical pressure-temperature conditions and above hard reservoir overpressure), and their proven ability to trap hydrocarbon accumulations, make them a world-class candidate for permanent $CO_2$ storage (Treviño and Meckel, 2017). The top of the storage window is defined by the critical depth of 1 km (~3000 ft), below which $CO_2$ is in supercritical state with low volume and high density. The base of the storage window is marked by the top of formation overpressure, which ranges from 2.7 to 3.3 km depth (8800 – 10,800 ft) in the area of study (Bump and Hovorka, 2024).

The US Department of Energy (DOE) National Energy Technology Laboratory (NETL) has determined that for a site to be economically feasible, a minimum of 30 Mt$CO_2$ storage capacity is required. They have developed a deterministic approach widely used to estimate the storage resources for a saline aquifer using a volumetric equation, where the static capacity is a product of total porosity, bulk volume, $CO_2$ density, and a storage efficiency factor (Goodman et al., 2011):

$$M_{CO2} = A_t h_g \phi_{tot} \rho_{CO2} E_{saline} \tag{1.1}$$

where,

$M_{CO2}$ = $CO_2$ storage resource mass estimate (kg; where 1 metric ton (tonne) = 1000 kg, and 1 Mt = $10^6$ metric tons)

$A_t$ = total area ($m^2$)

$h_g$ = gross formation thickness (m)

$\phi_{tot}$ = total porosity (unitless)

$\rho_{CO2}$ = $CO_2$ density at reservoir conditions (kg/$m^3$)

$E_{saline}$ = storage efficiency factor for saline aquifers (unitless)

This method represents a straightforward and fast evaluation of storage resources, but the accuracy largely relies on the storage efficiency factor ($E_{saline}$), which remains one of the most debated parameters in geologic $CO_2$ storage resource assessment because it represents the fraction of pore volume that can realistically be occupied by injected $CO_2$ while implicitly accounting for complex processes such as reservoir heterogeneity, sweep efficiency, residual trapping, and pressure limitations (Goodman et al. 2011; Goodman et al., 2013). This thesis includes the use of this methodology to estimate the storage resources for an identified storage site in Chapter 4.

Goodman et al. later developed probabilistic efficiency factors as part of the DOE-NETL methodology to provide a consistent framework for estimating prospective storage resources at regional and basin scales where detailed reservoir characterization and simulation data are unavailable. These authors emphasized that storage resource estimates are inherently uncertain due to simplifying assumptions and limitations in available subsurface data (Goodman et al., 2013).

Subsequent work by Bachu (2015) highlighted that storage efficiency is not a fixed physical property of a reservoir, but rather a scale-dependent parameter that varies with geology, boundary conditions, injection strategy, and assessment methodology. More recently, Wang et al. (2024) noted that $CO_2$ storage resources are constrained not only by available pore volume but also by maximum allowable pressure buildup, demonstrating that uncertainty in pressure-related parameters can strongly influence estimated storage efficiency. As a result, although volumetric methods remain useful for screening-level assessments, there is growing recognition that storage efficiency factors should be interpreted as uncertain screening-level assessment parameters rather than direct measures of achievable project-scale storage capacity (Goodman et al. 2013; Wang et al., 2024).

Multiple $CO_2$ storage resource estimation studies have been done for Lower Miocene stratigraphy in the northern Gulf. According to studies and reports compiled by

Treviño and Meckel (2017), offshore Texas State Waters hold a net capacity of 30 $GtCO_2/km^2$, with an estimated 2.5 $GtCO_2$ that can be stored in the Gulf Coast fields for enhanced oil recovery (EOR) (Carr et al., 2017). Wallace (2013) reports of a total 129 $GtCO_2$ storage capacity (static estimate), with the highest capacity density being offshore southeast Texas (Figure 1.10).

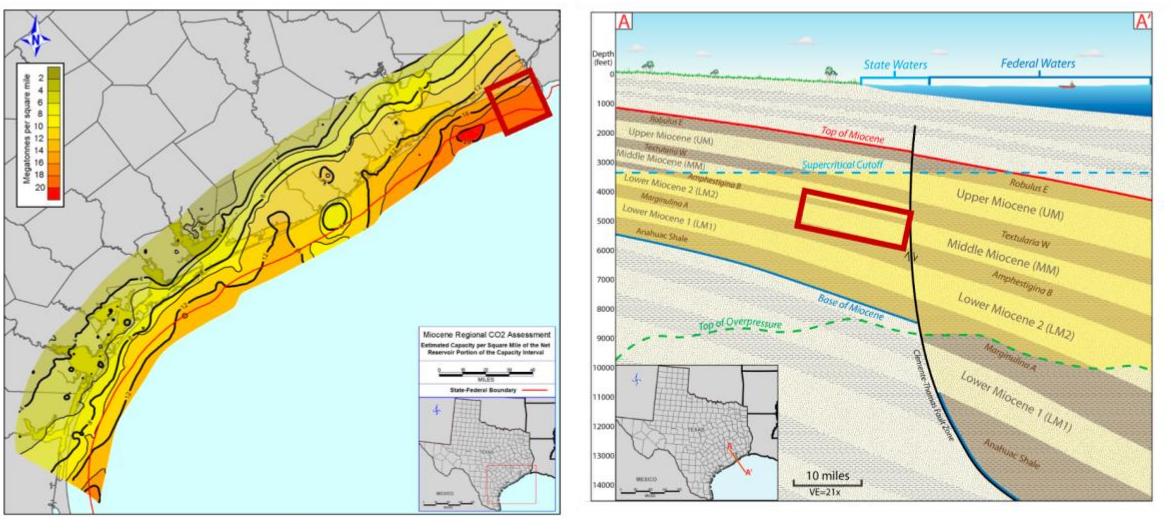


Figure 1.10: Left: Map showing $CO_2$ storage capacity per square mile for a net reservoir portion of the storage interval (modified from Wallace, 2013). Right: Schematic cross section across the northern Gulf margin, highlighting the $CO_2$ storage window (modified from Wallace et al., 2014). Red boxes outline the area of study on the left, and the interval of interest on the right.

DeAngelo et al. (2019) used a seismic-based workflow to identify and rank structural closures on a regional scale, relying on the concept of "fetch-trap" pairs. Fetch-trap pairs, as defined by Bump and Hovorka (2023a), use structural contours to map prospects that include both a migration route and a trap. "Fetch area" refers to the subsurface drainage area that feeds a given trap. Fetch area boundaries can include geological features, such as faults and synclinal axes, that divide drainage directions (Bump and Hovorka, 2023a).

The business risks of CCS in the northern Gulf margin have also been assessed to encourage investment. A study by Bump et al. (2021) used Composite Common Risk Segment (CRS) mapping, a common practice in the petroleum exploration industry, to assess the risks of CCS using geological maps as inputs (reservoir presence, reservoir quality, and seal capacity) constrained by a large dataset in the northern Gulf Coast. The resulting composite CRS map highlights minimal costs on coastal southeast Texas and Louisiana (Figure 1.11; Bump et al., 2021).

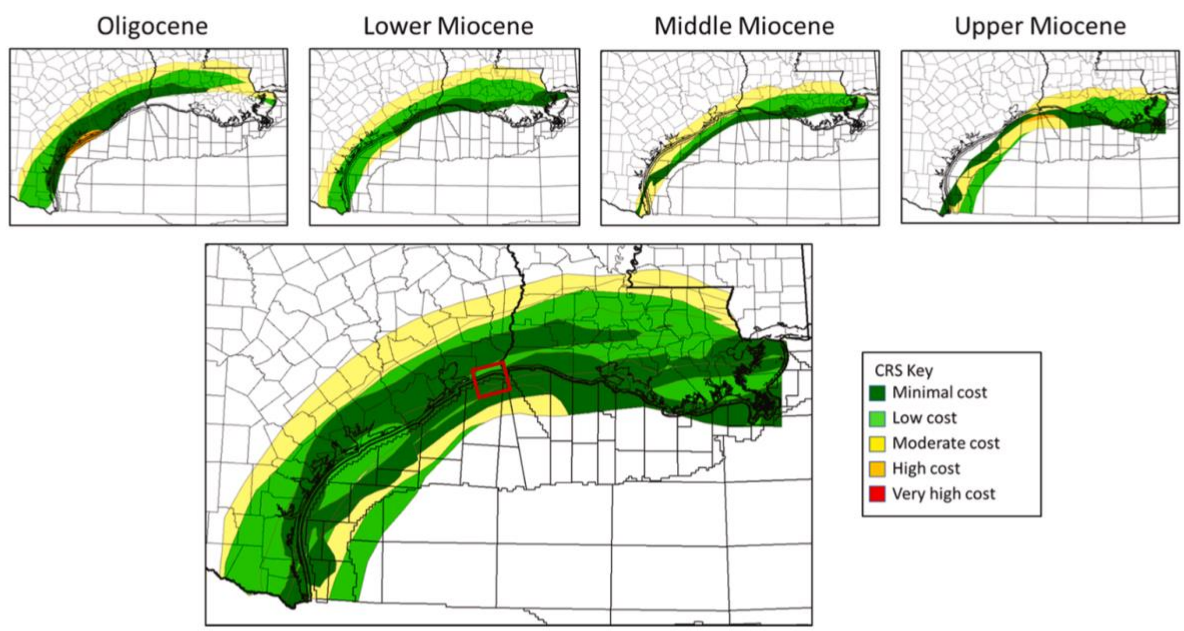


Figure 1.11: Composite CRS map for the Oligocene, Lower Miocene, Middle Miocene, and Upper Miocene (top row), and a combination (bottom row), modified from Bump et al. (2021). Red box outlines the area of study.

Other studies highlight the favorability of CCS in the northern Gulf Coast with lab experiments and dynamic reservoir modeling to prove the concept of "composite confining systems" for permanent $CO_2$ storage in the Lower Miocene interval (Figure 1.12). Unlike hydrocarbon trapping, $CO_2$ does not require one thick and effective seal, and the presence of multi-layered thin sealing units is enough to retard the vertical migration of $CO_2$, depending on their geometry and configuration (Bump et al., 2023; Ni et al, 2024).

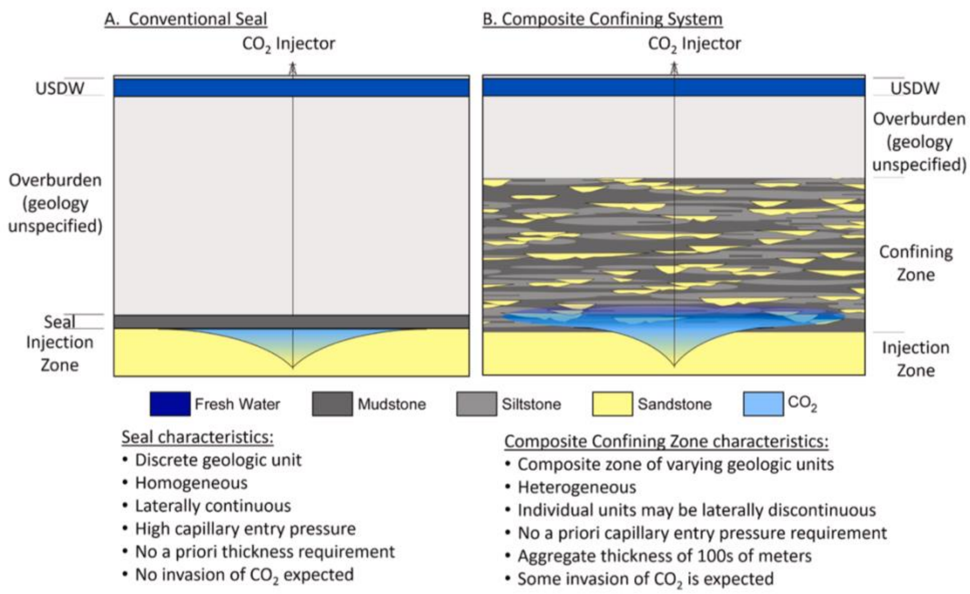


Figure 1.12: Schematic diagram illustrating the similarities and differences between (A) conventional seals, and (B) composite confining systems (from Bump et al., 2023). "USDW" refers to Underground Sources of Drinking Water.

While regional studies show promising storage capabilities in the northern Gulf Coast, the estimated capacities are likely highly inflated due to data sparsity and the use of 'static' capacity, which assumes that all pore space will be saturated with $CO_2$ (with an assumed efficiency factor). A study by Bump and Hovorka (2024) mapped the storage resource while considering depth-dependent nonlinear reservoir properties, including available pressure space, compressibility, and $CO_2$ density at reservoir conditions. The resulting storage resource maps refine the work of Wallace et al. (2014) in Miocene reservoirs near the area of study, with total (dynamic) storage resource reaching up to 1.8 $MtCO_2/km^2$ (4.7 $Mt/mi^2$), reducing the estimated storage resource for the AOI by nearly five times when compared to static estimates from Wallace et al. (Figure 1.13, Bump and Hovorka, 2024).

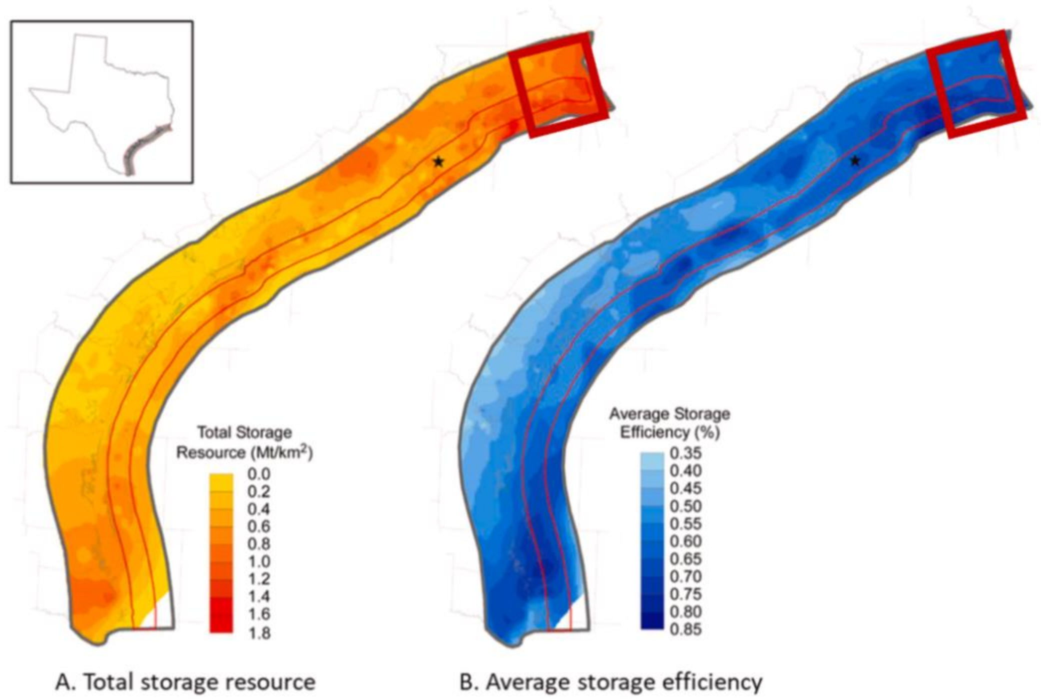


Figure 1.13: Result maps of A) pressure-based dynamic storage resource calculation for the Texas coastal Miocene, and B) the average storage efficiency. The area of study is outlined by a red box (modified from Bump and Hovorka, 2024).

Regional studies, including the ones just mentioned, are only part of the early stages of CCS screening. After identifying favorable areas, small-scale assessments must be conducted to refine storage resource estimations (Wallace, 2013; Wallace et al., 2014;

Treviño and Meckel, 2017; DeAngelo et al., 2019; Ramirez Garcia, 2019; Ruiz, 2019; Zulqarnain et al., 2023).

### 1.3.2 Field-scale $CO_2$ storage resource assessment studies

There are multiple depleted oil and gas reservoirs with known volumetrics, properties, and original hydrocarbon-in-place estimates in the northern Gulf Coast. This information can be used to assess the same sites for $CO_2$ storage. This subsection will consider three depleted hydrocarbon fields near the area of study. These settings represent analogs for the sizes of buoyant fluid accumulations resulting from geologic processes. Two of these depleted fields have been evaluated for potential $CO_2$ storage resources in prior studies (Beckham, 2018; DeAngelo et al., 2019; Ruiz, 2019).

#### ***High Island 10L field***

The High Island 10L field (Figure 1.1) was first discovered in 1955. It is located 13.5 miles southwest of Sabine Pass in Texas State Waters. In 2019, the Texas Railroad Commission (RRC) reported approximately 1 MMbbl of oil from several sands beneath the Amph. B shale, and approximately 8.6 Bcf of gas (Ramirez Garcia, 2019).

The producing sandstones were grouped into five plays with distinctive characteristics by Seni et al. (1997), four of which are beneath the Amph. B shale with stacking patterns consistent with a prograding deltaic system and occasional flooding events:

1. LM2 P.1B (Middle Lower Miocene)  progradational stacking pattern
2. LM4 P.4 (Middle Lower Miocene)  progradational
3. MM4 A.1B (Lower Middle Miocene)  aggradational
4. MM4 R.1. (Lower Middle Miocene)  retrogradational

The documented porosities of the producing sands range from 29% to 33%, and permeabilities range from 465 to 790 mD. The trapping mechanism for this field is structural, as an anticline formed by rollover structures associated with growth faults (Seni, 1997; Ramirez Garcia, 2019).

The 10L field's feasibility for CCS has been previously assessed by Beckham (2018) by integrating historical hydrocarbon production with key stratigraphic surfaces for fluid flow prediction. The study concluded that the reservoir is indeed able to retain fluids with low connectivity between individual deltaic sands.

DeAngelo et al. (2019) assessed the storage resource of the 10L field closure using two methods. The first method involved volumetric fluid replacement, specifically using the $CH_4$-$CO_2$ Volumetric Replacement Assessment developed by Meckel and Rhatigan (2017). The potential $CO_2$ storage resource was found to be at least 0.43 $MtCO_2$. However, this represents an underestimation due to the unfilled reservoirs and structures in the field, and the utilization of a relatively thin geologic interval. The second method used bulk volume from closure analysis, and the DOE formula from Goodman et al. (equation 1.1), to calculate the pore volume available for storage with different storage efficiency factors of 10%, 25%, and 50% (DeAngelo et al., 2019). However, the efficiency factors used here are higher than the published efficiency factors for saline clastic aquifers (Goodman et al., 2011; Bachu, 2015). The estimated $CO_2$ storage resources between MFS9 and MFS10 were found to range between 16 and 120 $MtCO_2$, with a P50 estimate of approximately 50 $MtCO_2$ (DeAngelo et al., 2019).

Ramirez Garcia (2019) estimated the storage resource of this field using both static and semi-dynamic modeling techniques built on site-specific and detailed characterization, integrating petrophysical properties with structural elements. The total static capacity calculated an average P50 value of 28.25 $MtCO_2$ within six reservoir layers in the Lower Miocene (Ramirez Garcia, 2019).

***High Island 24L field***

The High Island 24L field (Figure 1.1) was first discovered in 1967. It is located 9 miles northwest of the High Island 10L field and is considered a volumetrically significant hydrocarbon field with several plays within the Lower Miocene sands. The field is reported to have produced a cumulative of 470 Bcf of natural gas and around 4.5 MMbbl of oil (Seni et al., 1997; RRC, 2019). Seni et al. (1997) defined three plays within the Lower Miocene: (1) LM2 P.1B, which contains the "HC Sand", the highest producing sand in the field (~206 Bcf); (2) LM4 P.4, and (3) MM4 R.1. The documented porosities range from 31% to 33%, and permeabilities range from 50 to 2500 mD. The hydrocarbons have been trapped by rollover anticlinal structures and growth faults (Ruiz, 2019).

Multiple studies have been conducted to assess the suitability of the 24L depleted field for $CO_2$ storage. A detailed characterization by Ruiz (2019) was done to compare storage resource estimation methods in the HI 24L field. The first method involved direct volumetric conversion from the hydrocarbon production history, resulting in a total storage resource of 108 MtCO2 in the HC Sand alone (the shallowest sands of the LM1 sequence). The second method uses static volumetric capacity, as defined by equation (1.1) (Goodman et al., 2011), where the bulk volume is based on 3D geocellular modeling and closure analysis. The resulting static capacity ranges from 15 to 23 $MtCO_2$ in the HC Sands, and 179 $MtCO_2$ in LM2 sands. The third method of storage resource estimation used EASiTool, an analytical screening tool (later used in Chapter 4) developed by Hosseini et al. (2018), which considers pressure space and boundary conditions as key parameters to estimate storage resources and optimal injectivity for a given reservoir. Using this tool, the average capacity was found to be around 116 $MtCO_2$ for the LM2 interval and 30 $MtCO_2$ in the HC Sands (Ruiz, 2019). This thesis follows a similar use of these methods to provide a range of storage resource estimates and further discusses EASiTool for storage resource estimation in Chapter 4. The estimates referenced above are included in comparative analysis with the results of this research in Chapter 4 of this thesis.

***Clam Lake field***

The Clam Lake field is an onshore field spanning 1.09 square miles (~2.8 $km^2$). It is located in south Jefferson County, 13 miles west of Sabine and 3 miles inland from Texas State Waters (Figure 1.1). The Clam Lake field is a salt dome with complex crestal faulting, separating the producing reservoirs into isolated blocks that retain hydrocarbons. The productive Miocene and Upper Oligocene sands have yielded a cumulative of 7.28 MMbbl of oil and 6.05 Bcf of gas by 1961 (Denham, 1962).

This field has not been considered for CCS before. However, the equivalent $CO_2$ storage resource can be quickly estimated by converting gas-in-place to $CO_2$ mass using the conversion rate of 20 Mcf per ton of $CO_2$ (Meckel and Rhatigan, 2017). Based on this relationship, the equivalent $CO_2$ storage resource is estimated to be 0.3 $MtCO_2$ for this field. The values estimated for this field are not included in the comparative analysis presented in Chapter 4 of this work.

### 1.4 PROJECT DESCRIPTION

This study examines the area with the highest storage resource potential according to regional studies (Wallace, 2013; Wallace et al., 2014; Treviño and Meckel, 2017; Bump et al., 2021; Bump and Hovorka, 2024). The area chosen was previously estimated to contain storage resource potential of 4.7 to 20 $Mt/mi^2$ (1.8 - 7.5 $Mt/km^2$) in southeast Jefferson County, Texas (Wallace et al., 2014). This work considers a 749.9 $km^2$ area in Southeast Texas for detailed geologic characterization and structural analysis of the Lower Miocene Series to (1) identify non-hydrocarbon storage prospects for CCS, (2) estimate their $CO_2$ storage resource with different pressure-based boundary condition scenarios, and (3) compare them to static regional and local storage resource estimates. The workflow of this research is summarized in Figure 1.14.

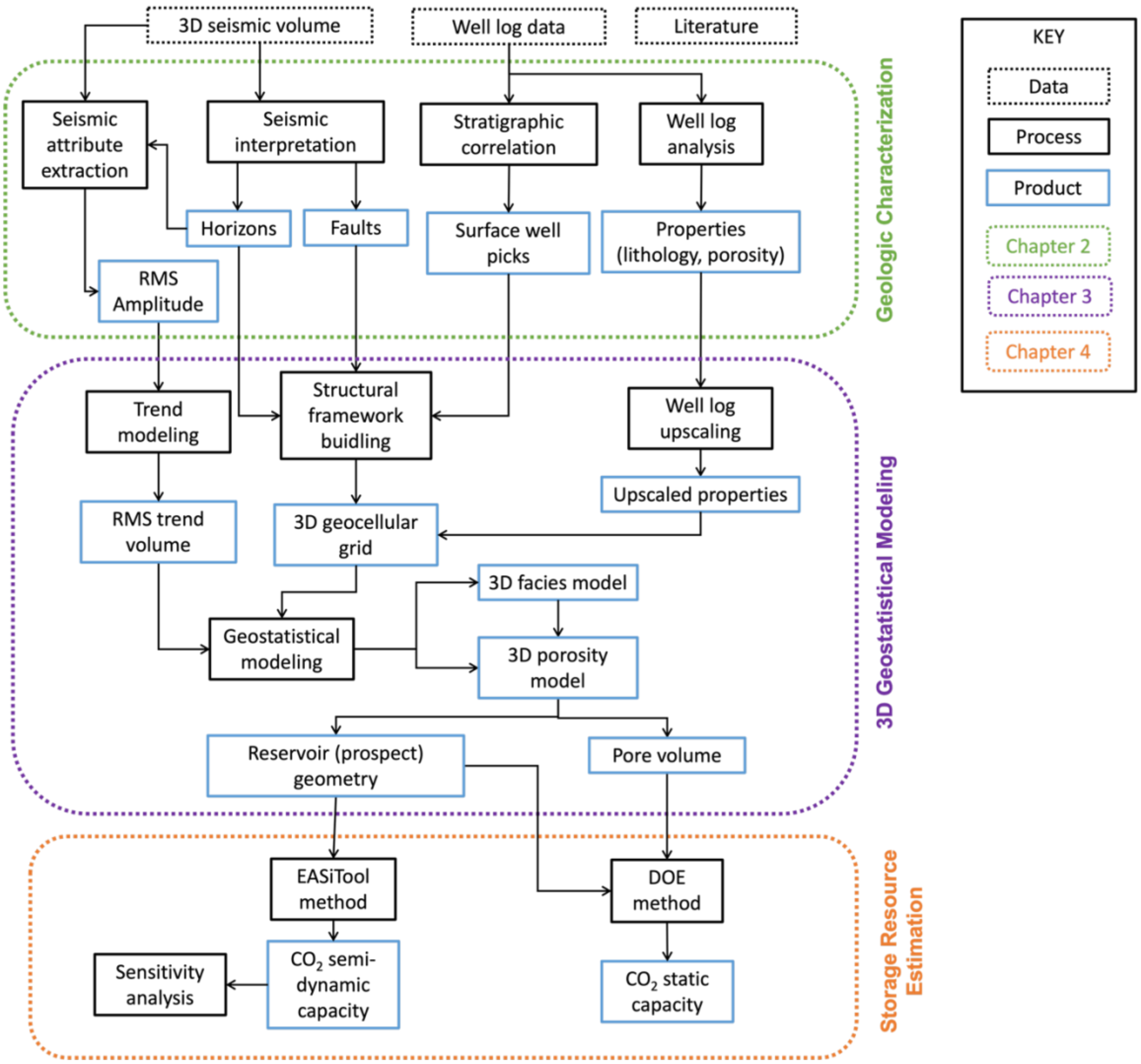


Figure 1.14: Schematic workflow diagram for this research.

## 1.5 SUMMARY

- Large-scale geologic carbon sequestration is needed to mitigate the environmental driver of atmospheric climate change
- The Northern Gulf of Mexico holds great potential for CCS due to its geologic setting, abundant data availability, and nearby $CO_2$ sources

- The Lower Miocene Series is an optimal interval for geologic carbon storage, explained by its structural and stratigraphic evolution
- Previous regional and field-scale studies for the Lower Miocene interval are reviewed, highlighting the methods used and estimated $CO_2$ capacities
- The objective of this research is to characterize a high-potential area in southeast Texas, identify a saline storage prospect, and estimate its storage resource using different calculation methodologies, which are then compared to previous assessments in the vicinity.

# Chapter 2: Geologic Characterization

Detailed geologic characterization is needed to identify CCS prospects and quantify their storage resources. This chapter describes the dataset, methodology, and results of the geologic characterization workflow performed in this thesis research. Seismic interpretation and well log correlation were performed using SLB's Petrel software (2023 version). Additional well log analysis was executed with code (Python) using Google Colab, with data stored in a Google Drive folder.

## 2.1 Site & Dataset Description

### 2.1.1 Seismic data

The seismic dataset used for this study is part of a seismic survey leased by Seismic Exchange, Inc. (2018) and used under license to the Bureau of Economic Geology (BEG). The TXLA Merge 3D seismic survey covers 3,100 $km^2$ (~1,013 $mi^2$) and is composed of 9 different smaller surveys (Figure 2.1). It contains 3,646 inlines (ranging from 5000-8645) and 2,193 crosslines (5000-7193) spaced at 100 ft (30.48 m). The dominant frequency of the seismic data in the area and interval of interest is around 25 Hz, and the average velocity at the depth of interest is ~2,500 m/s. The vertical resolution is about 25 m (82 ft) (Ramirez Garcia, 2019).

The Area of Interest (AOI) for prospect-scale evaluation is located in southeast Jefferson County, Texas, covering inlines 6600-7500 and crosslines 5147-6500 of the TXLA Merge survey (~750 $km^2$ area). The AOI was chosen to cover both onshore and offshore areas to map the progradation of a delta system and the associated facies changes across the shelf margin.

In this study, seismic interpretation is performed to map the structure of the Lower Miocene (LM2) interval and analyze the seismic response by extracting attributes. The interpretation is constrained by previous interpretations of bounding marine flooding surfaces, MFS9 and MFS10 (Sabbagh, 2017). Ultimately, the interpreted seismic horizons and faults are used as key inputs for building the structural framework, and seismic attributes will be used to guide the distribution trend in the property modeling phase of this study (see Chapter 3).

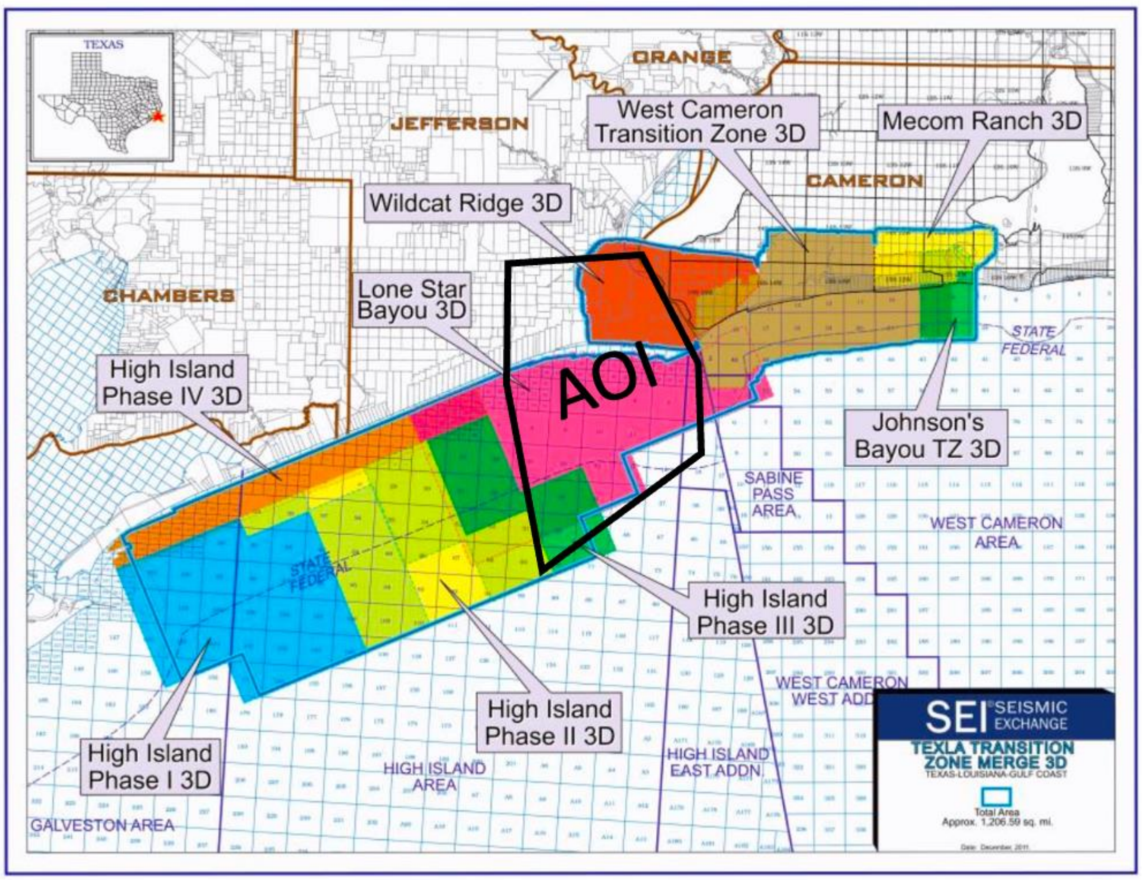


Figure 2.1: TexLa Transition Zone Merge 3D seismic survey, which is a combination of 9 different 3D surveys. The area of interest (AOI) is outlined in a black polygon (Seismic Exchange Inc., 2018; modified from Ruiz, 2019).

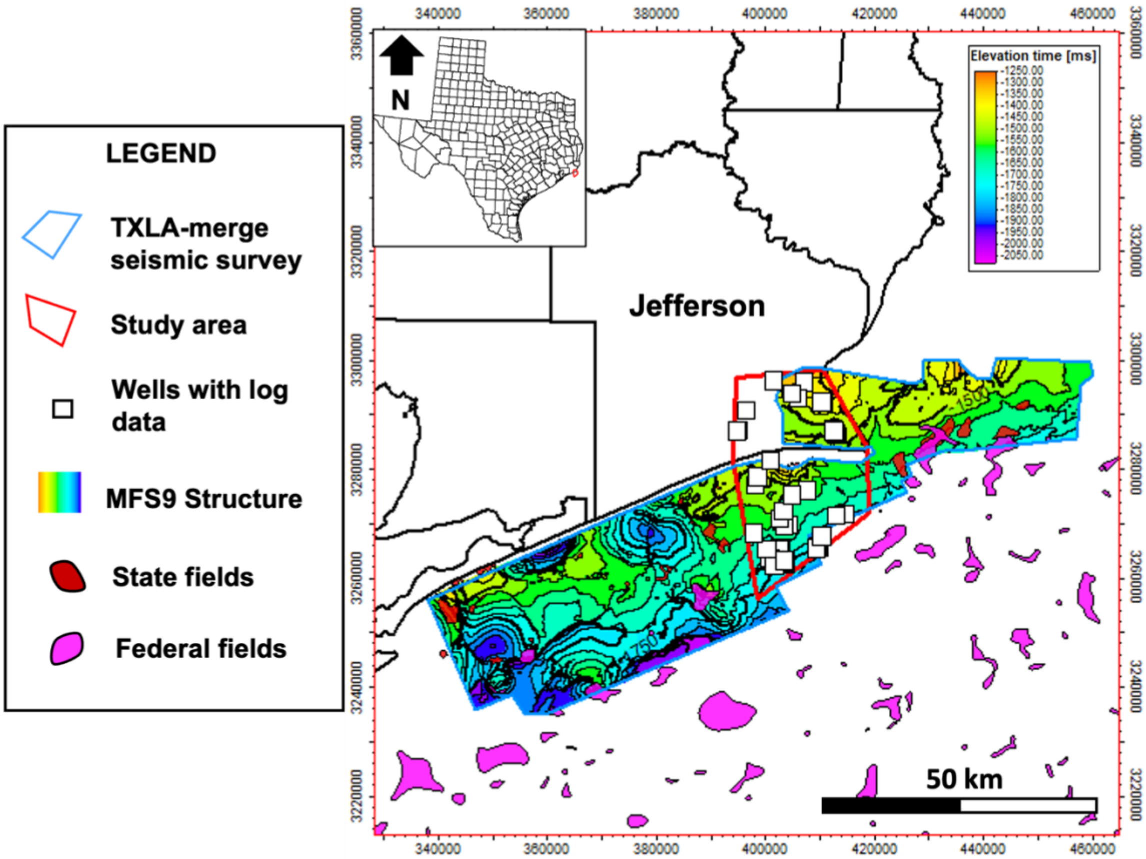


Figure 2.2: Map of study location and available data utilized in the AOI (red polygon). The structure mapped is the regional flooding surface (MFS9) mapped by Sabbagh (2017) across the TXLA Merge seismic survey.

### 2.1.2 Well log data

The AOI contains a total of 94 wells with wireline log data (Figure 2.2). The well location distribution can aid in constraining depths with the absence of seismic data in the northwestern quadrant of the AOI (Figure 2.2).

Table 2.1 summarizes the log data available for each well, with wells identified by their Unique Well ID (UWI) and arranged in descending order based on the number of available curves. Spontaneous potential (SP) and gamma ray (GR) logs are utilized for stratigraphic correlation and lithology analysis. In the AOI, 87 wells have SP logs, while only 28 have GR logs. Consequently, SP logs are primarily used for stratigraphic correlation and lithofacies assignment. GR logs serve as a secondary option when SP logs are unavailable, but other relevant logs are present. For property analysis, 13 wells have neutron-porosity (NPHI) logs, and 10 wells have density-porosity (DPHI) logs. Only six of these contain both logs, and just one includes data within the depth interval of interest. The properties calculated at well locations will be upscaled and then integrated into the 3D structural grid discussed in Chapter 3.

Table 2.1: Summary of well log inventory for 95 wells in the study area. "1" means the curve exists, and "0" means the curve does not exist. This table shows only the top 6 and the bottom 5 wells in terms of the number of available curves. The full table is in Appendix A.

| **Index** | **Well ID** | **Facies** | | **Density** | **Sonic** | **Porosity** | | **Resistivity** | **TOTAL LOGS** |
|---|---|---|---|---|---|---|---|---|---|
| | | **SP** | **GR** | **RHOB** | **DT** | **NPHI** | **DPHI** | **ILD** | |
| 1 | 42708401950000 | 1 | 1 | 0 | 1 | 1 | 1 | 1 | **6** |
| 2 | 42708401590000 | 1 | 1 | 1 | 1 | 1 | 0 | 1 | **6** |
| 3 | 42708401350000 | 1 | 1 | 1 | 1 | 1 | 0 | 1 | **6** |
| 4 | 42708400920000 | 1 | 1 | 1 | 1 | 1 | 0 | 1 | **6** |
| 5 | 42708400920000 | 1 | 1 | 1 | 1 | 1 | 0 | 1 | **6** |
| 6 | 42708403090000 | 1 | 1 | 0 | 0 | 1 | 1 | 1 | **5** |
| ⋮ | | | | | | | | | |
| 91 | 42245320600100 | 1 | 0 | 0 | 0 | 0 | 0 | 0 | **1** |
| 92 | 42708303580000 | 1 | 0 | 0 | 0 | 0 | 0 | 0 | **1** |
| 93 | 42708403980000 | 0 | 0 | 0 | 0 | 0 | 0 | 0 | **0** |
| 94 | 42245328930000 | 0 | 0 | 0 | 0 | 0 | 0 | 0 | **0** |
| 95 | 42245328760000 | 0 | 0 | 0 | 0 | 0 | 0 | 0 | **0** |
| **TOTAL WELLS** | | **87** | **28** | **7** | **22** | **13** | **10** | **62** | **229** |

## 2.2 SEISMIC INTERPRETATION

Seismic interpretation was performed with Petrel (2023) with the objective of mapping the structure, faulting, and thickness changes within the SIOI—which lies between MFS9 and MFS10—as well as extracting seismic attributes (e.g., amplitude) to capture stratigraphic changes in seismic facies both laterally and vertically. Interpreted horizons and faults are key inputs for the structural framework of the 3D model in Chapter 3.

Previous seismic interpretations of MFS9 and MFS10 by Sabbagh (2017), which vertically bound the LM2 SIOI, were used to constrain the LM2 window in the seismic time domain. Sabbagh (2017) interpretations were regional, covering the entire TEXLA-Merge survey. As discussed in the previous chapter, the upper bound, MFS9, is a regional datum associated with the Amph. B shale; and the lower bound, MFS10, separates the LM1 and LM2 depositional episodes (Olariu et al., 2019; Snedden and Galloway, 2019).

The seismic interpretation of three arbitrary horizons along high-amplitude reflectors within the LM2 was initially performed in the two-way-time (TWT) domain at every 50th inline and crossline, then interpolated using 3D autotracking. The interpretation was made to conform with Sabbagh (2017) surfaces (Figure 2.3) but introduces previously unmapped horizons in the SIOI for more refined correlation. This process was iterative, as constant quality control (QC) had to be done with the interpreted horizons when using 3D autotracking. In the northwestern quadrant of the AOI, where seismic data is missing, the seismic interpretation was extrapolated and later modified to match well picks near the Clam Lake Field.

For seismic depth conversion, a velocity model previously generated by a BEG researcher for the TEXLA seismic survey was applied to convert the interpreted horizons and the corresponding seismic volume from the time domain to the depth domain. To quality-scheck the depth conversion, the MFS9 surface was validated with stratigraphic picks in well logs to confirm it falls within the Amph. B shale.

Fault interpretation was performed and refined after the depth conversion of the seismic dataset (Figure 2.3). In the AOI, 33 major faults were identified and interpreted from seismic data. Fault transmissivity and fault-seal integrity are major areas of uncertainty for CO2 storage. The effect of nearby faults on reservoir compartmentalization may create pressure barriers that could limit storage capacity and injection rates. Based on seismic data, the average fault displacement in the AOI ranges from 65 to 165 ft (~20-50 m), which is small relative to reservoir thickness (~1500 ft; 457 m). Therefore, sands likely remain juxtaposed across the faults. In this research, faults are tested as boundary conditions for pressure-based resource estimation in Chapter 4.

The interpreted structural maps of five surfaces within the LM2 storage interval of interest show a general dipping to the south across the paleo shelf margin, with salt diapirism influencing the depositional architecture during the Early Miocene (Figure. 2.4). Because seismic imaging around the salt domes is not well-processed and thhus limited, the depth ranges are less certain. However, well log picks near or on top of the salt diapirs allowed us to confidently estimate the depths of MFS9 at these locations. Based on the seismic thickness maps, the overall thickening to the south but thinning towards the salt diapir suggest that salt movement may have been active during the Miocene deposition but at a slower rate while sediment influx was overwhelmingly high (Figure 2.4). Across the faults, the LM2 downthrow blocks show no significant thickening, suggesting that most fault movement likely occurred post-Miocene.

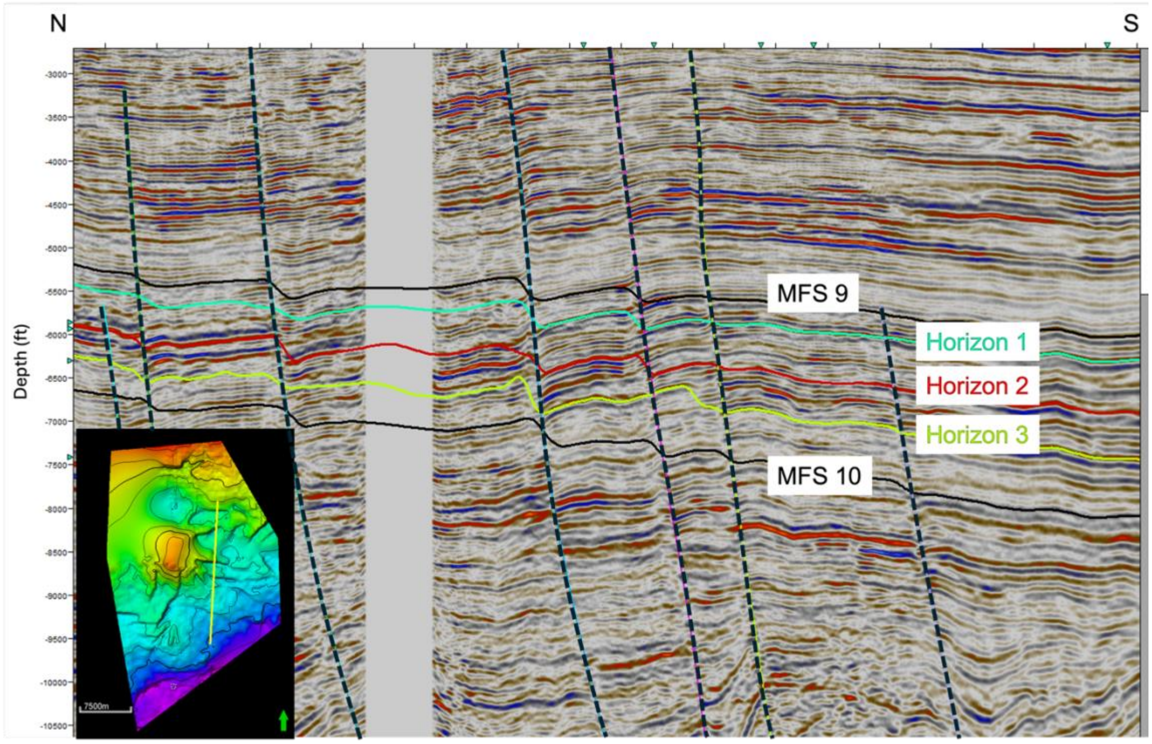


Figure 2.3: Seismic section showing key horizons and fault interpretations in this study. MFS 9 and MFS 10 surfaces in black are previous interpretations by Sabbagh (2017).

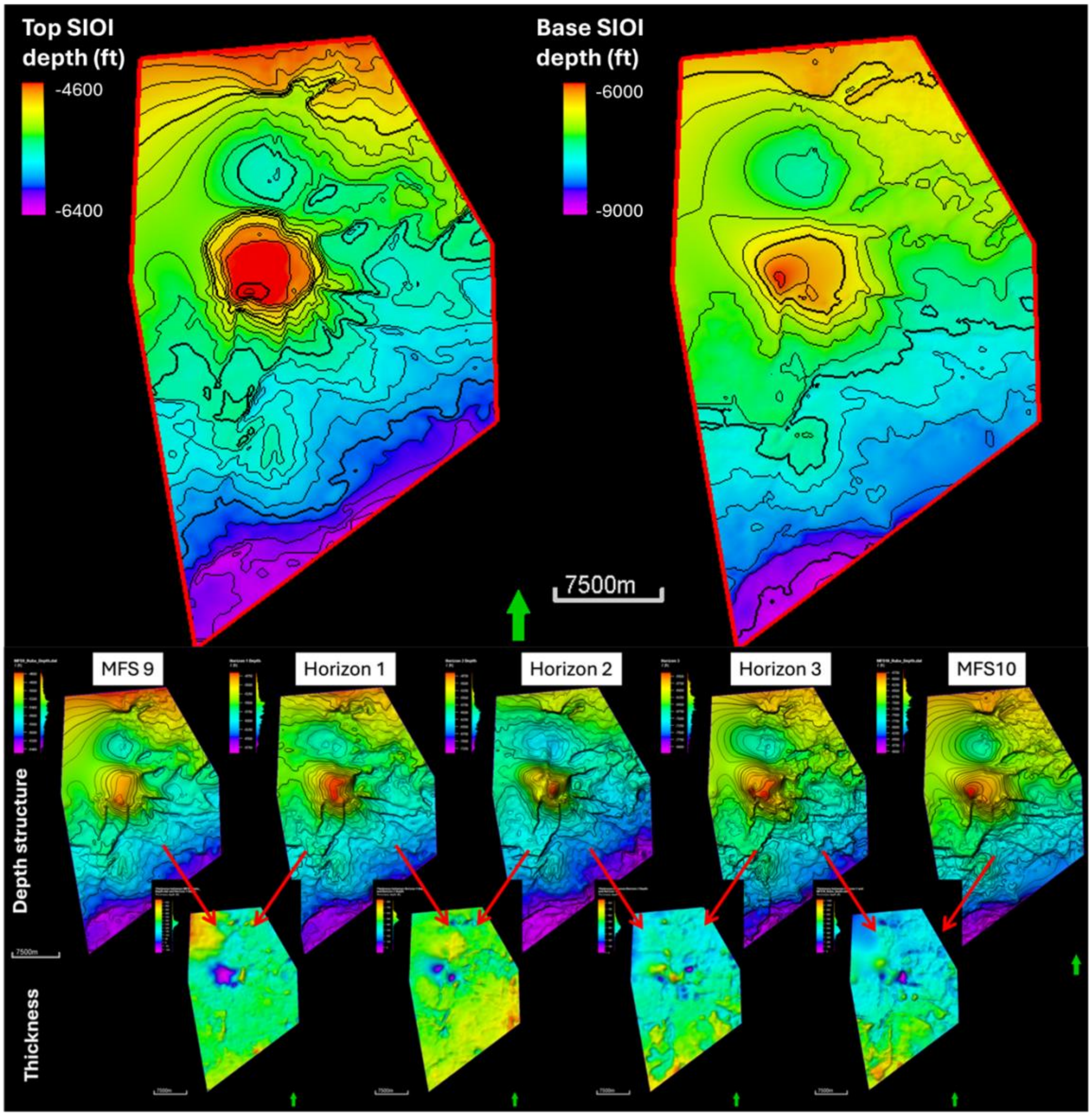


Figure 2.4: Top: seismic structure maps modified from Sabbagh (2017) of the top (MFS9) to the base (MFS10) of the storage interval of interest in feet. Bottom: computed thickness maps between the interpreted seismic surfaces.

### 2.3 Seismic Attribute Analysis

Seismic attributes are a vital characterization tool that aids in identifying geologic features, sand bodies, and structural discontinuities from seismic signals (DeAngelo et al., 2019). This tool will be used for prospect identification by delineating high-amplitude sands overlain by low-amplitude shales. More importantly, utilizing a 3D seismic volume can help infer the connectivity of sands between the wells in the study area. A common attribute used to identify sand-bodies is the Root Mean Square (RMS) Amplitude, which is the square root of the average of the squares of the amplitudes from each vertical sample within a given analysis window (DeAngelo et al., 2019; Oumarou et al., 2021). RMS amplitude essentially magnifies high-amplitude signals and diminishes low-amplitude signals, and it is used here to observe amplitude changes within the SIOI. Typically, high amplitudes (warm colors) reflect sandstone or other high porosity lithofacies, while lower amplitudes (cool colors) indicate a muddier facies (DeAngelo et al., 2019).

For this study, RMS amplitude was extracted from the depth-converted seismic cube to highlight geologic features and discontinuities from seismic signals (Figure 2.5). The resulting RMS amplitude volume will be used as a trend for the distribution of petrophysical properties between well locations in Chapter 3.

RMS amplitude was also extracted in 2D along interpreted horizons to observe spatial facies changes along five surfaces: MFS 9, Horizon 1, Horizon 2, Horizon 3, and MFS 10 (Figure 2.6). The analysis was applied in a zero-ft analysis window, which means the amplitude at the mapped horizon is shown, not including what is in a window that extends above and below. Unlike volumetric attributes, horizon attributes are only extracted along a single seismic horizon to highlight the lateral change in the seismic character across the area. This allows us to observe lateral facies change along a stratigraphic paleosurface (e.g., from deltaic sands to shales across the margin) and observe its temporal evolution by comparing it with the surface above it.

The resulting RMS surface maps show complex lateral sand distributions (high-amplitude patches), asserting the non-connectivity of sands within the massive Calcasieu delta lobe, which is larger than the study area (Figure 1.3; Figure 2.6). The vertical variability in RMS amplitude reflects temporal changes in sand distribution, with high-amplitude patches that are well connected on Horizon 2, and less so on Horizons 1 and 3. The sealing units, which are associate with low amplitudes, are patchy in the middle of the LM2 interval but more extensive on the marine transgression surfaces MFS9 and MFS10. The interpretation of surface attributes can be refined and optimized by interpreting additional horizons in between the five paleosurfaces to observe the evolution of the system margin at a finer time scale.

Additional attributes were extracted to refine the seismic interpretations presented in this chapter. Coherence attributes are commonly used to highlight discontinuities in the seismic signal that may represent faults or stratigraphic changes. Variance is a coherence attribute and a calculation of waveform dissimilarity within an analysis window. For this study, seismic variance was extracted from the cropped depth volume to quality-check fault interpretations (Figure 2.7).

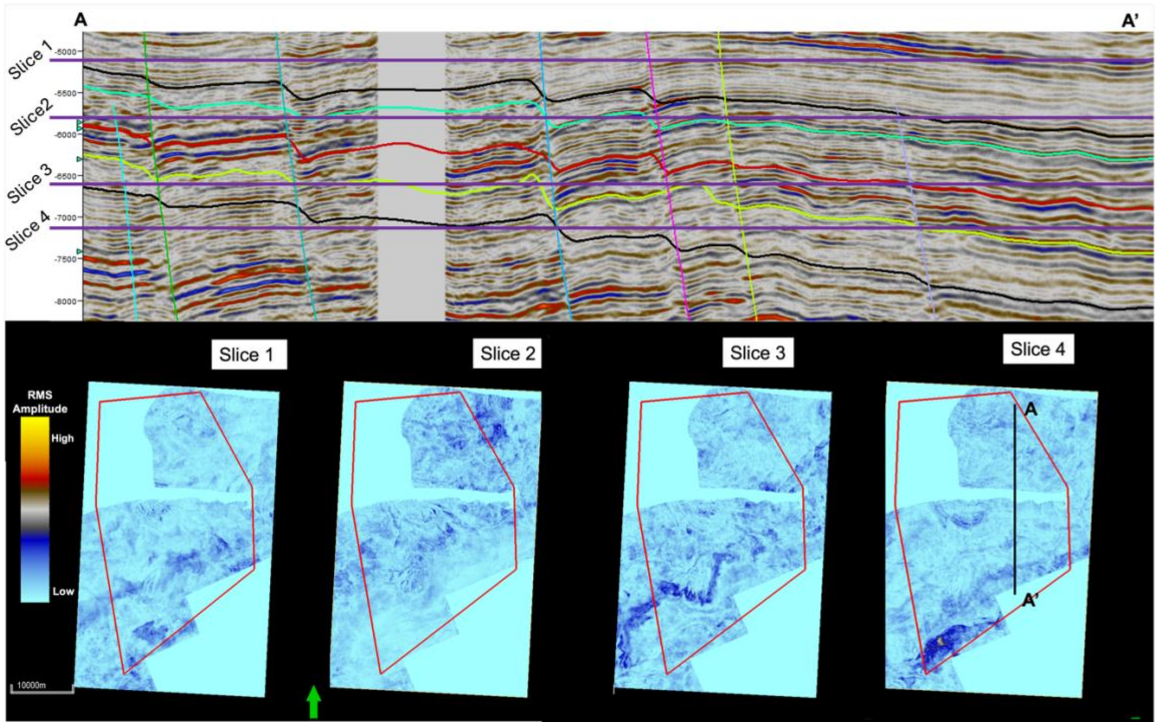


Figure 2.5: Seismic depth slices across the 3D RMS amplitude volume in the Lower Miocene 2 interval. The slices show dominance of low RMS amplitude (i.e., mud-prone facies) with a distingtive channel-like feature of relatively higher seismic amplitude striking SW-NE.

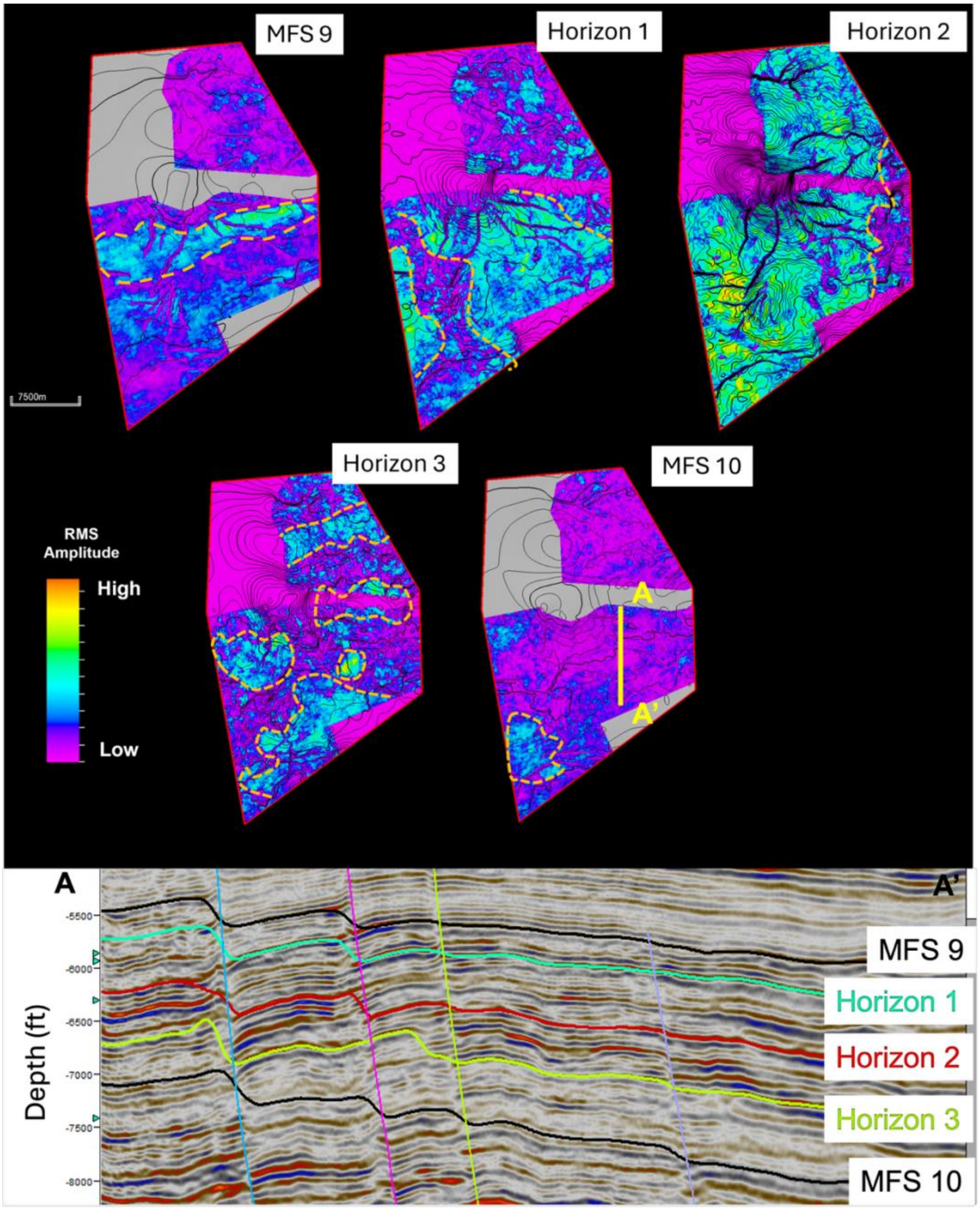


Figure 2.6: RMS amplitudes extracted from seismic horizon interpretations (stratigraphic paleosurfaces) of the storage interval of interest, with annotations of depositional features to distinguish high amplitudes (sand-prone) from low amplitudes (mud- prone). The top of the storage interval is MFS9, and the bottom is MFS10. Analysis window is 0 ft.

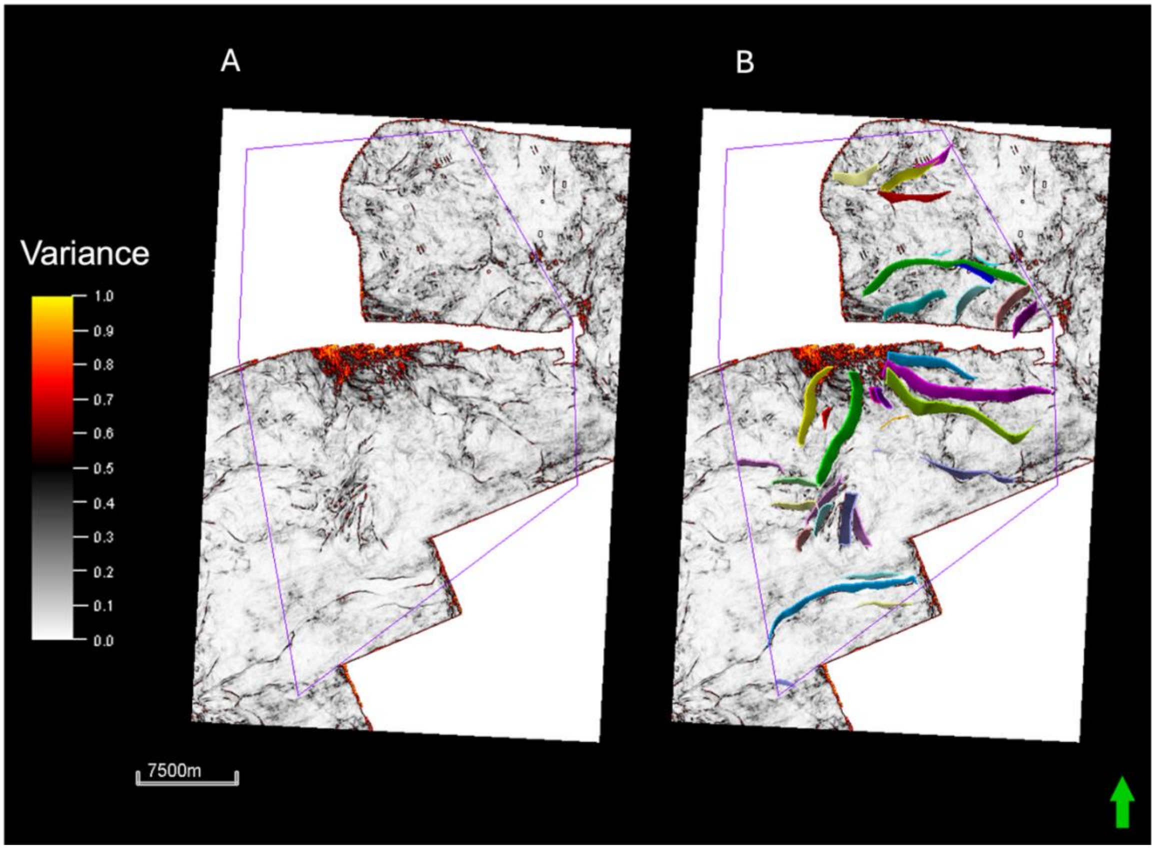


Figure 2.7: Seismic depth slice through 3D Variance volume (Z = 5600 ft) (A) without fault interpretations; (B) with fault interpretations.

## 2.4 Well Log Analysis

### 2.4.1 Stratigraphic correlation

For well log correlation, spontaneous potential (SP) curves were used to identify vertical stacking patterns within the interval of interest between MFS 9 and MFS 10. Previous well picks in the High Island 10-L Field by Ramirez Garcia (2019) were used to constrain the picking of the Amph. B shale and the underlying LM2 interval. Since SP curves are measured on a relative scale, they must be normalized to a common scale ranging from 0 (clean sand) to 1 (pure shale) for proper correlation. This normalization essentially provides us with the volumetric fraction of shale (VSH), using the equation: - 0pp

$$VSH_{SP} = \frac{SP - SP_{min}}{SP_{max} - SP_{min}} \tag{2.1}$$

where,

$VSH_{SP}$ = Shale volume from SP curve

SP = Log value from SP curve

$SP_{min}$ = Minimum SP value in the curve, representing clean sand

$SP_{max}$ = Maximum SP value in the curve, representing pure shale

A total of six surfaces were picked at 55 well locations using normalized SP (VSH) logs. The top and base picks for MFS 9 and MFS 10 were correlated across the AOI, following the aforementioned 10-L type log (Figure 2.8). Between them, three surfaces are interpreted as separating the main sequences, consisting of progradational, aggradational, and retrogradational stacking patterns (Figure 2.8). On a finer scale, the individual sandstone packages proved challenging to correlate across the entire AOI, proving the complexity of the stratigraphy and confirming that the sandbodies are indeed not connected throughout the AOI. Additionally, some faults cut the wells and are identified by missing stratigraphic sections in log record, with average throws of ~50 ft. It is worth noting that the MFS 10 surface picks at well locations may be off by a cycle or two based on the seismic surface and how it ties to the well logs.

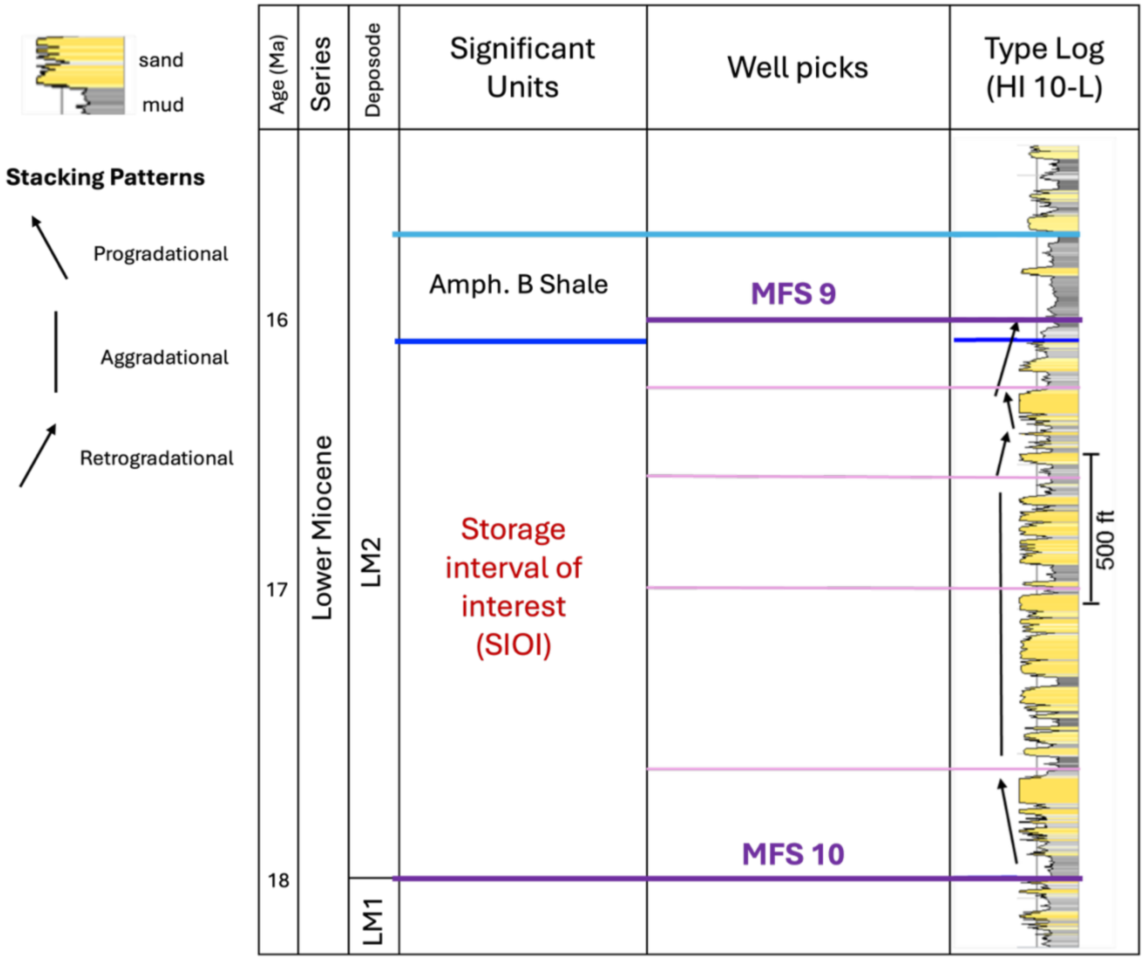


Figure 2.8: Spontaneous Potential (SP) type log from the High Island 10-L Field (Ramirez Garcia, 2019), showing stacking patterns of the units in the interval of interest and the key surface well picks that are interpreted in this study. Light blue=top of Amph. B shale; Purple=maximum flooding surface well picks (tied to seismic surfaces); Pink=well picks separating major stratigraphic cycles based on the stacking patterns.

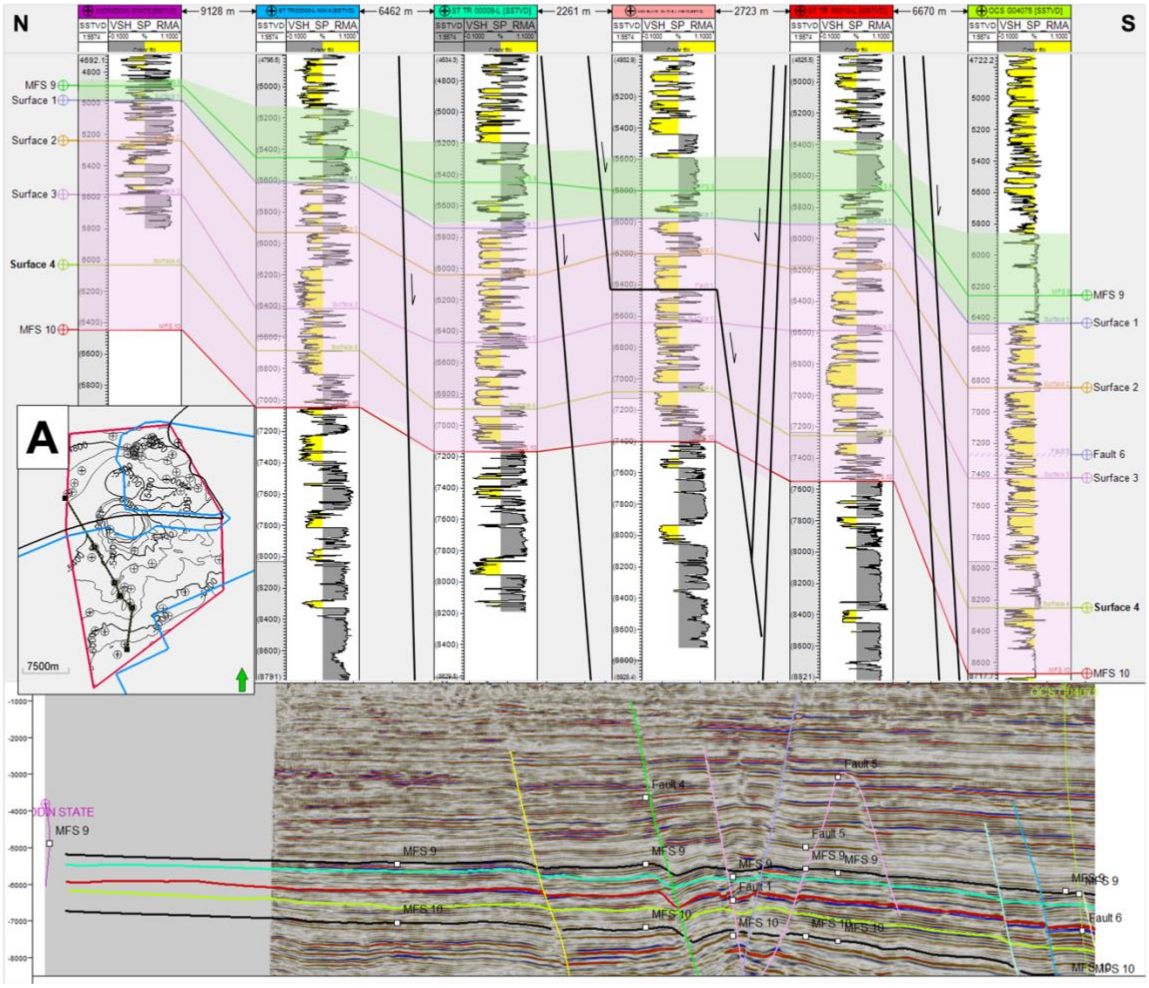


Figure 2.9: (A) Western dip-oriented well sections showing well log correlations (top) and alignment with seismic (bottom). The green interval represents the Amph. B shale, and the pink interval is the LM2 SIOI.

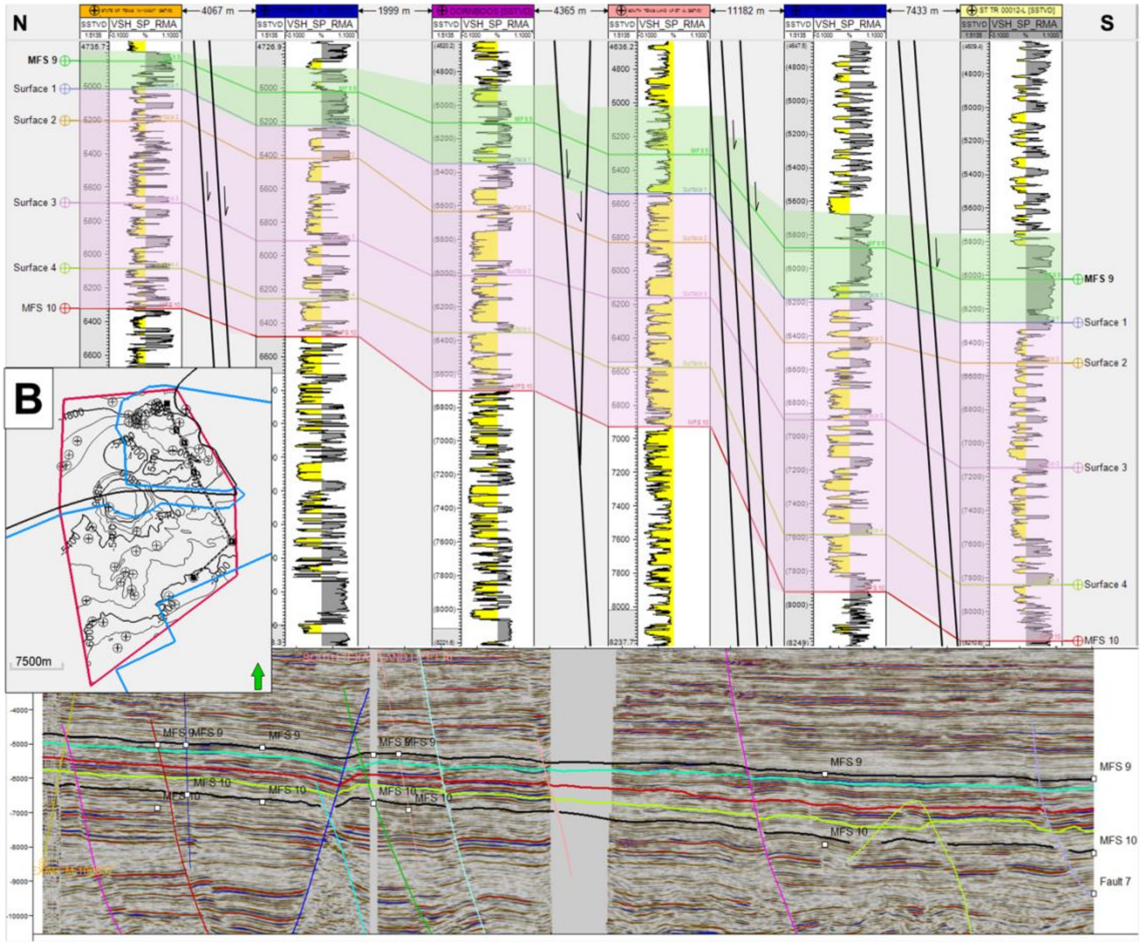


Figure 2.9: (B) Eastern dip-oriented well sections showing well log correlations (top) and alignment with seismic (bottom). The green interval represents the Amph. B shale, and the pink interval is the LM2 SIOI.

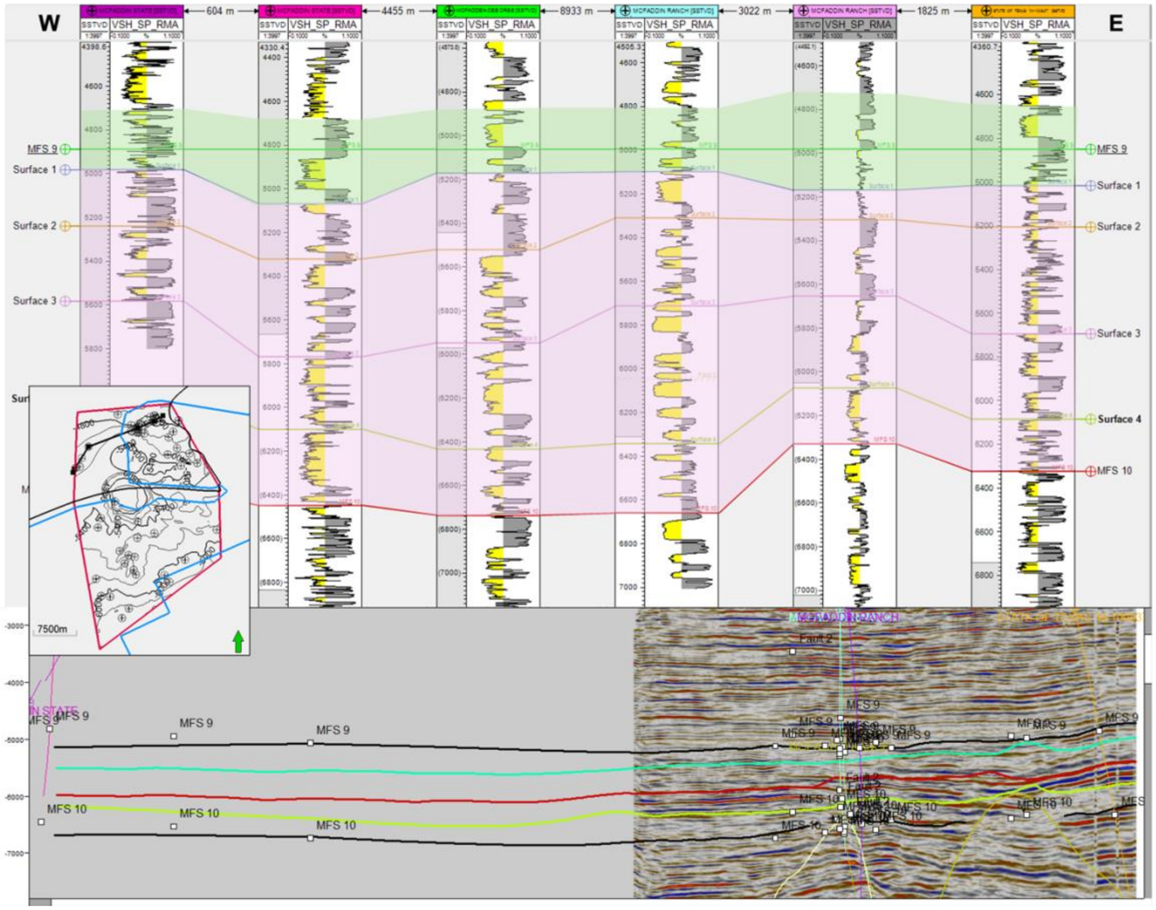


Figure 2.10: Strike-oriented section showing well log correlation (top) and seismic alignment (bottom) in the northern part of the AOI. The well section is flattened on MFS9. Note the area of missing seismic data in the northwest.

### 2.4.2 Lithofacies assignment

To distinguish sandstones from shales in the log record, the volumetric fraction of shale (Vshale or VSH), a continuous variable derived from SP using equation (2.1), is converted to a discrete log that categorizes lithotypes using chosen cutoffs. To determine cutoffs for this dataset, the distribution of VSH values from 60 wells with SP logs (Figure 2.11a) was analyzed to distinguish clean sandstone (VSH ~ 0%) from shale (VSH ~100%). In wells where the SP curve is unavailable, the same normalization equation (2.1) was applied to estimate VSH from gamma ray (GR) logs in 28 wells (Figure 2.11b). Prior studies in the area have always relied on SP as it is more common and the data is well-behaved. Thus, the decision was made to use solely SP logs for facies assignment for consistency. Based on the distribution of VSH derived from SP (Figure 2.11a), the lithotypes were classified based on the following:

- VSH < 0.4 is classified as "Clean Sand" (lithotype "0")
- 0.4 < VSH < 0.66 is classified as "Silty Sand" (lithotype "1")
- VSH > 0.66 is classified as "Shale" (lithotype "2")

The above conditions were applied to generate a new discrete "lithofacies" log that classifies the rock type along the wellbore wherever an SP curve is available. These newly created logs will be upscaled to a 3D grid to model facies distribution in Chapter 3.

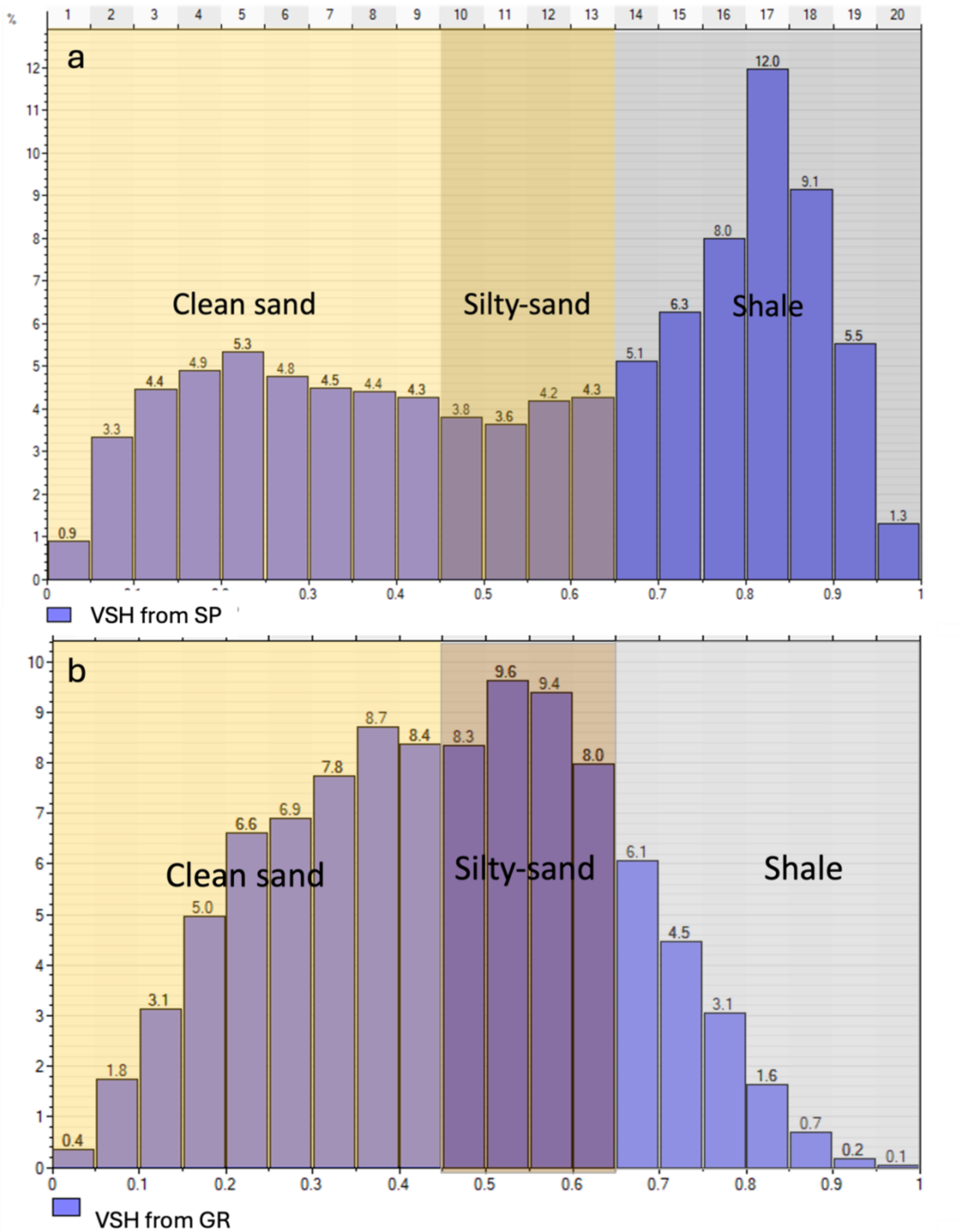


Figure 2.11: Histogram showing distribution of VSH values derived from (a) SP curves for 60 wells, and (b) GR curves for 28 wells in the AOI using equation (2.1), with lithotype cutoffs estimated based on the distribution.

### 2.4.3 Porosity calculation

Physical rock properties such as porosity and permeability can be inferred from petrophysical well logs. For simplicity in this study, the pores are assumed to be filled with brine (no hydrocarbons). Moreover, for static modeling, permeability is not included, as dynamic flow models are out of scope for this thesis. Rather, porosity curves were calculated and then validated with nearby porosity measurements from outside of the study area, and the results are later upscaled and populated across the 3D geocellular model in Chapter 3.

Porosity is a key factor for volumetric calculation of fluid capacities at a given site. However, core measurements are rare and sparse. In such cases, indirect porosity logs (NPHI and DPHI, or $\phi_n$ and $\phi_d$) are used to estimate the total porosity (PHIT, or $\phi_t$), which represents the fraction of pore space available regardless of pore connectivity that contributes to fluid flow. As discussed in the previous section, there is only one well that can be used to calculate total porosity, using the transform (Alberty, 1992):

$$PHIT = \sqrt{\frac{DPHI^2 + NPHI^2}{2}} \tag{2.2}$$

where,

PHIT = Total porosity

DPHI = Density-porosity log measurement

NPHI = Neutron-porosity measurement

For storage purposes, however, this research is more concerned with the effective porosity (PHIE or $\phi_e$) of the reservoir, which refers to the fraction of the total pore space that is likely connected (sandstone). In this case, the volumetric fraction of shale (VSH) is incorporated to essentially estimate the pore space available in sands only (Kamel and Mabrouk, 2003):

$$PHIE = PHIT \times (1 - VSH) \tag{2.3}$$

where,

PHIE = Effective porosity

PHIT = Total porosity

VSH = Volume of shale, derived from SP logs

The result is a continuous porosity curve, the distribution of which is illustrated in Figure 2.12. Based on the data distribution, certain porosity ranges are assigned to their corresponding lithofacies code. The overall porosity range can be validated using existing Lower Miocene porosity measurements from wells outside the study area, obtained from the BEG database (Figure 2.13). Based on the data in Figure 2.13, the average porosity for Lower Miocene stratigraphy is 24.9%, with a standard deviation of 3.6% (Loucks and Dutton, 2023). These values will be used to constrain the porosity model in Chapter 3, and later as inputs for $CO_2$ storage resource estimations in Chapter 4.

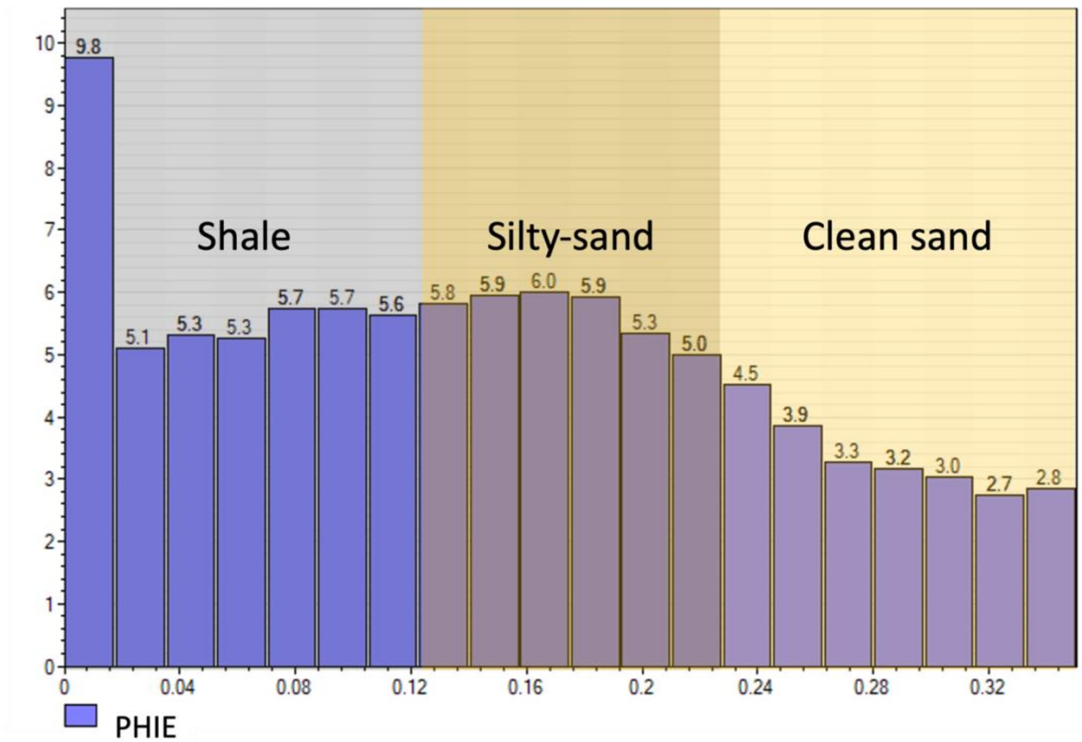


Figure 2.12: Histogram showing distribution of effective porosity (PHIE) calculated for one well in the south of the AOI (UWI 42708403090000) using equation (2.3), with annotations of estimated cutoffs in relation to lithotypes.

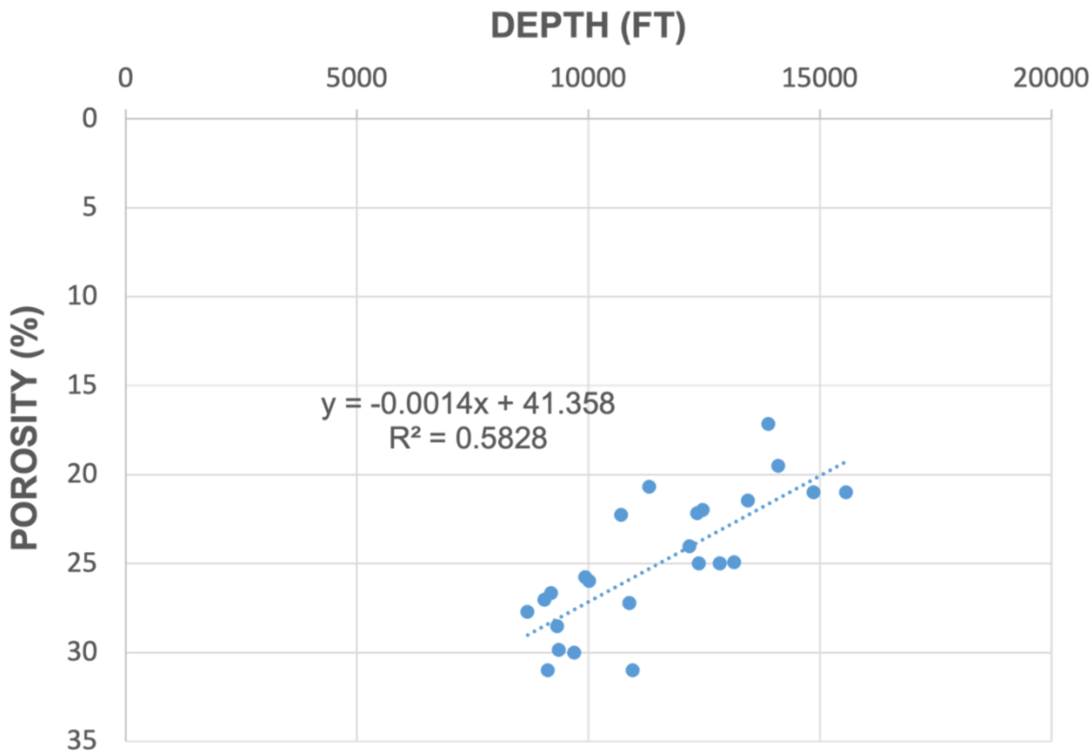


Figure 2.13: Lower Miocene porosity data as a function of depth based on a collection of petrophysical measurements from wells mostly outside the AOI. Note that the measurements are taken from wells in Federal Waters (i.e., deeper setting), where Lower Miocene Series lies in depths ranging from 8,600 to 15,000 ft (Loucks and Dutton, 2023).

### 2.5 Summary

- This chapter covers the workflow of geologic characterization for carbon storage site assessment in southeast Texas
- 3D seismic dataset and well logs were utilized to map subsurface structures, seismic facies, and reservoir properties
- Previous studies were used for reference to map the structure and thickness of the Lower Miocene 2 (LM2) storage interval

- Seismic attributes like RMS amplitude were extracted to highlight sand trends, shales, and faults, allowing us to identify favorable areas for potential storage
- Well log analysis allowed for correlation, rock classification (sand, silty-sand, or shale), and effective porosity calculation using SP and GR logs
- The results feed directly into building a 3D geocellular model and storage resource estimation in later chapters.

# Chapter 3: 3D Geocellular Modeling

This chapter covers the geocellular modeling workflow and results. The workflow consists of building a structural framework, 3D gridding, upscaling well logs to the grid, and populating rock properties across the grid cells using simple statistical methods with distribution trends guided by a seismic attribute volume. The final section covers post-processing and sensitivity analysis for $CO_2$ storage resource calculation in the following chapter. Table 3.1 summarizes the data utilized for 3D static modeling in this research.

Table 3.1: Summary of data available for geologic modeling

| Data | Number of data available | Source |
|---|---|---|
| Horizons | 5 | Sabbagh (2017) MFS surfaces + seismic interpretation (three arbitrary horizons in between) |
| Faults | 33 | Seismic interpretation (this study) |
| Seismic Attributes | 1 | Seismic attribute extraction (RMS amplitude volume) |
| Wells | 57 | BEG Database |
| Surface Picks | 2 | Well log interpretation (MFS 9 and MFS 10) |
| Lithofacies Curve | 57 | Derived from SP curves |
| Porosity Curve | 1 | Derived from neutron- and density-porosity curves |

### 3.1 Structural Framework Building

The structural framework is built by integrating seismic surfaces, faults, and well surface picks to generate a 3D model that allows for volumetric calculations. For this study, there are five seismic horizons, two of which are tied to well surface picks, and 33 faults that go into building the structural framework (Figure 3.1).

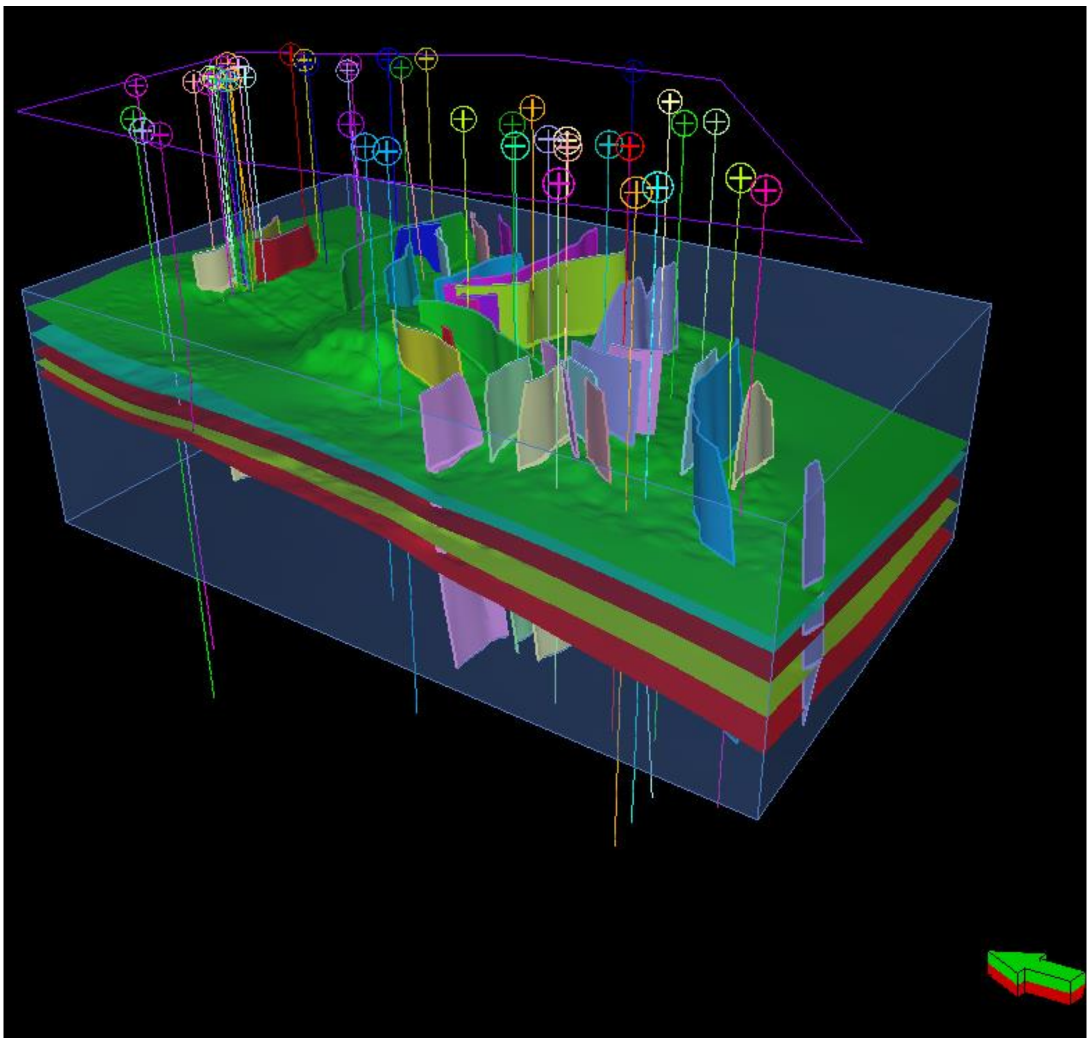

Figure 3.1: 3D representation of the structural framework showing seismic surfaces, faults, and well locations.

## 3.2 GRID DEFINITION

To build the 3D model, a 3D grid is defined to contain cells that will be populated with rock properties derived from petrophysical logs. The structural framework defined in the previous section is the foundation for the structural grid. Table 3.2 summarizes the 3D grid parameters used for modeling. The five seismic horizons create four zones that are each assigned a number of layers in the grid based on the resolution of the log response. The layering was chosen to be proportional to their respective top and bottom surfaces to best honor the geology (Figure 3.2).

Table 3.2: Summary of relevant geocellular grid information used for modeling. Surfaces with "*" are tied to well picks.

| **Structural Grid Statistics** | | | |
|---|---|---|---|
| | **x** | **y** | **z** |
| Grid increment (m) | 50 | 50 | 16.3 |
| Number of grid cells | 500 | 835 | 118 |
| Total number of cells | 49,265,000 | | |
| **Number of Layers** | | | |
| Zone 1 (MFS 9* - Horizon 1) | 20 | | |
| Zone 2 (Horizon 1 - Horizon 2) | 30 | | |
| Zone 3 (Horizon 2 - Horizon 3) | 30 | | |
| Zone 4 (Horizon 3 - MFS 10*) | 30 | | |
| TOTAL | 110 | | |

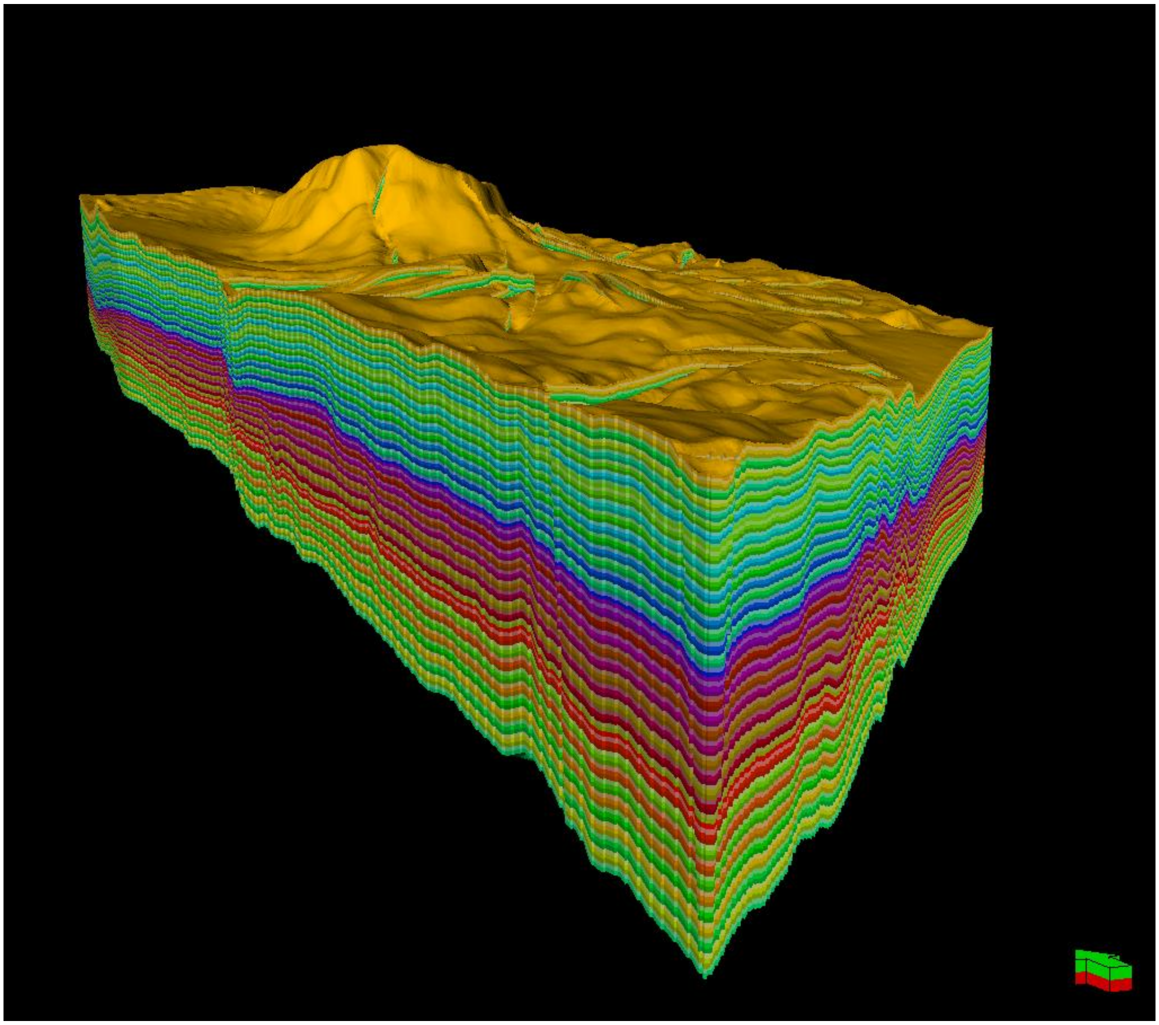

Figure 3.2: 3D structural grid showing 110 layers considered for property modeling. Average cell size is 50 x 50 x 16.3 m

### 3.3 Geostatistical Property Modeling

In this section, petrophysical rock properties derived from well logs will be incorporated into the 3D grid and later populated across the grid with a trend volume to guide it. Two types of properties will be defined at well locations: the discrete lithotype curve, and the continuous effective porosity curve. In the area of study, there are 57 wells with lithology logs and one well with an effective porosity log (Table 3.1). A seismic RMS amplitude volume, previously mentioned in Chapter 2, is used to guide the distribution of properties in such a way that honors the geology related to sand continuity.

To assign the grid cells property values at well locations, the well logs, which have a 2 ft sampling rate (~0.61 m), must first be upscaled to the grid's vertical resolution, which is approximately 53.5 ft (16.3 m). After upscaling the global lithofacies log, each cell crossing the well paths of 57 wells is assigned a facies value (sand, silty sand, or shale) (Figure 3.3a). The averaging method most appropriate for upscaling the discrete lithofacies logs is the "most of" function, which assigns the most frequently occurring lithofacies code within a 3D grid cell to that cell. The overall facies proportions assigned were approximately 46% for sand, 27% for silty-sand, and 26% for shale based on existing well log data. The upscaling of the porosity log (PHIE) considers the one well in the very south of the AOI (Figure 3.3b) and was done using arithmetic mean, as it is more appropriate for continuous logs (SLB, 2023).

For spatial control, especially in areas with no well data, the depth-converted RMS volume (25 ft vertical resolution) is incorporated and resampled to the 3D grid to guide the distribution of properties between wells (Figure 3.3c). The distribution of facies was performed using the Sequential Indicator Simulation (SIS) algorithm embedded in Petrel, along with the RMS volume for trend control (Figure 3.4). The distribution of effective porosity was conditioned to facies with normal distributions and assigned porosity ranges, where sand has an effective porosity range of 22-35%, 12-22% for silty sand, and 0-12% for shale (Figure 2.12) A total of ten realizations were made of the effective porosity model (Figure 3.5), and the results are summarized in Table 3.3.

Table 3.3: Summary of effective porosity model statistics for 10 model realizations.

| **Realization** | **Porosity (effective)** | | | |
|---|---|---|---|---|
| | **Min** | **Max** | **Mean** | **std** |
| 1 | 0 | 0.4492 | 0.1971 | 0.0989 |
| 2 | 0 | 0.4492 | 0.1965 | 0.0998 |
| 3 | 0 | 0.4492 | 0.1958 | 0.0976 |
| 4 | 0 | 0.4492 | 0.1972 | 0.0973 |
| 5 | 0 | 0.4492 | 0.1966 | 0.0975 |
| 6 | 0 | 0.4492 | 0.1969 | 0.0994 |
| 7 | 0 | 0.4492 | 0.1973 | 0.0978 |
| 8 | 0 | 0.4492 | 0.1971 | 0.0992 |
| 9 | 0 | 0.4492 | 0.1958 | 0.0961 |
| 10 | 0 | 0.4492 | 0.1967 | 0.0986 |
| **AVERAGE** | **0** | **0.4492** | **0.1967** | **0.09822** |

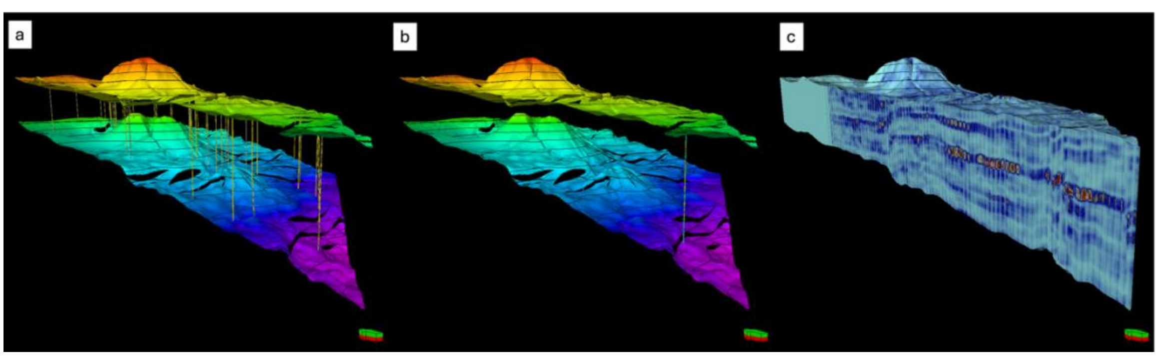


Figure 3.3: 3D views showing the properties that have been upscaled to the grid between MFS9 and MFS10. a) lithofacies in 57 wells, b) effective porosity in one well, and c) RMS amplitude volume (everywhere). Z factor = 10

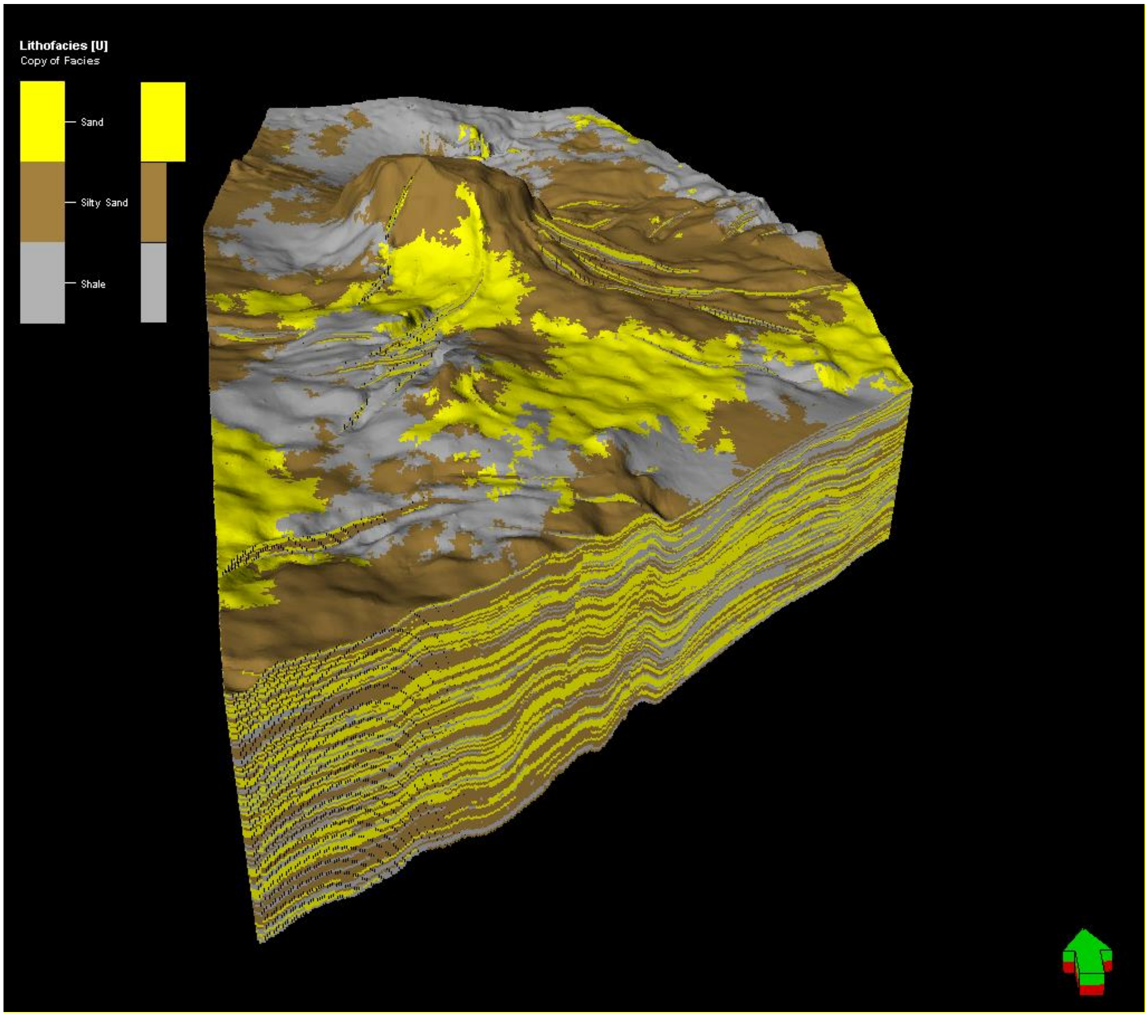


Figure 3.4: 3D representation of resulting 3D facies model derived from upscaled well logs facies determinations.

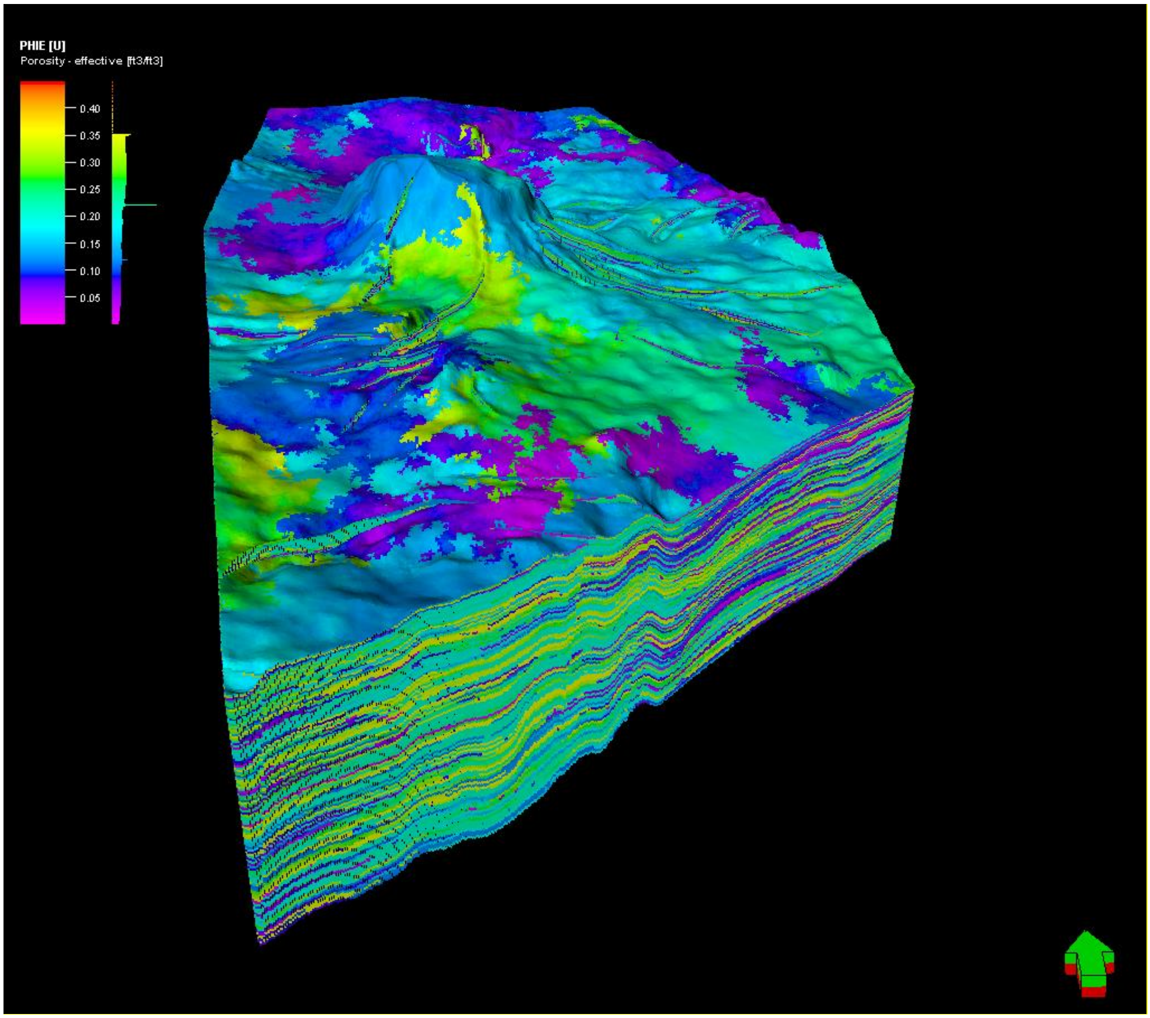


Figure 3.5: 3D representation of resulting effective porosity model (realization 1).

## 3.4 Post Processing

### 3.4.1 Prospect definition

Based on the structural analysis and static models, a small area (62 km$^2$; ~24 mi$^2$) southeast of the salt diapir has been identified as the "prospect" for $CO_2$ storage resource estimation in the next chapter (Figure 3.6). The prospect lies southeast of the salt diapir and sits between two faults that radiate from the salt structure. The strata show subtle thickening and southeastward dipping, away from the salt diapir. The gross thickness of the SIOI in the prospect area is approximately 1500 ft (~457 m), containing interbedded sand, silty sand, and shale facies.

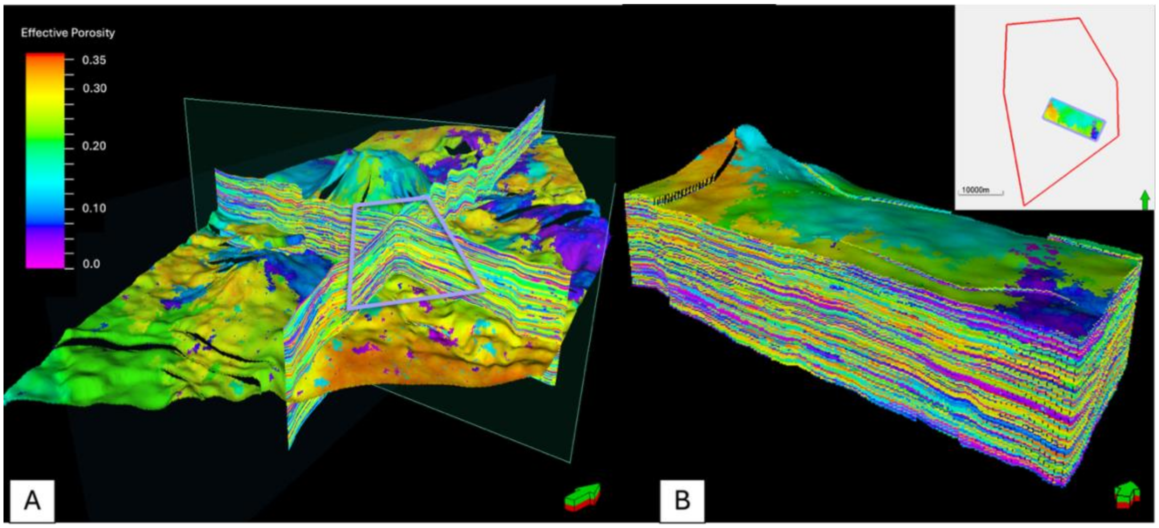


Figure 3.6: 3D representation of the prospect location, size and effective porosity distribution. (A) shows I, J, and K intersections around the prospect location, and (B) shows the cropped 3D grid to the prospect area.

### 3.4.2 Net pore volume and sensitivity analysis

In order to calculate the Net Pore Volume (NPV) available for $CO_2$ storage, a net sand thickness must be determined for each grid cell. Net thickness here refers to the total cumulative thickness of a rock layer that meets specific, usable criteria for holding and transmitting fluids. Net thickness is a subset of the gross thickness, calculated by applying a specific net-to-gross (NTG) ratio to each facies. The net pore volume, assigned for each grid cell, is calculated by:

$$NPV = A_t h_g NTG \phi_e \tag{3.1}$$

where,

$NPV$ = net pore volume (m$^3$)

$A_t$ = total area (m$^2$)

$h_g$ = gross thickness (m)

$NTG$ = net-to-gross ratio (unitless)

$\phi_e$ = effective porosity (unitless)

Three NTG models were applied to test the sensitivity of net pore volume, and ultimately the storage resource, to net thickness (Table 3.4). The first model assigned NTG values of 0, 0.5 and 1 for shale, silty sand, and sand facies respectively. This essentially means that when a cell is assigned sand facies, the net thickness will account for 100% of the gross thickness; for silty sand, the 50% of the thickness is considered; and 0% of the thickness is accounted for shale.

Table 3.4: Net-to-gross ratios tested for net pore volume calculation.

| **Facies** | **Optimistic NTG** | **Conservative NTG** | **Pessimistic NTG** |
| --- | --- | --- | --- |
| Sand | 1 | 1 | 1 |
| Silty sand | 0.5 | 0.15 | 0 |
| Shale | 0 | 0 | 0 |

Table 3.5: Prospect net pore volume calculated results for the three net-to-gross (NTG) ratio models and 10 effective porosity ($\phi_e$) realizations. The "optimistic" NTG model refers to 0.5 net-to gross ratio applied for silty sand, and the conservative NTG is 0.15.

| $\phi_e$ Realization | Optimistic NTG | Conservative NTG | Pessimistic NTG |
|---|---|---|---|
| | Net Pore Volume ($m^3$) | | |
| 1 | 6.15E+09 | 5.62E+09 | 5.38E+09 |
| 2 | 6.13E+09 | 5.61E+09 | 5.39E+09 |
| 3 | 6.07E+09 | 5.56E+09 | 5.34E+09 |
| 4 | 6.04E+09 | 5.50E+09 | 5.27E+09 |
| 5 | 6.12E+09 | 5.59E+09 | 5.37E+09 |
| 6 | 6.06E+09 | 5.54E+09 | 5.31E+09 |
| 7 | 6.05E+09 | 5.52E+09 | 5.30E+09 |
| 8 | 6.19E+09 | 5.66E+09 | 5.44E+09 |
| 9 | 6.04E+09 | 5.49E+09 | 5.26E+09 |
| 10 | 6.00E+09 | 5.46E+09 | 5.23E+09 |
| **AVERAGE** | **6.08E+09** | **5.55E+09** | **5.33E+09** |

As shown in Tables 3.4 and 3.5, the first NTG model is considered more optimistic by accounting for more transitional (silty sand) facies as "storable" intervals. A second and more conservative NTG ratio of 15% was applied to silty sand, which resulted in an 8.7% decrease in storable volume from $6.08 \times 10^9$ to $5.55 \times 10^9$ cubic meters for the prospect (Table 3.5). The third "pessimistic" model accounts only for sand facies and none of the silty sand intervals in the net thickness calculation, resulting in a 12% reduction in storable volume compared to the optimistic model. This insignificant decrease could be attributed to the way facies' thickness proportions were assigned during the model-building stage of this thesis.

### 3.5 SUMMARY

- A 3D structural framework was built using the seismic surfaces, faults, and well surface picks from Chapter 2
- The 3D grid was set up to divide the model into layered cells based on seismic surface and well log resolution
- Well log data were upscaled and used to assign lithofacies (sand, silty-sand, and shale) and effective porosity to grid cells, guided by seismic attributes for spatial trends
- A 62-$km^2$ prospect area was identified as the main $CO_2$ storage target, for which the storage resources are estimated in Chapter 4
- Net pore volume was calculated for each grid cell, using different net-to-gross (NTG) ratio models to test how assumptions affect storage estimates
- Reducing the silty-sand component in the NTG parameter led to a slight (~12%) reduction of the total net pore volume. This is likely due to the way in which facies proportions were assigned during the modeling phase of this work.

# Chapter 4: $CO_2$ Storage Resource Estimation

This chapter covers the quantification of $CO_2$ storage resources for the prospect defined in Chapter 3. Two methods are covered in this study: 1) The DOE-NETL static volumetric method, which was introduced in Chapter 1 (Goodman et al., 2011); and 2) pressure-based semi-dynamic analytical method using EASiTool, also previously defined in Section 1.3 of this thesis. The final section summarizes and compares the results from the two methods.

## 4.1 Static Storage Resource Estimation

The US DOE-NETL equation (1.1) is a calculation of storable $CO_2$ mass in a fraction of the pore volume, which is a product of the reservoir area, gross formation thickness and total porosity (Goodman et al., 2011). In the previous chapter, three models of variable NTG ratios were tested to note the impact on net pore volume, for which there are 10 realizations that were calculated using equation (3.1). For this section, the volumetric values calculated in Table 3.5 are considered "storable" within the prospect area (62 km$^2$; ~24 mi$^2$) for static resource calculation. Thus, the Goodman et al. (2011) equation is refined to reflect these parameters:

$$M_{CO2} = NPV\rho_{CO2}E_{saline} \tag{4.1}$$

where,

$M_{CO2}$ = $CO_2$ storage resource mass estimate (kg; where 1 metric ton (tonne) = 1000 kg, and 1 Mt = $10^6$ metric tons)

$NPV$ = net pore volume (m$^3$)

$\phi_e$ = effective porosity (unitless)

$\rho_{CO2}$ = $CO_2$ density at reservoir conditions (kg/m$^3$)

$E_{saline}$ = storage efficiency factor for saline aquifers (unitless)

The storage efficiency factor ($E_{saline}$) is one of the most influential and debated parameters in $CO_2$ storage resource assessments. It represents a fraction of the pore volume that can realistically be occupied by injected $CO_2$ (Goodman et al., 2011; Bachu, 2015; Goodman et al., 2016). It is acknowledged that the Goodman et al. deterministic method provides a wide range of storage resource estimates that are most likely highly inflated due to $E_{saline}$, which realistically can be closer to 1% based on prior reservoir simulations (Treviño and Meckel, 2017). For this study, a range of storage probabilistic storage efficiency factors ranging from 1% (P90) to 50% (P10) were tested to quantify the capacity's sensitivity to this variable, a portion of which is presented in Table 4. 1.

A range of $CO_2$ densities (620 - 750 kg/m$^3$) were also tested to quantify their impact on $CO_2$ storage resource estimates. Previously compiled temperature and pressure data from wells penetrating Miocene strata in Texas State Waters were used by Nicholson (2012) and Wallace (2013) to determine the regional $CO_2$ density using the Peng-Robinson equation of state (Figure 4.1). Given the substantial thickness considered here for storage resource estimation (~1500 ft; 475 m), a range of $CO_2$ densities reflecting the depth-dependent variability in reservoir conditions (i.e., temperature and pressure) had to be considered. For the SIOI in this study, temperature ranges from 60 °C to 75 °C, and formation pressure ranges from 20 to 25 MPa (Figure 4.1; Nicholson, 2012; Wallace, 2013). Portions of the estimated static capacities are summarized in Table 4.1 and plotted in Figure 4.2. More capacity datapoints exist in a file that test combinations of NTG models, efficiency factors and $CO_2$ densities, that could not be included in this thesis format due to its large size (see Appendix B). The full table of static $CO_2$ capacity calculations is located in an Excel spreadsheet titled “static_capacity_calc.xlsx”, available to BEG/GCCC researchers.

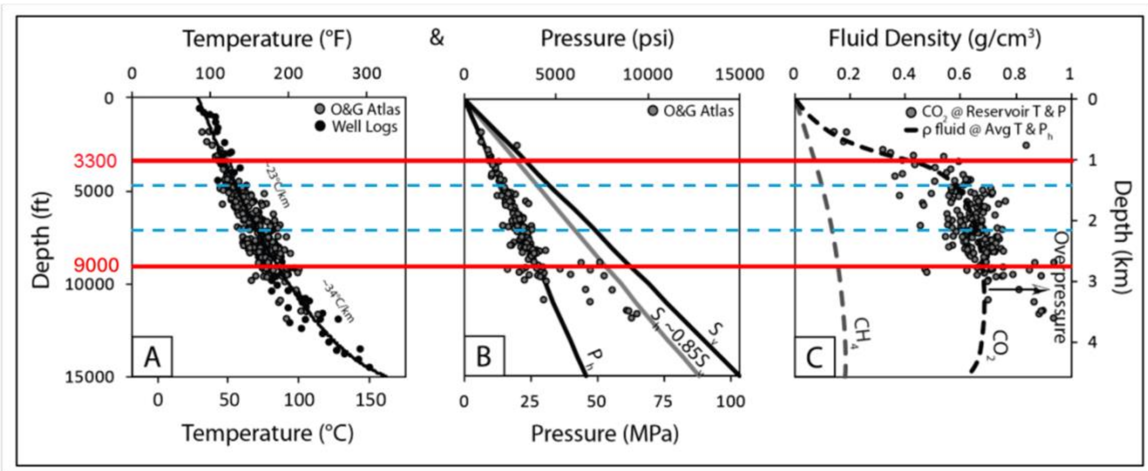


Figure 4.1: (A) Temperature, (B) pressure, and (C) $CO_2$ density versus depth in Texas State Waters, modified from Nicholson (2012) and Wallace (2013). Red lines mark the approximate top (supercritical depth) and base (formation overpressure) of the $CO_2$ storage window. Blue dashed lines indicate the approximate depth of the storage interval of interest for this study (Lower Miocene 2 SIOI).

Table 4.1: Portion of probabilistic $CO_2$ storage resource estimates of variable storage efficiencies covering the prospect area and SIOI for one scenario, where the pessimistic NTG (P90) model was used, and $CO_2$ density was assumed to be 650 kg/m$^3$ (P50).

| **Facies model** | **Porosity model realization** | **NTG model** | **$CO_2$ (km/m$^3$)** | **NPV $\times 10^9$ (m$^3$)** | **Static $CO_2$ Storage Resource (Mt)** | | |
|---|---|---|---|---|---|---|---|
| | | | | | **E = 1% (P90)** | **E = 14% (P50)** | **E = 50% (P10)** |
| 1 | 1 | pessimistic (P90) | 650 (P50) | 5.38 | 34.97 | 489.58 | 1748.50 |
| | 2 | | | 5.39 | 35.04 | 490.49 | 1751.75 |
| | 3 | | | 5.34 | 34.71 | 485.94 | 1735.50 |
| | 4 | | | 5.27 | 34.26 | 479.57 | 1712.75 |
| | 5 | | | 5.37 | 34.91 | 488.67 | 1745.25 |
| | 6 | | | 5.31 | 34.52 | 483.21 | 1725.75 |
| | 7 | | | 5.30 | 34.45 | 482.30 | 1722.50 |
| | 8 | | | 5.44 | 35.36 | 495.04 | 1768.00 |
| | 9 | | | 5.26 | 34.19 | 478.66 | 1709.50 |
| | 10 | | | 5.23 | 34.00 | 475.93 | 1699.75 |
| **AVERAGE** | | | | **5.33** | **34.64** | **484.94** | **1731.93** |

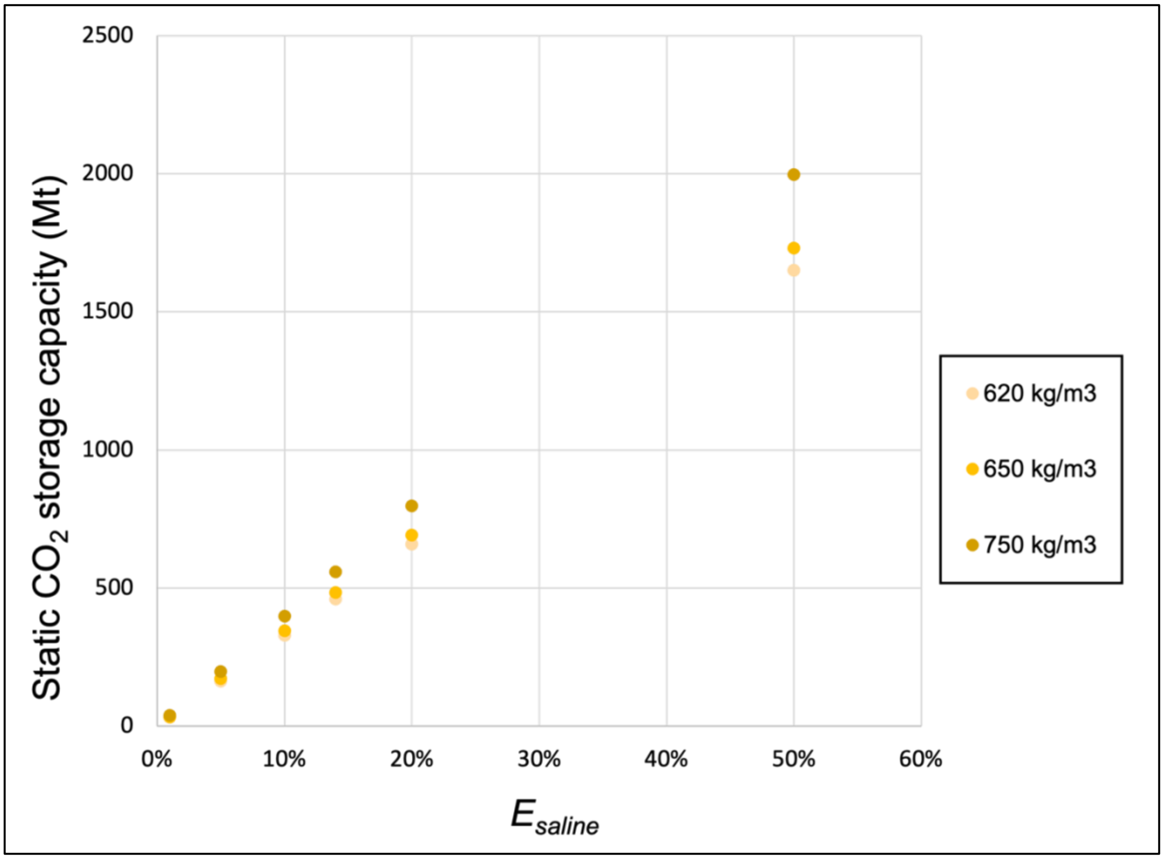


Figure 4.2: Plot summarizing static $CO_2$ storage resources for the prospect, estimated using the Goodman et al. (2011) method as a function of the storage efficiency factor $E_{saline}$, and color-coded by $CO_2$ density at reservoir conditions within the SIOI. The table with the datapoints can be found in Appendix B.

Based on the results in Table 4.1, increasing the storage efficiency factor $E_{saline}$ significantly increases the predicted storage capacity. Alternatively, $CO_2$ density variability had a visible impact on estimated storage resources only at high storage efficiencies. Given that realistic $E_{saline}$ values are likely less than 10%, it is safe to assume that the density variability is negligible at these levels. Many calculations were performed with varying input parameters in this analysis; only a portion of them are presented in this thesis. The overall storage resources for the prospect range from 34 $MtCO_2$ (P90) to 1998 $MtCO_2$ (P10), with a P50 of 485 $MtCO_2$.

The comparative stage of this study (Section 4.3) refers to probabilistic (by $E_{saline}$) static capacities estimated by applying the optimistic NTG model and assuming $CO_2$ density of 650 kg/m$^3$ in volumetric calculations. The estimated $CO_2$ storage resources using the DOE-NETL method range from 39.6 Mt (P90) to 1977.6 Mt (P10), with a P50 of 553.7 Mt for the 62-km$^2$ reservoir. These values represent the upper bound (absolute roof) of $CO_2$ storage resources compared to estimates from more sophisticated methods, such as EASiTool.

### 4.2 Storage Resource Estimation using EASiTool

EASiTool (ET), which stands for Enhanced Analytical Simulation Tool, is a dynamic, web-based analytical solution developed by researchers at the Gulf Coast Carbon Center (GCCC) at the Bureau of Economic Geology to estimate $CO_2$ storage capacity in geologic reservoirs (Hosseini et al., 2018). It serves as a fast screening-level alternative to complex, time-consuming numerical simulations. Key features of EASiTool 5.1 include:

1. A module for calculating the maximum $CO_2$ storage capacity at both the reservoir and basin scales using both open and closed boundary condition scenarios
2. Defines the Area of Review (AoR) for a given storage site, which is the area around the $CO_2$ plume that would be impacted by the pressure front from $CO_2$ injection and brine displacement
3. A module for economic evaluation to optimize the number of injection and extraction wells

4. Sensitivity analyses and Monte Carlo simulations to quantify uncertainty (Hosseini et al., 2018).

One of the limitations of EASiTool is its use of an over-simplified geologic model, assuming a homogeneous, isotropic, isothermal, and horizontal reservoir with constant thickness, limited to a square-shaped area (Hosseini et al., 2018). For this reason, a smaller square area (20.75 $km^2$; ~8 $mi^2$) was cropped from the rectangular prospect (62 $km^2$; ~24 $mi^2$) that was defined in the previous section (Figure. 4.3).

Boundary condition options are a major control on how EASiTool estimates the pressure limits and, thus, maximum $CO_2$ storage capacity within a reservoir. The current version of EASiTool (v5.1; Wang and Hosseini, 2024) provides only two boundary condition options (open or closed), while the prospect area may be considered “semi-closed” due to the faults that act as potential barriers on two sides of the green square (Figure 4.3). For this reason, both open and closed boundary condition scenarios are tested to estimate the maximum storage capacity in both extreme cases.

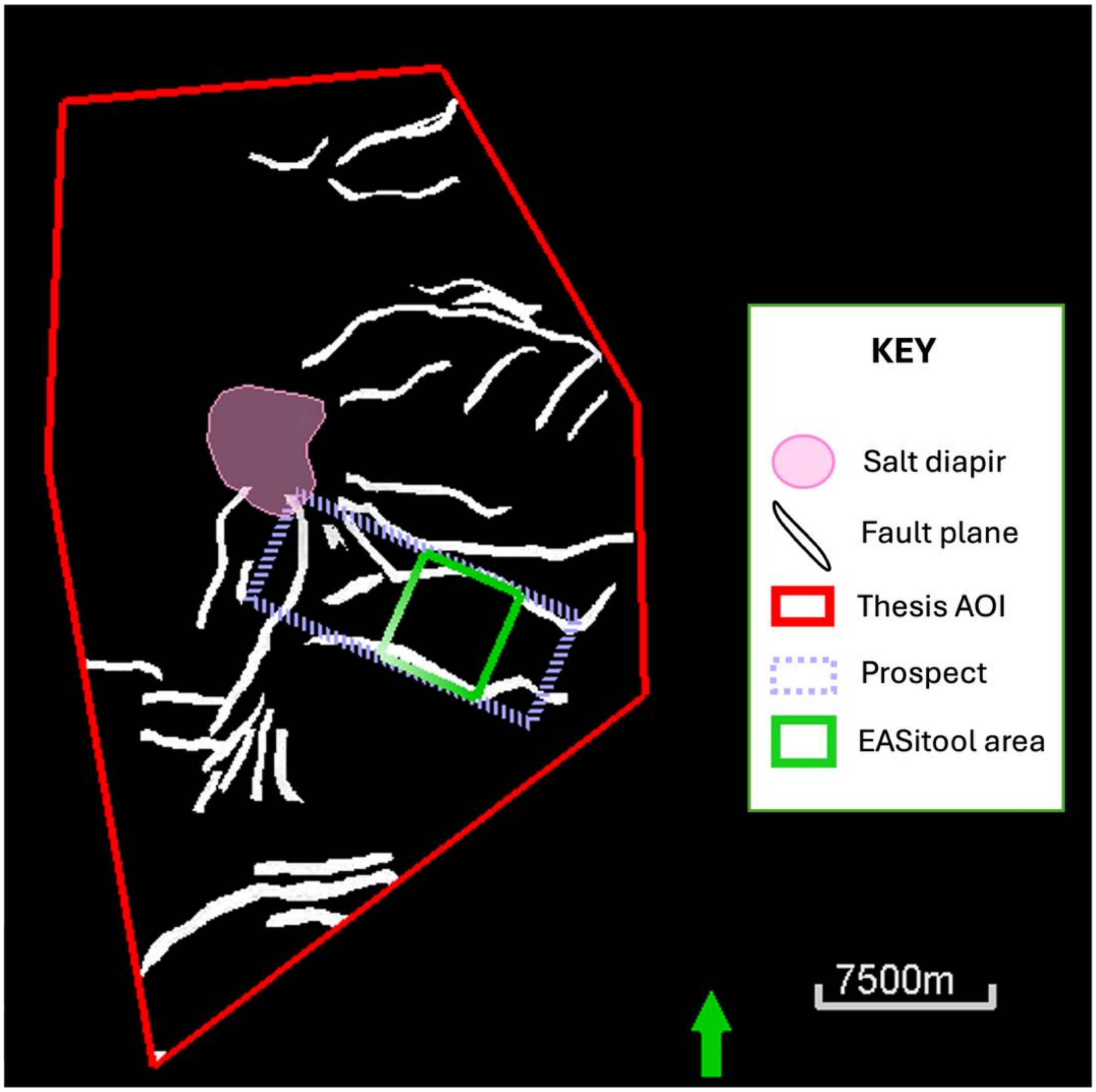


Figure 4.3: 2D map showing main structural features and polygons in this project. Analysis of the red polygon (~750 $km^2$) was covered in chapters 2 and 3 of this work. The dashed purple polygon (62 $km^2$) is the prospect area used for static $CO_2$ storage capacity estimation in section 4.1 and will be considered the reservoir area in the EASiTool analysis. The green polygon (20.75 $km^2$) is defined as the EASiTool project area for analysis in this section.

To run EASiTool, the user modifies an Excel input file template containing five input parameter modules to run through the web-based simulator: 1) reservoir properties,

2) maximum storage capacity estimation, 3) relative permeability parameters, 4) simulation properties, and 5) net present value parameters (Figure 4.4). Boundary conditions are set in the web-based EASiTool interface after uploading the input file.

| Project Settings | | | | | |
|---|---|---|---|---|---|
| Project Name | Field X CCS Project_Template | | | | |
| Select a simulation module | Maximum Storage Capacity | | | | |
| Select a unit system | SI Units | | | | |
| **Reservoir Properties** | **SI Value** | **Field Value** | **Input Value** | **Range** | **SI/Field Unit** |
| Initial Pressure | 20.00 | 2900.75 | 20.00 | >=7, <=55 | MPa |
| Initial Temperature | 65.00 | 149.00 | 65.00 | >=31, <=107 | °C |
| Thickness | 100.00 | 328.08 | 100.00 | <=500 | m |
| Salinity | 1.00 | 10000.00 | 1.00 | <=4 | mol/kg |
| Porosity | 0.20 | 0.20 | 0.20 | >=0, <=1 | ~ |
| Permeability | 100.00 | 100.00 | 100.00 | <=10000 | mD |
| Rock Compressibility | 5.00E-10 | 3.45E-06 | 5.00E-10 | <=1e-3 | 1/Pa |
| Reservoir Area | 1600.00 | 1000.00 | 1600.00 | >=Project Area | km^2 |
| | | | | | |
| **For Maximum Storage Capacity Module Only** | **SI Value** | **Field Value** | **Input Value** | **Range** | **SI/Field Unit** |
| Project Area | 500.00 | 386.10 | 500.00 | N/A | km^2 |
| Max Allowable Injection Pressure | 25.00 | 3625.94 | 25.00 | >=Initial Pressure, <=2.0x initial pressure | MPa |
| Number of Injection wells (min) | 1 | 1 | 1 | <=10x10, Square number | - |
| Number of Injection wells (max) | 81 | 81 | 81 | <=10x10, Square number | - |
| Number of Extraction wells | 0 | 0 | 0 | Among 0, 4 or 8 | - |
| Min Extraction Pressure | 19.00 | 2755.72 | 19.00 | <=initial reservoir pressure | MPa |
| Injection Duration | 10.00 | 10.00 | 10.00 | <=100 | year |
| | | | | | |
| **Simulation Properties** | **SI Value** | **Field Value** | **Input Value** | **Range** | **SI/Field Unit** |
| Injection Well Radius | 0.10 | 0.33 | 0.10 | >=0.05, <=0.5 | m |
| Critical Pressure Increase (default AOR value for interface) | 2.00 | 290.00 | 2.00 | <=50 | MPa |

| Relative Permeability Properties | SI Value | Range | SI Unit | Notes | |
|---|---|---|---|---|---|
| Water Corey Exponent (m) | 3.00 | >=1, <=6 | - | https://onepetro.org/spe/general-information/1221/2-phase-relative-permeability-models?searchresult=1 | Ton/day to MMT/yr |
| Gas Corey Exponent (n) | 3.00 | >=1, <=6 | - | | m^3/day to bbl/day |
| Endpoint Water Relative Permeability (kra0) | 1.00 | >=0.1, <=1 | - | | MPa to psi |
| Endpoint Gas Relative Permeability (krg0) | 0.30 | >=0.1, <=1 | - | | |
| Residual Water Saturation (Sar) | 0.20 | >=0.05, <=0.9 | - | | |
| Critical Gas Saturation (Sgc) | 0.10 | >=0.05, <=0.9 | - | | |
| | | | | | |
| **NPV Properties** | **Value** | **Range** | **SI Unit** | **Notes** | |
| Initial Investment | 500.00 | N/A | $M | Initial capital investment | |
| Annual Operational Cost (Upstream) | 10.00 | N/A | $M | Capture and transport | |
| Annual Operational Cost (Downstream) | 1.00 | N/A | $M/well | Storage, Monitor, etc. | |
| Tax Credit | 85.00 | N/A | $/ton | Tax Credit | |
| Discount Rate | 0.09 | 0-1 | - | https://www.investopedia.com/terms/n/npv.asp | |

Figure 4.4: EASiTool user input parameters Excel sheet (Hosseini et al., 2018). The values shown here are part of the standard input template (default values, later changed).

### 4.2.1 Inputs

For the purposes of this section, only three input modules were modified (reservoir properties, maximum storage capacity, and simulation properties), while the other modules (relative permeability and net present value properties) were left unchanged (Figure 4.4). For well placement, injection was simulated from a single injector at the midpoint of the reservoir area (green square polygon in Figure 4.3). Under the reservoir properties module, brine salinity was set to 1.2 mol/kg (~71,000 TDS), based on USGS produced water data from nearby fields in southwest Louisiana (Blondes et al., 2023). Rock compressibility was kept at the default of $5\times10^{-10}$ 1/Pa for consolidated rocks, although shallow-depth rocks (~6000 ft) may not be fully consolidated, so a range is tested for sensitivity analysis. A temperature gradient of 23 °C/km and a hydrostatic reservoir pressure gradient of 10.3 MPa/km (0.456 psi/ft) were assumed. In reservoir temperature and pressure calculations, the midpoint depth of the SIOI (6686 ft; ~2093 m) was chosen as the representative injection zone depth for EASiTool simulations. Using transforms derived from the data presented in Figure 4.1 (Nicholson, 2012; Wallace, 2013; Ramirez Garcia, 2019), temperature was calculated using:

$$T = 0.00701z + 23.88 \tag{4.2}$$

where,

$T$ = average reservoir temperature (°C)

$z$ = midpoint depth (ft)

The average reservoir pressure was calculated using the transform:

$$P_h = 0.465z + 14.7 \tag{4.3}$$

where,

$P_h$= hydrostatic pressure (psi)

$z$ = midpoint depth (ft)

The reservoir thickness parameter reflects the average net thickness of the pessimistic NTG model previously generated in subsection 3.4.2 of this thesis (85.1 m; ~280 ft). The project area is represented by the green polygon in Figure 4.3 (20.75 km$^2$; ~8 mi$^2$), and the reservoir area is set as 62 km$^2$, nearly three times the project area, to account for brine displacement. The average reservoir porosity was estimated from the "pessimistic NTG" model, and permeability was estimated using the following transform (Holtz, 2002):

$$\kappa = 7 \times 10^7 \times \phi_e^{9.61} \tag{4.4}$$

where,

$\kappa$ = permeability (mD)

$\phi_e$ = effective porosity (unitless)

However, previous characterization studies of Lower Miocene units in southwestern Louisiana show porosity ranges from 22 to 30% and permeabilities ranging from 100 to 2500 mD (Goddard and Zimmerman, 2003). To account for the high sensitivity of permeability to porosity, these ranges were included in sensitivity analyses.

To avoid fracturing the reservoir during injection, the maximum allowable injection pressure ($P_{max}$) must be less than the reservoir's fracture pressure, which is around 85-90% of the lithostatic pressure. Thus, the maximum injection pressure is assumed to be 80% of the lithostatic pressure ($P_{lith}$), which has a gradient of ~23 MPa/km (1 psi/ft) in the northern Gulf of Mexico (Wallace, 2013). Previous studies have fit a linear curve through density log data to obtain the lithostatic pressure (Ramirez Garcia, 2019):

$$P_{lith} = 0.006499z + 0.28598 \tag{4.5a}$$

Thus, the maximum allowable injection pressure ($P_{max}$) is calculated by:

$$P_{max} = 0.8 \times P_{lith} \tag{4.5b}$$

where,

$P_{lith}$= lithostatic pressure (MPa)

$z$ = midpoint depth (ft)

To delineate the area of review (AoR) for maximum capacity estimation, EASiTool requires the input of a critical pressure threshold that would drive the formation brine vertically upward to underground sources of drinking water (USDW), which are protected under EPA standards for Class VI injection well permitting (EPA, 2026). The critical (threshold) pressure increase from initial conditions is calculated by Ni et al. (2026, unpublished):

$$\Delta P_c = \frac{1}{2} g\xi(z_{inj} - z_{USDW})^2 \tag{4.6}$$

where,

$\Delta P_c$ = critical pressure increase (MPa)

$z_{inj}$ = representative depth of injection zone (m)

$z_{USDW}$ = representative depth of the base of USDW (m)

$g$ = acceleration due to gravity (9.8 m/s$^2$)

$\xi$ = density gradient (kg/m$^4$)

The density gradient ($\xi$) is a linear coefficient that depends on salinity increase and the geothermal gradient, and is defined by (Ni et al., 2026, unpublished):

$$\xi = \frac{\rho_{inj} - \rho_{USDW}}{z_{inj} - z_{USDW}} \tag{4.7}$$

where,

$\rho_{inj}$ = injection zone fluid density (~1050 kg/m$^3$)

$\rho_{USDW}$ = USDW fluid density (~1000 kg/m$^3$)

Even though it is highly unrealistic for a 20-km$^2$ reservoir, the maximum number of injection wells was set to 80 to test the effect of increasing the number of injection wells on capacity, pressure limits, and $CO_2$ plume size in open versus closed systems. Moreover, for the sake of estimating the maximum storage capacity that can retain $CO_2$ based on pressure limits, no extraction wells (for brine production) were included in the simulations presented in this work.

Table 4.2 EASiTool input parameters adjusted for this study. The ranges tested for sensitivity analysis are arbitrary, except for permeability, which was based on previous characterizations.

| Module | Parameter | Value (Range) | Unit |
|---|---|---|---|
| **Reservoir properties** | **Initial Pressure** | 21.69 (17.35-26.03) | MPa |
| | **Initial Temperature** | 72.01 (57.61-86.41) | °C |
| | **Thickness** | 85.1 (60-90) | m |
| | **Salinity** | 1.2 (0.96-2.0) | mol/kg |
| | **Porosity** | 21 (20-30) | % |
| | **Permeability** | 200 (100-2500) | mD |
| | **Rock Compressibility** | 5.00E-10 (4.75E-10-5.10E-10) | 1/Pa |
| | **Reservoir Area** | 62.00 | $km^2$ |
| **Maximum Storage Capacity** | **Project Area** | 20.75 | $km^2$ |
| | **Max Allowable Injection Pressure** | 30(25-35) | MPa |
| | **Min Number of Injection Wells** | 1 | - |
| | **Max Number of Injection Wells** | 80 | - |
| | **Injection Duration** | 20 | years |
| **Simulation properties** | **Critical Pressure Increase (default AoR value for interface)** | 0.4625 | MPa |

### 4.2.2 Outputs

The input parameters in Table 4.2 were run through the web-based simulator for two boundary condition scenarios (open and closed), and the results are summarized in Table 4.3. Sensitivity analyses were run for both scenarios to identify the parameters with the greatest impact on storage capacity (Figure 4.5).

Table 4.3 Summary of EASiTool simulation results using open and closed boundary scenarios for one injector over a 20-year injection period.

| **Boundary conditions** | **Closed** | **Open** |
|---|---|---|
| **Total $CO_2$ capacity (Mt)** | 5.69 | 97.15 |
| **Injection rate (Mt/year)** | 0.28 | 4.86 |
| **$CO_2$ plume radius (km)** | 0.46 | 1.91 |

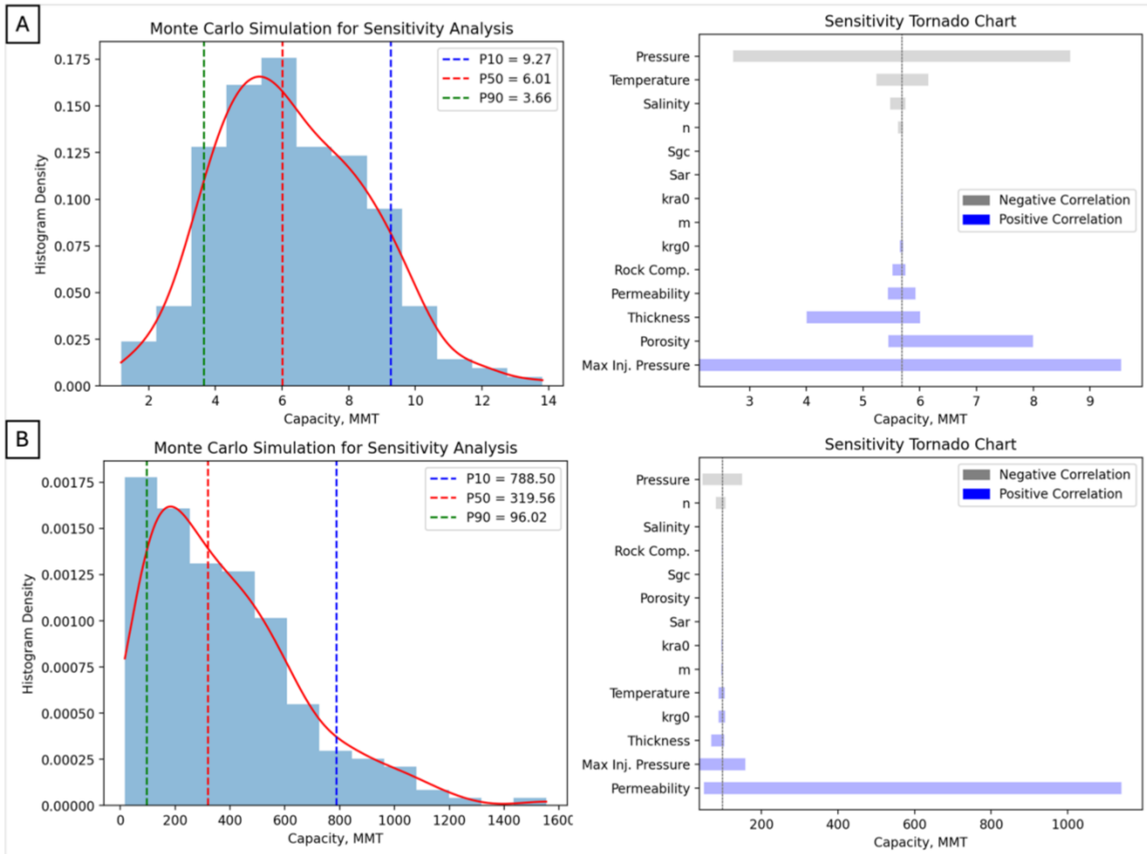


Figure 4.5: EASiTool capacity Monte Carlo sensitivity analyses (left) and tornado charts (right) for A) closed boundary, and B) open boundary scenarios.

The sensitivity analysis showed that for closed boundary conditions, capacity ranges from 3.7 to 9.3 Mt, with a P50 of 6 Mt for the 62-km$^2$ prospect. The variables with the greatest impact on capacity in closed-boundary scenarios are the maximum allowable injection pressure ($P_{max}$), which validates the conclusions of Wang et al. (2024), followed by initial reservoir pressure ($P_h$), porosity, and reservoir net thickness. On the other hand, open boundary conditions yield a wide range of capacities ranging from 96 to 789 Mt, with a P50 of 320 Mt for the prospect. The variable with the highest impact on capacity for this scenario was permeability (Figure 4.5b). In reality, the reservoir is likely partially compartmentalized by faults, so the boundary conditions are semi-closed. Storage resources would thus be somewhere between the closed and open boundary conditions.

## 4.3 Comparative Results

### 4.3.1 Static capacity vs. EASiTool

Similar to oil and gas exploration, the early stages of CCS projects are associated with the highest uncertainty in storage resource estimates. A static volumetric estimate of $CO_2$ storage resource using the US-DOE method is a fair starting point; however, the actual storage capacity can only be lower, possibly by orders of magnitude. Additional data, expertise, and computational force are required to run a reservoir simulation to obtain more accurate estimates. For these reasons, EASiTool serves as a better screening alternative to the static capacity method in terms of storage capacity accuracy and a much faster alternative to computationally expensive reservoir simulations in the early stages of a project (Figure 4.6). Table 4.4 summarizes key differences between the methods mentioned above.

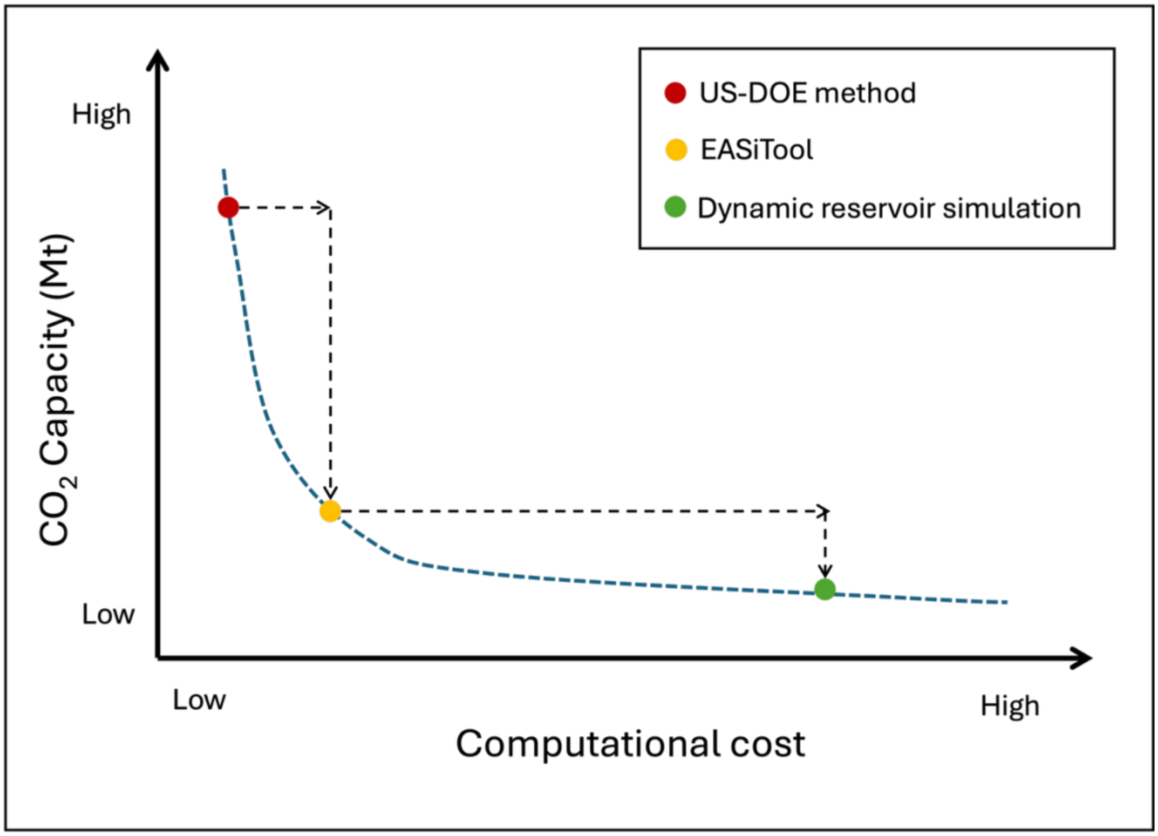


Figure 4.6: Schematic illustration of relative $CO_2$ storage capacities of three methods with varying degrees of computational cost (not to scale).

Table 4.4: Comparison between three methods for estimating the $CO_2$ storage resource for a geologic site (Goodman et al., 2011; Hosseini et al., 2018; Leng et al., 2024).

| **Aspect** | **US DOE-NETL** | **EASiTool** | **Reservoir Simulation** |
|---|---|---|---|
| **Method type** | Static, volumetric | Semi-dynamic analytical | Fully dynamic numerical |
| **Geological detail** | Regional-scale, highly simplified | Intermediate; assumes homogeneous or layered systems | High-resolution heterogeneous models |
| **Computational cost** | Very low | Low | High |
| **Accuracy** | Very low | Medium | High |
| **Key governing physics** | Simplified volumetric balance | Pressure diffusion and simplified plume migration | Multiphase flow, relative permeability, capillarity, and geomechanics |
| **Time dependency** | No time dimension | Time-dependent injection and pressure evolution | Fully time-dependent injection and post-injection behavior |
| **Pressure consideration** | Indirect (through storage efficiency factors) | Explicit analytical pressure buildup calculation | Fully modeled pressure field |
| **Boundary conditions** | Not explicitly handled | Simplified (closed, open, leaky systems can be approximated) | Fully defined (faults, aquifers, boundaries) |

For proper comparison, the same reservoir parameters were used to estimate the maximum $CO_2$ storage capacity using the static method and the EASiTool (ET) method.

This subsection refers to static capacities calculated for the pessimistic (sand-only) model previously defined in this thesis, with variable efficiency factors to approximate the equivalent efficiency factors for ET estimates. The combined results are illustrated in Figure 4.7.

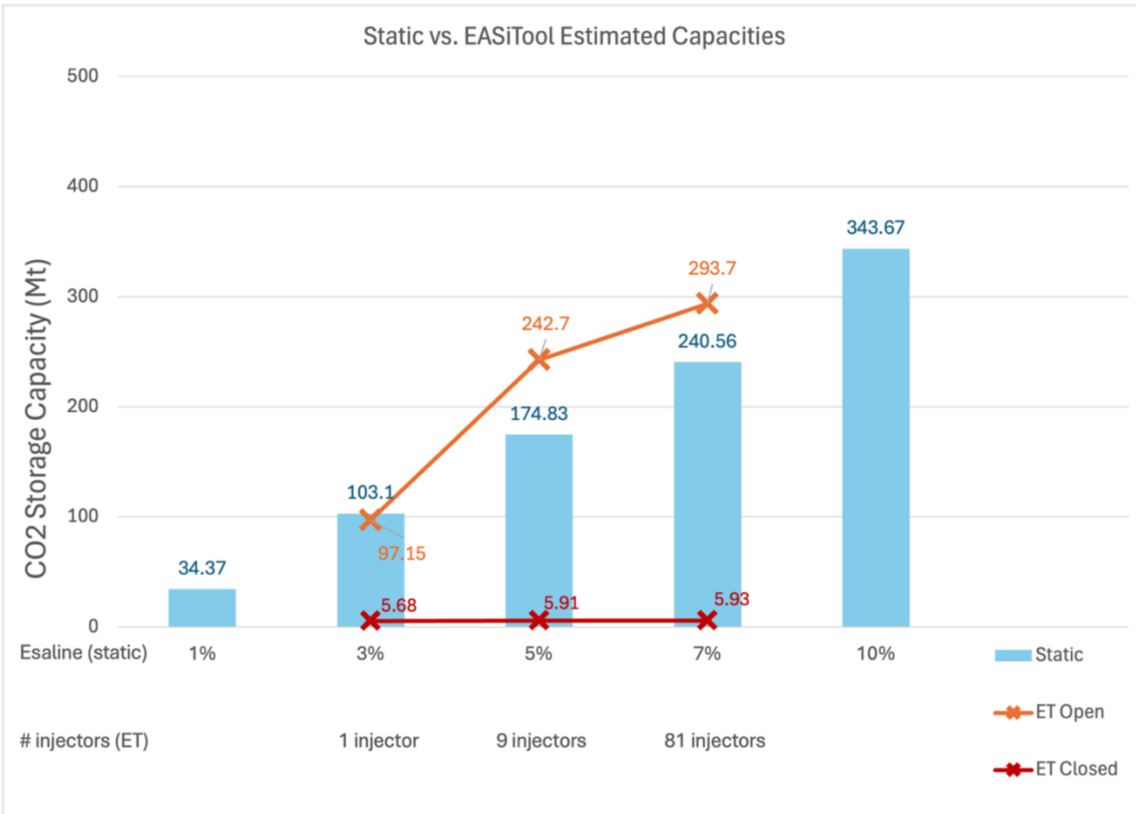


Figure 4.7: $CO_2$ storage capacities estimated from two methods for the same dataset. Static capacities (blue bars) as a function of the storage efficiency factor ($E_{saline}$), ranging from 1 to 10%. Dynamic EASiTool capacities are estimated for two boundary condition scenarios (open and closed), and three injector designs (1, 9, and 81 injectors) for a 20-year injection simulation.

The results in Figure 4.7 show that, for the same dataset, EASiTool estimates are much lower than static estimates because the pressure limit is usually reached before the pore volume limit, confirming the conclusions drawn from Bump and Hovorka (2024).

EASiTool capacities for an open boundary scenario are similar to static capacities, with 3-7% storage efficiency over a 20-year injection period. However, a 7% efficiency does not necessarily mean 7% of the 62 km² reservoir is independently available. It may mean the 62 km² reservoir is borrowing pressure support from a much larger connected aquifer. The number of injectors highly affects the estimated capacity in open-boundary conditions, but one to four wells is a realistic range for the number of injectors in CCS projects. On the other hand, closed-boundary EASiTool scenarios provide capacity estimates equivalent to <0.5% storage efficiency in static estimates, with little to no variability across different numbers of injectors. These findings validate an internal GCCC analysis that reports ET estimates for maximum storage capacity are generally 1-3% of static volumetric capacity assessments for a 10-year injection simulation. The percentages shown from this thesis research would be lower (closer to 1-3%) for a shorter injection period.

#### 4.3.2 Comparison with nearby studies

While many studies provide a mass value for storable $CO_2$ at a CCS site, there is no benchmark to determine whether this capacity is realistic, especially for this specific geologic site. When $CO_2$ storage resource numbers are provided to management, the following questions must first be answered: What is the relative size of this storable volume to the study area? What methods were used, and what does it mean for the uncertainty of these estimates? In this section, a new metric is proposed to easily compare results from studies of different scales (regional to field-scale) by normalizing the resulting capacity to area and thickness to obtain a capacity per square kilometer per meter thickness (Mt/km$^2$/m). This way, the capacities from different studies become comparable by efficiency factors and $CO_2$ densities. The results of this study are compared with storage resource estimates by Wallace (2013), Ruiz (2019), Ramirez Garcia (2019), and Bump and Hovorka (2024), all of which are generally for the same geological setting and interval but at different scales. The purpose here is to determine whether capacity estimates from these studies consistently fall within the range estimated in this study for this geologic site (Figure 4.8). For simplicity in comparison, the values presented from other studies refer to their P50 capacity estimates. The red squares in Figure 4.8 represent two different intervals from the Ruiz (2019) study: the top value that falls in the trendline refers to the SIOI interval, is highly similar to the thickness interval considered in this study. The lower datapoint that falls below a trendline was estimated for the HC Sand interval (see Appendix C).

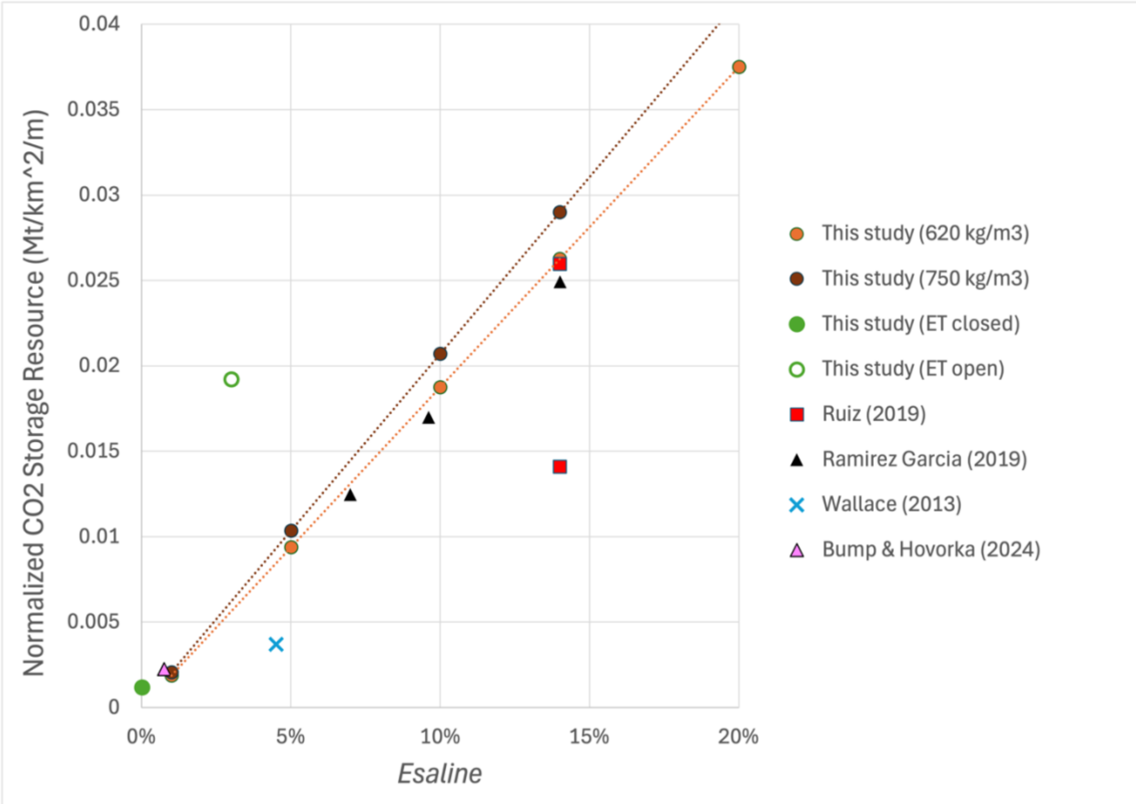


Figure 4.8: Normalized storage capacities in the Offshore Texas State Waters area versus the storage efficiency factor $E_{saline}$, across multiple studies covered in this thesis. A table containing data points from other studies is available in Appendix C.

The results in Figure 4.8 show that normalized capacities from other studies for the same geologic interval are consistently closer to those estimated in this study, using the pessimistic NTG model and assuming a relatively low $CO_2$ density at reservoir conditions. The storage resource estimated using EASiTool's closed-boundary scenario is closest to <1% efficiency factors in static estimates, while the open-boundary scenario yields a capacity equivalent to 10% storage efficiency.

## 4.4 SUMMARY

- Two methods are covered in this study for $CO_2$ storage capacity estimation: 1) the DOE-NETL static volumetric method, and 2) the pressure-based EASiTool method
- The static method calculates storage capacity using net pore volume, porosity, $CO_2$ density, and a storage efficiency factor. The storage efficiency factor has the highest impact on the estimated capacity
- Testing different scenarios, static estimates for the prospect site ranges from 34 to 2000 million tons (Mt) of $CO_2$, with a P50 estimate of 485 Mt
- EASiTool dynamically estimates storage capacity based on pressure limits, Area of Review (AoR), and injection constraints, using both open and closed boundary condition scenarios to account for geological complexity
- For closed boundaries, storage resources were found to be equivalent to <1% storage efficiency (P50 estimate 6 Mt).
- For open boundaries, storage resources were equivalent to 3-7% storage efficiencies (P50 estimate 320 Mt).
- In reality, the system is semi-closed due to faults, so the storage resources would range between the open and closed boundary conditions' estimates
- Pressure limits and permeability are key factors influencing the $CO_2$ storage resource estimates for this prospect, based on EASiTool sensitivity analyses
- Comparing the two methodologies, the static method provides an upper bound value for $CO_2$ storage resources using reasonable storage efficiencies (1-10%). EASiTool, on the other hand, gave lower storage resource

estimates, reflecting more realistic scenarios that are constrained by pressure and time limits.

- The results are also compared with other studies using a normalized capacity per area/thickness, showing that the estimates for this site fit regional trends when using realistic parameters, which allowed for gauging realistic capacity ranges for this geologic site.

# Chapter 5: Discussion

The first main part of this research covered the geologic characterization of Lower Miocene reservoirs in Texas State Waters (Chapter 2) using standard workflows for 3D seismic mapping of horizons and faults, along with well log correlation and analysis. Extracted seismic attributes revealed lateral changes in seismic reflector amplitudes, suggesting complex facies changes within the massive deltaic lobe system, which is only partially covered in the study area. The outputs of this workflow include the structural elements needed to build a 3D structural grid in the next stage of this work.

The overall structure from seismic interpretation revealed a subtle dip in the beds and thickening towards the basin, away from a salt diapir that may have been growing during deposition (see Figure 2.4). The lack of significant thickness change across the faults indicates that faulting may not have been active during the deposition of the interval of interest. Well log analysis allowed classification of lithofacies based on the volumetric fraction of shale calculated at well locations as sand, silty-sand, or shale. Porosity logs, wherever available, were used to calculate the effective porosity, a continuous log constrained by lithofacies codes at well locations. These properties were to be populated across the 3D model built in Chapter 3, where the 3D seismic attribute (RMS amplitude) volume was incorporated as a trend volume to guide the distribution of properties between well locations. From the 3D models, a 62-$km^2$ area was identified as the prospect, located southeast and downdip of a salt diapir and bounded by two major growth faults striking parallel to the overall dip orientation of the beds.

Uncertainties in the 3D model stem from the low resolution of the seismic data; the structural model's resolution could have been improved if more seismic horizons had been interpreted between the three arbitrary surfaces chosen in this study, possibly revealing features that may have been missed during the seismic interpretation stage of this work. Moreover, the lack of porosity curves near the prospect area, except for a few wells with Lower Miocene porosity data in a deeper geologic setting outside the study area, may lead to an underestimation of porosity in the shallower setting (this study). This would later impact the confidence in the porosity and permeability parameters used in storage resource estimation, Furthermore, the NTG assumptions applied in this study were designed to estimate net pore volume available for $CO_2$ occupancy and should not be interpreted as equivalent flow barriers for dynamic simulation. Silty-sand intervals assigned NTG values of 0 or 0.15 may still contribute significantly to pressure dissipation through brine flow. Consequently, subsequent dynamic reservoir simulations should distinguish between storage volume and pressure-support volume by assigning permeability properties to lower quality facies rather than treating them as impermeable zones. This distinction may increase effective pressure communication and dynamic storage resource estimates relative to the static NTG-based calculations.

The third and final workflow, covered in Chapter 4 of this work, quantifies $CO_2$ storage resources for the storage prospect and interval. Two methods were used for $CO_2$ capacity estimation: the first is a volumetric method, developed by the US DOE, using the net pore volumes calculated from the 3D models and assuming a range of $CO_2$ densities and storage efficiency factors (Goodman et al., 2011). Early regional-scale assessments required a simple volumetric method that could estimate storage resources across large basins without detailed reservoir simulations. Consequently, the DOE-NETL methodology adopted efficiency factors derived from analytical studies, numerical simulations, and expert judgment to account for plume sweep efficiency, reservoir heterogeneity, trapping processes, and pressure limitations. Goodman et al. (2011) formalized this approach by developing probabilistic efficiency factor ranges for saline formations and recommending P90, P50, and P10 values for use in regional resource assessments. Their objective was not to predict project-scale storage performance, but rather to provide a consistent methodology for comparing large geographic areas where detailed characterization data were unavailable.

The capacities estimated using this method were expected to be highly overestimated, even when the most conservative storage efficiencies are assumed, due to the simplicity of the geologic model and the method itself. Since Goodman et al. (2011) was published, many studies have shown that volumetric estimates often overstate practical storage capacity because they do not explicitly model pressure buildup (Wang et al., 2024). In numerous reservoirs, injection pressure limits usually become the main constraint before the pore space is fully filled with $CO_2$. This begs the question of whether the higher efficiency factors used in regional assessments are suitable for site-specific project evaluations. As a result, subsequent research and simulation tools estimate capacities based on about a few percent of the volumetric efficiency (~1% for closed systems). Therefore, storage efficiency factors should be seen as screening-level resource indicators rather than precise measures of commercially achievable storage capacity.

The second methodology uses a semi-dynamic analytical tool that considers pressure constraints that limit the amount of $CO_2$ that can be injected into the reservoir and displace brine. The EASiTool methodology considers initial reservoir conditions as well as project duration and boundary conditions (Hosseini et al., 2018). It was anticipated that open-boundary scenarios would yield capacities that are too high but still lower than the most conservative static estimate, whereas closed-boundary scenarios would yield a lower-bound capacity value that is likely more realistic. EASiTool simulations assumed a 20-year injection period and a variable number of injector wells to assess the maximum possible storage capacity for both open and closed scenarios.

The results in this analysis show that static capacity ranges from 36 Mt (assuming 1% efficiency; realistic) to 1805 Mt (50% efficiency; unrealistic), with a P50 of 505 Mt (14% efficiency; optimistic) for the 62-km$^2$ reservoir. EASiTool, on the other hand, showed that the maximum storage capacity for a 20-year injection period using one injector is approximately 5.7 Mt for closed-boundary scenarios and 97 Mt for open-boundary scenarios. Closed-boundary conditions yielded a much lower maximum storage capacity, about 82% lower than the most conservative static estimate, equivalent to a storage efficiency of less than 0.5% (Figure 4.7). The number of injector wells significantly affects estimated capacities only in open-boundary scenarios. Built-in sensitivity analysis in EASiTool showed that for an open-boundary reservoir, capacity ranges are wide and most sensitive to permeability (Figure 4.5). Alternatively, for a closed-boundary reservoir, the top three parameters with the highest impact on capacity estimates are the maximum injection pressure, initial reservoir pressure, and porosity. These findings are supported by Wang et al. (2024), who conclude that storage efficiency is an uncertainty parameter constrained by pressure buildup and available pore volume.

The comparison between static and EASiTool estimates highlights the importance of pressure support and connected pore volume. Open-boundary EASiTool scenarios yielded storage resources equivalent to approximately 3-7% storage efficiency factors in static calculations. However, efficiencies above approximately 1% likely require brine displacement beyond the mapped reservoir volume considered in this study. Consequently, the higher storage resources estimated for open-boundary scenarios should not be interpreted as storage occurring solely within the 62 km$^2$ prospect. Rather, these estimates imply hydraulic communication with a larger connected aquifer system that provides additional pressure-support volume for displaced brine. Therefore, practical storage resources depend not only on local pore volume, but also on the extent and connectivity of surrounding reservoir units.

To compare the resulting capacities with multiple studies of varying scales (from regional to field-scale), this study proposed a metric that normalizes capacity by area and thickness, helping constrain the realistic range of $CO_2$ storage resources for this particular geologic setting (Figure 4.8). It was found that both the static and closed-boundary EASiTool estimates from this study follow a linear trend that is aligned with regional and field-scale estimates from other studies for the same storage interval of interest within the vicinity. For storage efficiencies ranging from 0.05 to 10%, normalized storage resources range from 0.003 to 0.02 Mt/km$^2$/m-thickness, respectively. These values may be considered a "realistic" $CO_2$ storage resource range for Lower Miocene reservoirs in Texas State Waters, and should be further constrained through dynamic reservoir simulations.

# Chapter 6: Conclusions and Recommendations

## 6.1 Conclusions

To meet global climate goals and remain below the 2°C mark for global mean temperature increase since the industrial revolution, approximately 5 billion tons of $CO_2$ must be removed from the atmosphere annually. Most greenhouse gas emissions come from industrial facilities, such as power plants and hydrocarbon refineries. A key strategy for large-scale emission reduction from these facilities is carbon capture and geologic sequestration (CCS). However, screening for storage sites is often associated with high uncertainty and risk for potential investors in CCS projects. The estimated $CO_2$ storage resource for a site is a key driver of project cost in the early screening stages. Quantifying a reservoir's storage capacity with high accuracy requires time, data, resources, and expertise in reservoir modeling. In the early stages, however, simpler methods can be used to provide capacity ranges that are constrained over time.

The northern GOM contains abundant subsurface data, point-source emitters, infrastructure, and a geologic setting favoring permanent $CO_2$ storage. The Lower Miocene Series was shaped by rapid delta progradation along the shelf margin and by increased sedimentation rates through multiple fluvial channels. Extensive faulting and salt diapirism shaped the landscape and compartmentalized the reservoir into regions capable of retaining injected $CO_2$. Multiple studies have assessed the storage capacity of Lower Miocene formations in offshore Texas State Waters at different scales and quantified the storage resource using multiple methods of varying complexity. However, these studies had not yet been combined or compared to constrain the actual $CO_2$ capacity for Lower Miocene reservoirs in this region.

This research had three main objectives: (1) to identify a potential prospect (tens of $km^2$) for project-scale CCS in saline aquifers in offshore southeast Texas, (2) to quantify the storage resource of the prospect using more than one method, and (3) to compare the estimated capacities to each other as well as to nearby studies for the same geologic setting. To achieve these objectives, this research applied site-specific geologic characterization and 3D modeling to Lower Miocene rocks southeast of Jefferson County in offshore Texas State Waters to identify potential storage sites and constrain their CO2 storage resources. Static 3D geologic models (lithofacies and porosity) were constructed from 3D seismic interpretation and well log analysis in the study area, from which a prospect site has been identified for storage resource assessment.

This work has demonstrated ways to gauge $CO_2$ storage resources in Texas State Waters using two fast, screening-level methodologies before resorting to full-flow reservoir simulations. Static capacity calculations using the Goodman et al. methodology, in conjunction with the EASiTool methodology, enabled quantification of CO2 storable volume in Miocene aquifers. The static Goodman et al. methodology yielded endpoint storage resource estimates that may be considered realistic when storage efficiencies are closer to 1%. EASiTool, on the other hand, would provide storage resource estimates with efficiencies of 3-7% for open systems, and <0.05% for closed systems.

Still, there are limitations in the storage resource assessment methods covered in this study. Volumetric assessments do not account for dynamic parameters such as time and pressure, and no injection from an injection well was simulated. Therefore, the $CO_2$ plume and surrounding area of elevated pressure were not explicitly modeled, and storage resources were conceptualized using a volumetric calculation for each grid cell, with assigned average porosity, thickness, and area (Figure 6.1). Alternatively, EASiTool incorporates time and pressure constraints to model the $CO_2$ plume and area of elevated pressure around it. However, its limitation lies in its assumption of an idealized, homogeneous reservoir model, in which the $CO_2$ plume is modeled radially from an injection well, saturating the surrounding rock with 100% $CO_2$ (Figure 6.1). It does not account for lateral and vertical heterogeneity and thus does not model the spatial variability in $CO_2$ saturation within the plume. Full-physics reservoir simulations are still needed to model the shape of the injected $CO_2$ plume and pressure space to plan for injection and monitoring well locations (Figure 6.1).

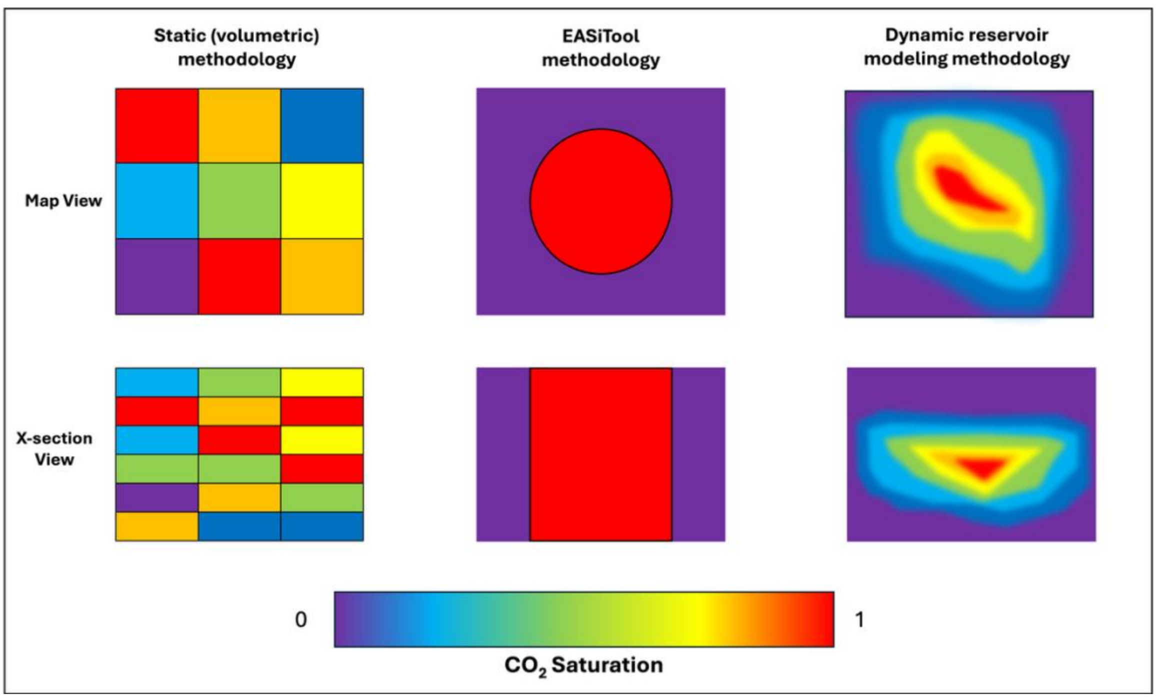


Figure 6.1: Schematic illustration of conceptualized $CO_2$ plume distributions using the three methodologies mentioned in this study for $CO_2$ storage resource assessments (not to scale).

## 6.2 RECOMMENDATIONS

Future work should incorporate the results from this study into dynamic reservoir simulations to constrain the storage resources of the prospect discussed in this thesis and delineate the extent of $CO_2$ plume for project-scale planning. The Petrel project may be accessed with permission from the GCCC.

# Appendices

## APPENDIX A

Full well log inventory table for wells in the study area.

| UWI | Facies | | Density | Sonic | Porosity | | Resistivity | TOTAL LOGS |
|---|---|---|---|---|---|---|---|---|
| | SP | GR | RHOB | DT | NPHI | DPHI | ILD | |
| 42708401950000 | 1 | 1 | 0 | 1 | 1 | 1 | 1 | **6** |
| 42708401590000 | 1 | 1 | 1 | 1 | 1 | 0 | 1 | **6** |
| 42708401350000 | 1 | 1 | 1 | 1 | 1 | 0 | 1 | **6** |
| 42708400920000 | 1 | 1 | 1 | 1 | 1 | 0 | 1 | **6** |
| 42708400920000 | 1 | 1 | 1 | 1 | 1 | 0 | 1 | **6** |
| 42708403090000 | 1 | 1 | 0 | 0 | 1 | 1 | 1 | **5** |
| 42708403410000 | 0 | 1 | 1 | 1 | 1 | 0 | 1 | **5** |
| 42708303250000 | 1 | 1 | 1 | 1 | 0 | 0 | 1 | **5** |
| 42708400400000 | 1 | 0 | 0 | 1 | 1 | 1 | 1 | **5** |
| 42708303070000 | 1 | 1 | 0 | 1 | 0 | 1 | 1 | **5** |
| 42708302240000 | 1 | 0 | 1 | 1 | 1 | 0 | 1 | **5** |
| 42708302760000 | 1 | 1 | 0 | 1 | 0 | 0 | 1 | **4** |
| 42708401580000 | 1 | 1 | 0 | 0 | 0 | 1 | 1 | **4** |
| 42708303490000 | 1 | 1 | 0 | 0 | 1 | 1 | 0 | **4** |
| 42708402050000 | 1 | 1 | 0 | 1 | 0 | 0 | 1 | **4** |
| 42708302350000 | 1 | 1 | 0 | 1 | 0 | 0 | 1 | **4** |
| 42708402040000 | 1 | 1 | 0 | 1 | 0 | 0 | 1 | **4** |
| 42708302670000 | 1 | 1 | 0 | 0 | 0 | 0 | 1 | **3** |
| 42245030100000 | 1 | 0 | 0 | 1 | 0 | 0 | 1 | **3** |
| 42606300070000 | 1 | 0 | 0 | 1 | 0 | 0 | 1 | **3** |
| 42245324090000 | 1 | 1 | 0 | 0 | 0 | 0 | 1 | **3** |
| 42245303970000 | 1 | 0 | 0 | 1 | 0 | 0 | 1 | **3** |
| 42245323210000 | 1 | 0 | 0 | 1 | 0 | 0 | 1 | **3** |
| 42708300810000 | 1 | 0 | 0 | 1 | 0 | 0 | 1 | **3** |
| 42708301080000 | 1 | 0 | 0 | 1 | 0 | 0 | 1 | **3** |
| 42708300350000 | 1 | 0 | 0 | 1 | 0 | 0 | 1 | **3** |
| 42708302350100 | 0 | 1 | 0 | 0 | 1 | 1 | 0 | **3** |
| 42245320700000 | 1 | 1 | 0 | 0 | 0 | 0 | 1 | **3** |
| 42708302980000 | 1 | 1 | 0 | 0 | 0 | 0 | 1 | **3** |

| | | | | | | | | |
|---|---|---|---|---|---|---|---|---|
| 42708300870000 | 0 | 1 | 0 | 0 | 1 | 1 | 0 | **3** |
| 42708300740000 | 1 | 0 | 0 | 1 | 0 | 0 | 1 | **3** |
| 42245031270000 | 1 | 0 | 0 | 0 | 0 | 0 | 1 | **2** |
| 42245302740000 | 1 | 0 | 0 | 0 | 0 | 0 | 1 | **2** |
| 42245302130000 | 1 | 0 | 0 | 0 | 0 | 0 | 1 | **2** |
| 42245320600000 | 1 | 0 | 0 | 0 | 0 | 0 | 1 | **2** |
| 42708404430000 | 1 | 1 | 0 | 0 | 0 | 0 | 0 | **2** |
| 42708302640000 | 1 | 0 | 0 | 0 | 0 | 0 | 1 | **2** |
| 42708302400000 | 1 | 0 | 0 | 0 | 0 | 0 | 1 | **2** |
| 42708300800000 | 1 | 0 | 0 | 0 | 0 | 0 | 1 | **2** |
| 42708300630000 | 1 | 0 | 0 | 0 | 0 | 0 | 1 | **2** |
| 42245320700100 | 0 | 0 | 0 | 0 | 1 | 1 | 0 | **2** |
| 42708401590100 | 1 | 0 | 0 | 0 | 0 | 0 | 1 | **2** |
| 42708000670000 | 1 | 0 | 0 | 0 | 0 | 0 | 1 | **2** |
| 42708404650000 | 1 | 0 | 0 | 0 | 0 | 1 | 0 | **2** |
| 42708000640000 | 1 | 0 | 0 | 0 | 0 | 0 | 1 | **2** |
| 42245303580000 | 1 | 0 | 0 | 0 | 0 | 0 | 1 | **2** |
| 42708302930000 | 1 | 0 | 0 | 0 | 0 | 0 | 1 | **2** |
| 42708300660000 | 1 | 0 | 0 | 0 | 0 | 0 | 1 | **2** |
| 42708000680000 | 1 | 0 | 0 | 0 | 0 | 0 | 1 | **2** |
| 42708300770000 | 1 | 0 | 0 | 0 | 0 | 0 | 1 | **2** |
| 42708300750000 | 1 | 0 | 0 | 0 | 0 | 0 | 1 | **2** |
| 17023020810000 | 1 | 0 | 0 | 0 | 0 | 0 | 1 | **2** |
| 42245031780000 | 1 | 0 | 0 | 0 | 0 | 0 | 1 | **2** |
| 42245323930000 | 1 | 1 | 0 | 0 | 0 | 0 | 0 | **2** |
| 42708302880000 | 1 | 0 | 0 | 0 | 0 | 0 | 1 | **2** |
| 42708302270000 | 1 | 0 | 0 | 0 | 0 | 0 | 1 | **2** |
| 42245322460000 | 1 | 0 | 0 | 0 | 0 | 0 | 1 | **2** |
| 42606301580000 | 1 | 0 | 0 | 0 | 0 | 0 | 1 | **2** |
| 42245311670000 | 1 | 0 | 0 | 0 | 0 | 0 | 1 | **2** |
| 42245328410000 | 1 | 1 | 0 | 0 | 0 | 0 | 0 | **2** |
| 42245323860000 | 1 | 1 | 0 | 0 | 0 | 0 | 0 | **2** |
| 42708303300000 | 1 | 0 | 0 | 0 | 0 | 0 | 1 | **2** |
| 42245321340000 | 1 | 1 | 0 | 0 | 0 | 0 | 0 | **2** |
| 42708300270000 | 1 | 0 | 0 | 0 | 0 | 0 | 1 | **2** |
| 42245031770000 | 1 | 0 | 0 | 0 | 0 | 0 | 1 | **2** |
| 42245031240000 | 1 | 0 | 0 | 0 | 0 | 0 | 1 | **2** |

| | | | | | | | | |
|---|---|---|---|---|---|---|---|---|
| 42245033650000 | 1 | 0 | 0 | 0 | 0 | 0 | 1 | **2** |
| 42708303510000 | 1 | 0 | 0 | 0 | 0 | 0 | 1 | **2** |
| 42245031230000 | 1 | 0 | 0 | 0 | 0 | 0 | 1 | **2** |
| 42245033650100 | 1 | 0 | 0 | 0 | 0 | 0 | 1 | **2** |
| 42245031220000 | 1 | 0 | 0 | 0 | 0 | 0 | 1 | **2** |
| 42708405580000 | 1 | 1 | 0 | 0 | 0 | 0 | 0 | **2** |
| 42708303590000 | 1 | 0 | 0 | 0 | 0 | 0 | 1 | **2** |
| 42708000010000 | 1 | 0 | 0 | 0 | 0 | 0 | 0 | **1** |
| 42708000040000 | 1 | 0 | 0 | 0 | 0 | 0 | 0 | **1** |
| 42708303690000 | 0 | 1 | 0 | 0 | 0 | 0 | 0 | **1** |
| 42245015420000 | 1 | 0 | 0 | 0 | 0 | 0 | 0 | **1** |
| 42245021130000 | 1 | 0 | 0 | 0 | 0 | 0 | 0 | **1** |
| 42708000120000 | 1 | 0 | 0 | 0 | 0 | 0 | 0 | **1** |
| 42245320950300 | 1 | 0 | 0 | 0 | 0 | 0 | 0 | **1** |
| 42245320950000 | 1 | 0 | 0 | 0 | 0 | 0 | 0 | **1** |
| 42245302130100 | 1 | 0 | 0 | 0 | 0 | 0 | 0 | **1** |
| 42245311560000 | 1 | 0 | 0 | 0 | 0 | 0 | 0 | **1** |
| 42708303570000 | 1 | 0 | 0 | 0 | 0 | 0 | 0 | **1** |
| 42708000070000 | 1 | 0 | 0 | 0 | 0 | 0 | 0 | **1** |
| 42708000100000 | 1 | 0 | 0 | 0 | 0 | 0 | 0 | **1** |
| 42708000130000 | 1 | 0 | 0 | 0 | 0 | 0 | 0 | **1** |
| 42715000310000 | 1 | 0 | 0 | 0 | 0 | 0 | 0 | **1** |
| 42708303390000 | 1 | 0 | 0 | 0 | 0 | 0 | 0 | **1** |
| 42708303430000 | 1 | 0 | 0 | 0 | 0 | 0 | 0 | **1** |
| 42245320600100 | 1 | 0 | 0 | 0 | 0 | 0 | 0 | **1** |
| 42708303580000 | 1 | 0 | 0 | 0 | 0 | 0 | 0 | **1** |
| 42708403980000 | 0 | 0 | 0 | 0 | 0 | 0 | 0 | **0** |
| 42245328930000 | 0 | 0 | 0 | 0 | 0 | 0 | 0 | **0** |
| 42245328760000 | 0 | 0 | 0 | 0 | 0 | 0 | 0 | **0** |
| **TOTAL WELLS** | **87** | **28** | **7** | **22** | **13** | **10** | **62** | **229** |

**APPENDIX B**

Static $CO_2$ storage resources estimated using the "pessimistic NTG" model, variable by $CO_2$ density at reservoir conditions and storage efficiency $E_{saline}$ and illustrated in Figure 4.2.

| | | **$CO_2$ Density (kg/m$^3$)** | | | | | | |
|---|---|---|---|---|---|---|---|---|
| ***$E_{saline}$*** | | **620** | **630** | **640** | **650** | **660** | **670** | **750** |
| | **1%** | 33 | 34 | 34 | 35 | 35 | 36 | 40 |
| | **5%** | 165 | 168 | 170 | 173 | 176 | 179 | 200 |
| | **10%** | 330 | 336 | 341 | 346 | 352 | 357 | 400 |
| | **14%** | 462 | 470 | 477 | 485 | 492 | 500 | 560 |
| | **20%** | 661 | 671 | 682 | 693 | 703 | 714 | 799 |
| | **50%** | 1651 | 1678 | 1705 | 1732 | 1759 | 1785 | 1998 |

## APPENDIX C

$CO_2$ storage resources, normalized to thickness and area (Mt-km$^2$-m), and relevant parameters from different studies in the vicinity. Illustrated in Figure 4.8. Some parameters (e.g., net thickness) were not explicitly mentioned in some studies and had to be estimated indirectly.

| Researcher | Scale/Method | E | Area (km$^2$) | NET thickness (m) | Capacity (Mt) | Norm. capacity (Mt/km$^2$/m) | Prob | CO2 density (kg/m$^3$) |
|---|---|---|---|---|---|---|---|---|
| **Ruiz (2019)** | Field scale Static - HC sand | 14% | 13 | 60 | 11 | 0.0141 | P50 | 650 |
| | Field scale Static - SIOI | 14% | 13 | 320 | 108 | 0.0260 | P50 | 650 |
| **Ramirez Garcia (2019)** | Static | 14% | 12.5 | 77 | 24 | 0.0249 | P50 | 626-660 |
| | | 7% | | | 12 | 0.0125 | P90 | |
| | | 24% | | | 41.22 | 0.0428 | P10 | |
| | $CO_2$-SCREEN | 9.6% | | | 16.36 | 0.0170 | P90 | |
| | | 22% | | | 38.61 | 0.0401 | P50 | |
| | | 41% | | | 71.78 | 0.0746 | P10 | |
| **Wallace (2013)** | Regional static | 4.5% | 19.2 | 1981 | 7.7 (Mt/km$^2$) | 0.0037 | - | 650-700 |
| **Bump & Hovorka (2024)** | Regional pressure-limited and depth-variable | 0.75% | - | ~800 | 1.8 (Mt/km$^2$) | 0.00225 | - | - |
| **Afifi (2026) (this study)** | Local static | 1% | 62 | 234 | 37.7 | 0.00188 | P90 | 620 |
| | | 14% | | | 528.2 | 0.0263 | P50 | |
| | | 50% | | | 1886.3 | 0.0938 | P10 | |
| | | 1% | | 214 | 46.1.6 | 0.00207 | P90 | 750 |
| | | 14% | | | 583.22 | 0.0290 | P50 | |
| | | 50% | | | 2082.3 | 0.1035 | P10 | |

## References


Alberty, M., 1992. Standard Interpretation: Part 4. Wireline Methods.

Bachu, S., 2015. Review of $CO_2$ storage efficiency in deep saline aquifers. International Journal of Greenhouse Gas Control, 40, 188–202.

Beckham, E. C., 2018. $CO_2$ Storage in Deltaic Environments of Deposition: Integration of 3-Dimensional Modeling, Outcrop Analysis, and Subsurface Application. Master's thesis.

Blondes, M. S., Knierim, K. J., Croke, M. R., Freeman, P. A., Doolan, C., Herzberg, A. S., & Shelton, J. L., 2023. US Geological Survey National Produced Waters Geochemical Database v 3.0, December 2023. US Geological Survey.

Bump, A.P., Bakhshian, S., Ni, H., Hovorka, S.D., Olariu, M.I., Dunlap, D., Hosseini, S.A. and Meckel, T.A., 2023. Composite confining systems: Rethinking geologic seals for permanent $CO_2$ sequestration. International Journal of Greenhouse Gas Control, 126, p.103908.

Bump, A.P., Hovorka, S.D. and Meckel, T.A., 2021. Common risk segment mapping: Streamlining exploration for carbon storage sites, with application to coastal Texas and Louisiana. International Journal of Greenhouse Gas Control, 111, p.103457.

Bump, A.P. and Hovorka, S.D., 2023a. Fetch-trap Pairs: Exploring definition of carbon storage prospects to increase capacity and flexibility in areas with competing uses. International Journal of Greenhouse Gas Control, 122, p.103817.

Bump, A.P. and Hovorka, S.D., 2023b. Minimizing exposure to legacy wells and avoiding conflict between storage projects: Exploring area of review as a screening tool. International Journal of Greenhouse Gas Control, 129, p.103967.

Bump, A.P. and Hovorka, S.D., 2024. Pressure space: The key subsurface commodity for CCS. International Journal of Greenhouse Gas Control, 136, p.104174.

Carr, D. L., Treviño, R., Meckel, T. A., Breton, C., Yang, C., and Miller, E., 2011, Executive summary: Task 15 – NATCARB atlas update – CO2 sequestration capacity, offshore western Gulf of Mexico: The University of Texas at Austin, Bureau of Economic Geology, 2 p.

Carr, D. L., Wallace, K. J., Yang, C., and Nicholson, A. J., 2016, CO2 sequestration capacity sectors in Miocene strata of the Offshore Texas State Waters: Gulf Coast Association of Geological Societies Journal, v. 5, p. 130–140. Available online here: http://www.gcags.org/exploreanddiscover/2016/00103_carr_et_al.pdf

Carr, D. L., Wallace, K. J., Nicholson, A. J., and Yang, C., 2017, Chapter 5: Regional CO2 static capacity estimate, offshore Miocene saline aquifers, Texas state waters, in Treviño, R. H. and Meckel, T. A., eds., Geological CO2 sequestration atlas of Miocene strata, offshore Texas state waters: Austin, Texas, Bureau of Economic Geology, Report of Investigations, no. 283, p. 37–46. http://doi.org/10.23867/RI0283D.

DeAngelo, M.V., Fifariz, R., Meckel, T. and Treviño, R.H., 2019. A seismic-based CO2-sequestration regional assessment of the Miocene section, northern Gulf of Mexico, Texas and Louisiana. International Journal of Greenhouse Gas Control, 81, pp.29-37.

Denham, R. L., ed. 1962. *Typical Oil & Gas Fields of Southeast Texas*. Houston, TX: Houston Geological Society.

Dhakal, S., Minx, J.C., Toth, F.L., Reisinger, ..., Lamb, W.F., Döbbeling, N., Wiedmann, T., Hubacek, K., Andrew, R.M., Crippa, M., Forster, P.M., Olivier, J., Peters, G.P., Pongratz, J., Rigby, M., Saunois, M., Smith, S.J., Solazzo, E., Tian, H., Blok, K., Clark, H., Cowie, A., Fuglestvedt, J.S., Geden, O., Ginzburg, V., Guivarch, C., House, J.I., Mrabet, R., Nabuurs, G.J., Riahi, K., Strømman, A.H., Schaeffer, R., van Vuuren, D.P., Al Khourdajie, A., & Slade, R., 2022: Emissions Trends and Drivers Supplementary Material. In IPCC, 2022: Climate Change 2022: Mitigation of Climate Change. Contribution of Working Group III to the Sixth Assessment Report of the Intergovernmental Panel on Climate Change [P.R. Shukla, J. Skea, R. Slade, A. Al Khourdajie, R. van Diemen, D. McCollum, M. Pathak, S. Some, P. Vyas, R. Fradera, M. Belkacemi, A. Hasija, G. Lisboa, S. Luz, J. Malley, (eds.)]. Available from https://www.ipcc.ch/report/ar6/wg3/.

Ellett, K., Zhang, Q., Medina, C., Rupp, J., Wang, G. and Carr, T., 2013. Uncertainty in regional-scale evaluation of CO2 geologic storage resources—Comparison of the Illinois Basin (USA) and the Ordos Basin (China). Energy Procedia, 37, pp.5151-5159.

Ewing, T.E. and Galloway, W.E., 2019. Evolution of the northern Gulf of Mexico sedimentary basin. The sedimentary basins of the United States and Canada, pp. 627-694

Galloway, W.E., 1989. Genetic stratigraphic sequences in basin analysis II: application to northwest Gulf of Mexico Cenozoic basin. AAPG bulletin, 73(2), pp.143-154.

Galloway, W.E., Ganey-Curry, P.E., Li, X. and Buffler, R.T., 2000. Cenozoic depositional history of the Gulf of Mexico basin. AAPG bulletin, 84(11), pp.1743-1774.

Galloway, W.E., 2008. Depositional evolution of the Gulf of Mexico sedimentary basin. Sedimentary basins of the world, 5, pp.505-549.

Galloway, W.E., Whiteaker, T.L. and Ganey-Curry, P., 2011. History of Cenozoic North American drainage basin evolution, sediment yield, and accumulation in the Gulf of Mexico basin. Geosphere, 7(4), pp.938-973.

Goddard, D. A., and Zimmerman, R. K.,2003. Shallow Miocene and Oligocene gas potential: southeastern Louisiana's Florida Parishes.

Goodman, A., Hakala, A., Bromhal, G., Deel, D., Rodosta, T., Frailey, S., Small, M., Allen, D., Romanov, V., Fazio, J. and Huerta, N., 2011. US DOE methodology for the development of geologic storage potential for carbon dioxide at the national and regional scale. International Journal of Greenhouse Gas Control, 5(4), pp.952-965.

Goodman, A. L., Bromhal, G., Strazisar, B., Rodosta, T., Guthrie, W., & Guthrie, G., 2013. Comparison of methods for geologic storage of carbon dioxide in saline formations. International Journal of Greenhouse Gas Control, 18, 329-342. https://doi.org/10.1016/j.ijggc.2013.07.016

Goodman, A., Sanguinito, S., and Levine, J. S., 2016. Prospective CO2 saline resource estimation methodology: Refinement of existing US-DOE-NETL methods based on data availability. International Journal of Greenhouse Gas Control, 54, 242-249.

Hosseini, S.A., Ganjdanesh, R. and Kim, S., 2018. Enhanced Analytical Simulation Tool (EASiTool) for $CO_2$ Storage Capacity Estimation and Uncertainty Quantification, Bureau of Economic Geology, Jackson School of Geosciences, The University of Texas at Austin, Austin, Texas.

Intergovernmental Panel on Climate Change (IPCC) 2023, Climate Change 2023: Synthesis Report. Contribution of Working Groups I, II and III to the Sixth Assessment Report of the Intergovernmental Panel on Climate Change, Core Writing Team, H. Lee and J. Romero (eds.), IPCC, Geneva, Switzerland, doi:10.59327/IPCC/AR6-9789291691647.

International Energy Agency (IEA) Global Energy Review 2025, IEA, Paris https://www.iea.org/reports/global-energy-review-2025, Licence: CC BY 4.0

Kamel, M. H., & Mabrouk, W. M., 2003. Estimation of shale volume using a combination of the three porosity logs. Journal of Petroleum Science and Engineering, 40(3-4), 145-157.

Leng, J., Bump, A., Hosseini, S.A., Meckel, T.A., Wang, Z. and Wang, H., 2024. A comprehensive review of efficient capacity estimation for large-scale CO2 geological storage. Gas Science and Engineering, 126, p.205339.

Loucks, R. G., & Dutton, S. P. (2023). Northern Gulf of Mexico sandstone reservoir-quality database (GOMRQ): Multiple data types for evaluating reservoir-quality risk (Report of Investigations No. 289). Bureau of Economic Geology. https://doi.org/10.23867/RI0289D

Meckel, T.A., Treviño, R., Carr, D., Nicholson, A. and Wallace, K., 2013. Offshore CCS in the northern Gulf of Mexico and the significance of regional structural compartmentalization. Energy Procedia, 37, pp.4526-4532.

Meckel, T.A., Treviño, R. and Hovorka, S.D., 2017. Offshore CO2 storage resource assessment of the northern Gulf of Mexico. Energy Procedia, 114, pp.4728-4734.

Meckel, T.A., Treviño, R., and Hovorka, S.D., 2017. Offshore CO2 Storage Resource Assessment of the Northern Gulf of Mexico, Energy Procedia, 114, pp. 4728-4734, ISSN 1876-6102, https://doi.org/10.1016/j.egypro.2017.03.1609.

Meckel, T. A., and Rhatigan, J.-L. T., 2017, Chapter 2: Implications of Miocene petroleum systems for geologic CO2 sequestration beneath Texas offshore lands, in Treviño, R. H., and Meckel, T. A., eds., Geological CO2 sequestration atlas for Miocene strata offshore Texas state waters: The University of Texas at Austin, Bureau of Economic Geology Report of Investigations No. 283, p. 7–13, http://doi.org/10.23867/RI0283D.

Nicholson, A. J., 2012, Empirical analysis of fault seal capacity for CO2 sequestration, Lower Miocene, Texas Gulf Coast, Master's Thesis, University of Texas at Austin, http://repositories.lib.utexas.edu/handle/2152/ETD-UT-2012-05-5606

Ni, H., Bump, A.P. and Bakhshian, S., 2024. An experimental investigation on the CO2 storage capacity of the composite confining system. International Journal of Greenhouse Gas Control, 134, p.104125.

Ni, H., Bakhshian, S., Bump, A. and Hovorka, S. (unpublished) CCS Workbook: Manual for Applied CCS Practitioners. 1st edn. Austin, USA: Gulf Coast Carbon Center, Bureau of Economic Geology, The University of Texas at Austin.

Olariu, M.I, DeAngelo, M., Dunlap, D. and Treviño, R., 2019. High frequency (4th order) sequence stratigraphy of Early Miocene deltaic shorelines, offshore Texas and Louisiana.

Oumarou, S., Mabrouk, D., Tabod, T.C., Marcel, J., Ngos III, S., Essi, J.M.A. and Kamguia, J., 2021. Seismic attributes in reservoir characterization: an overview. Arabian Journal of Geosciences, 14(5), p.402.

Paola, C., Mullin, J., Ellis, C., Mohrig, D., Swenson, J., Parker, G., Hickson, T., Heller, P., Pratson, L., Syvitski, J., Sheets, B., Strong, N., 2001. Experimental Stratigraphy, GSA Today 11 (7), 4.

Ruiz, I., 2019. Characterization of the High Island 24L Field for Modeling and Estimating CO2 Storage Capacity in the Offshore Texas State Waters, Gulf of Mexico. Master's Thesis.

Ramirez Garcia, O., 2019. Geological Characterization and Modeling for Quantifying CO2 Storage Capacity for the High Island 10-L Field in Texas State Waters, Offshore Gulf of Mexico. Master's Thesis.

Sabbagh, R.J., 2017. Pre-injection Reservoir Characterization for CO2 Storage in the Inner Continental Shelf of the Texas Gulf of Mexico. Master's Thesis (and Petrel Project).

Seni, S. J., Hentz, T.F., & Kaiser, W.R., 1997. Atlas of northern Gulf of Mexico gas and oil reservoirs. Vol. 1: Miocene and Older Reservoirs: The University of Texas at Austin, Bureau of Economic Geology, 199.

Snedden, J.W. and Galloway, W.E., 2019. The Gulf of Mexico Sedimentary Basin: Depositional Evolution and Petroleum Applications. Cambridge: Cambridge University Press. 1 - 346.

Society of Petroleum Engineers, American Association of Petroleum Geologists, Society of Petroleum Evaluation Engineers, Society of Exploration Geophysicists, World Petroleum Council and European Association of Geoscientists and

Engineers, 2017, Storage resources management system guidelines. Houston, TX: Society of Petroleum Engineers.

SLB (2023) Petrel E&P software platform, Version 2023. Houston, TX: SLB.

Treviño, R.H. and Meckel, T.A. eds., 2017. Geological CO2 sequestration atlas of Miocene strata, offshore Texas state waters. Bureau of Economic Geology, The University of Texas at Austin, Report of Investigations No. 283, p. 74.

Treviño, R. H., and Rhatigan, J.-L. T., 2017, Chapter 1: Regional geology of the Gulf of Mexico and the Miocene section of the Texas near-offshore waters, in Treviño, R. H., and Meckel, T. A., eds., Geological CO2 sequestration atlas of Miocene strata, offshore Texas state waters: Austin, Texas, The University of Texas at Austin, Bureau of Economic Geology, Report of Investigations, no. 283, p. 3–6, http://doi.org/10.23867/RI0283D.

United States Environmental Protection Agency (EPA), 2026, Class VI wells used for geologic sequestration of carbon dioxide. Available at: EPA Class VI Wells Used for Geologic Sequestration of Carbon Dioxide

Van Wagoner, J.C., Mitchum, R.M., Campion, K.M., and Rahmanian, V.D., 1990. Siliciclastic Sequence Stratigraphy in Well Logs, Cores, and Outcrops. American Association of Petroleum Geologists. Methods in Exploration Series

Wang, Z.W, Qi, S., and Zheng, B., 2024. Uncertainty Analysis of the Storage Efficiency Factor for $CO_2$ Saline Resource Estimation. Energies, 17(6), 1297. https://doi.org/10.3390/en17061297

Wang, Z.W. and Hosseini, S., 2024. Advanced CO2 storage capacity estimation with EASiTool V. 5. In Carbon Capture, Utilization, and Storage Conference and Exhibition, 11–13 March 2024 (pp. 62-71). Carbon Capture, Utilization, and Storage (CCUS) Conference and Exhibition.

Wallace, K.J., Meckel, T.A., Carr, D.L., Treviño, R.H. and Yang, C., 2014. Regional CO2 sequestration capacity assessment for the coastal and offshore Texas Miocene interval. Greenhouse Gases: Science and Technology, 4(1), pp.53-65.

Wallace, K.J., 2013. Use of 3-dimensional dynamic modeling of $CO_2$ injection for comparison to regional static capacity assessments of Miocene sandstone reservoirs in the Texas State Waters, Gulf of Mexico. Master's Thesis.

Zulqarnain, M., Sears, S.O., Zeidouni, M., Hughes, R.G., Carlson, D. and Rivera, C.F., 2023. CCS site selection in saline Miocene formations in South Louisiana. International Journal of Greenhouse Gas Control, 122, p.103818.